Dynamically Programmable Surfaces for High-Speed Optical Modulation and Detection

by

Cheng Peng

B.A., Cornell University (2013)
S.M., Massachusetts Institute of Technology (2015)

Submitted to the Department of Electrical Engineering and Computer Science
in partial fulfillment of the requirements for the degree of

Doctor of Philosophy in Electrical Engineering and Computer Science

at the

MASSACHUSETTS INSTITUTE OF TECHNOLOGY

May 2020

Author .....
Department of Electrical Engineering and Computer Science
May 15, 2020

Certified by .....
Dirk R. Englund
Associate Professor of Electrical Engineering and Computer Science
Thesis Supervisor

Accepted by .....
Leslie A. Kolodziejski
Professor of Electrical Engineering and Computer Science
Chair, Department Committee on Graduate Students

Dynamically Programmable Surfaces for High-Speed Optical Modulation and Detection

by

Cheng Peng

Submitted to the Department of Electrical Engineering and Computer Science
on May 15, 2020, in partial fulfillment of the
requirements for the degree of
Doctor of Philosophy in Electrical Engineering and Computer Science

Abstract

Dynamically programmable surfaces for spatiotemporal control of light are crucial to many optoelectronic technologies including high-speed optical communication, display and projection, autonomous driving, optical information processing, imaging, and fast programmable optical tweezers. Currently available electro-optically tunable components are often bulky, inefficient, and have limited operation speeds. This thesis describes the development of a compact, high-speed, electro-optic spatial light modulator (SLM) architecture based on two-dimensional arrays of tunable microcavities. Optimized microcavity designs can enable high-speed, high diffraction efficiency SLMs with standard-CMOS-compatible driving voltages. An electro-optic material, graphene, is also investigated in detail. A graphene carrier density spatiotemporal modulation technique is proposed and experimentally validated. This technique enables the demonstration of a compact graphene thermopile in the mid-infrared wavelengths and paves the way for future implementations of graphene plasmonic metasurfaces.

Thesis Supervisor: Dirk R. Englund
Title: Associate Professor of Electrical Engineering and Computer Science

Acknowledgments

First, I would like to express my sincere gratitude to my advisor, Prof. Dirk Englund, for his immense knowledge and continuous inspiration, motivation, and support. I would like to especially thank him for the vision he brought to my research. He broadened my horizon and turned me from a naive first-year student who knew only about deriving equations for class to a researcher with the ability to identify important problems and push the boundaries of technology. I am also grateful that Dirk gave me the freedom to switch direction in the middle of my PhD. This ultimately allowed me to discover the topic I was most passionate about. I would also like to thank the members of my thesis and RQE committees - Prof. Tomas Palacios, Prof. Kevin O'Brien, and Prof. Jing Kong - whose thoughtful advice made this thesis better. Finally, I would like to thank my academic advisor, Prof. Karl Berggren, who helped me stay on track in the program and gave me excellent advice every semester.

My sincere thanks also go to Jim Daley and Mark Mondol of the NSL nanofabrication facility, whose knowledge, experience, and down-to-earth attitudes significantly lowered the barrier to fabrication, and Janice Balzer, who helped me with every administrative issue with speed and patience.

I would also like to thank my mentors and collaborators. Especially, I'd like to thank Dr. Ren-Jye Shiue, who taught me everything about graphene and optoelectronic experiments, Prof. Dmitri Efetov, who guided me bit by bit through my first major project, and Dr. Ryan Hamerly, for his insightful theoretical guidance. I learned a great deal from their broad knowledge and their way of performing research. Thank you also to Christopher Panuski who worked as the best team mate one could ask for. His enthusiasm and self-discipline never ceased to amaze me and I found myself learning from him in every aspect. I am grateful for this opportunity to work with him and support each other through a valuable friendship.

My next block of thanks goes to my friends both in and out of the lab - every exceptional member of the Quantum Photonics Group, Mihika Prabhu and Christopher Panuski whom I spent days and nights in the office with, college friends in the

sleepless Wechat room (especially Yiran Li), friends from high school who met with me for tennis every week, and other people I met at MIT whom I shared the journey with.

I would also like to especially thank Bolei Zhou for being the best partner I have had and for constantly supporting and inspiring me to pursue my goal. Thank you for being my light.

Finally I would like to dedicate this thesis to my parents who gave me their constant and unconditional support, encouragement, and love. Thank you for believing in me and providing me with all the resources over the years. I can not imagine having a better family.

Contents

List of Figures

List of Tables

Chapter 1

Introduction

1.1 Spatiotemporal light control

Spatial light modulators (SLMs), which manipulate the spatial amplitude and phase distributions of light waves, find use in a wide range of applications (Fig. 1-1), including compact beam steering for LiDAR [11, 12], display and projection [13], beam shaping [14], biomedical *in-vivo* imaging through scattering media [15], wavefront encoding for optical information processing [16, 5], high-speed interconnects [17], and fast programmable optical tweezers [18, 2].

After decades of advances, SLMs based on liquid crystals and digital micromirrors can now reach large pixel counts exceeding 10^6 with pixel pitches of less than 10 µm and driving voltages compatible with CMOS (complementary metal–oxide–semiconductor) processes [19, 4]. However, the rather slow frame rates in such SLMs (in the range of kHz) presents limitations for many applications. For example, optics show promise to replace electronics in data interconnects thanks to their low loss and low power consumption, but until now no electro-optic modulators have simultaneously achieved a large channel count and a large channel bandwidth to clearly demonstrate optical interconnects' advantage. Another example is mirror-based color projectors implemented with duty-cycle modulation and color wheels. Currently, a transition from bright to dark pixels in projectors with a kHz frame rate would produce an undesirable rainbow effect that causes discomfort for some people.

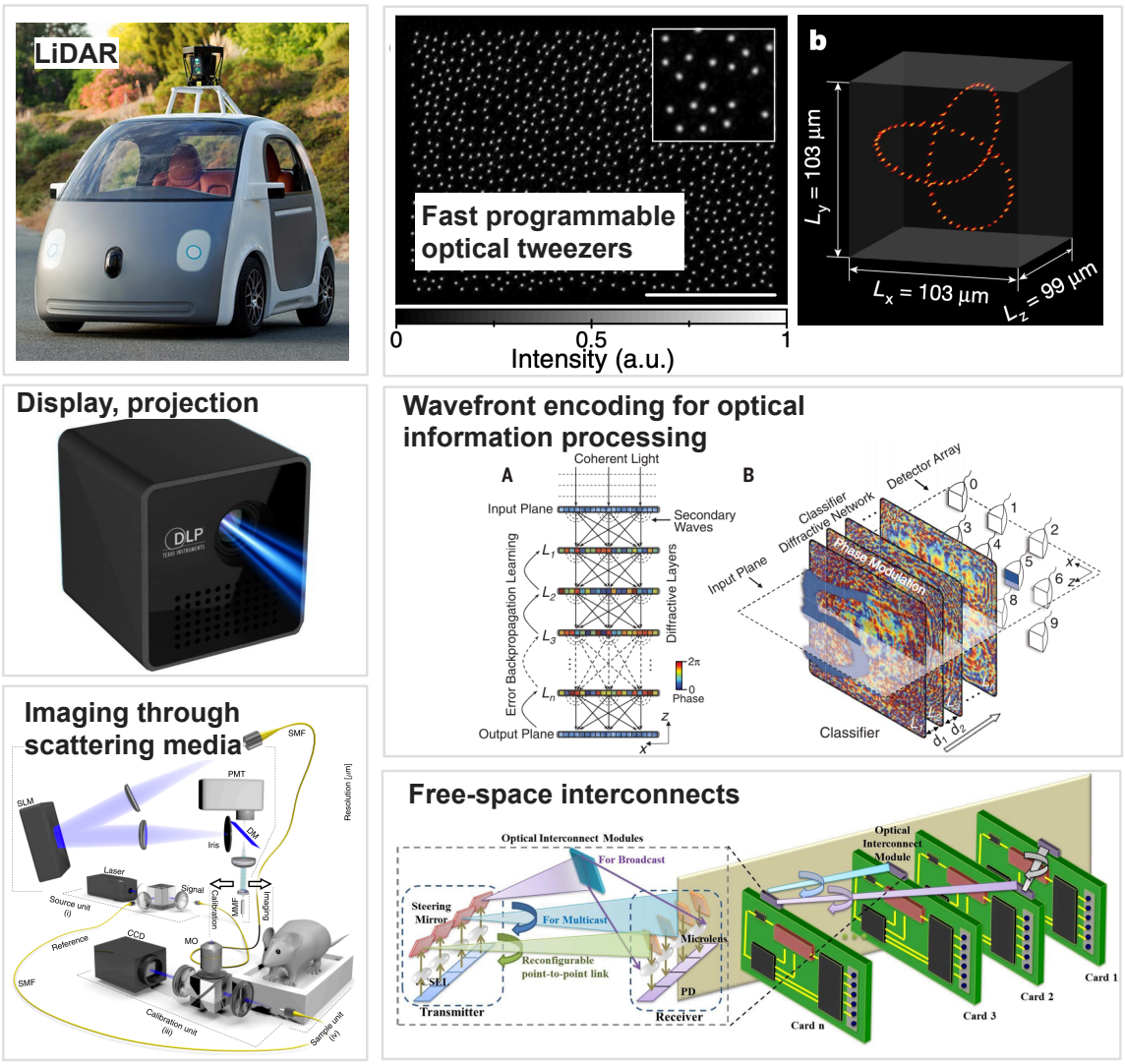

Figure 1-1: Spatial light modulators find a wide range of applications, including compact beam steering for LiDAR, fast programmable optical tweezers, display and projection, wavefront encoding for optical information processing, biomedical *in-vivo* imaging through scattering media, and high-speed interconnects. Figure reproduced from [1, 2, 3, 4, 5, 6, 7].

1.2 Commercial spatial light modulators

Current commercial technologies for SLMs are based on two dominant platforms, liquid crystals (LCs) and digital micromirror devices (DMDs). Table 1.1 summarizes several key figure-of-merits of these two platforms.

Table 1.1: **Figure-of-merits of commercial SLMs.**

	Nematic LCs / LCOS [19]	Ferroelectric LCs [20]	Commercial DMDs [21]	High-Voltage MEMS [22]
Modulation Mode	Phase and amplitude	Amplitude only (binary)	Amplitude only (binary)	Phase and amplitude
Frame Rate	100 Hz	10 kHz	40 kHz	10 kHz
Driving Voltage	< 5 V	0.005 V	3.3 V	50 V
Pixel Pitch	< 20 µm	13.2 µm	5.4 µm	40 µm
Insertion Loss	< 0.5 dB	2.2 dB	0.5 dB	0.2 dB
Array Size	$< 1920 \times 1080$	1280×768	1920×1080	128×128
Fill Factor	$< 95\%$	90%	∼100%	84%

Notably, both platforms allow large pixel counts $> 10^6$, small pixel pitches $<$ 10 µm, and low driving voltages compatible with CMOS processes, but the slow response times associated with these two mechanical tuning mechanisms limit the frame rate to kHz [23, 20, 19, 13, 21, 22]. In addition, the complex design and manufacturing process for DMDs and their relatively high failure rate [24] due to moving parts make them not ideal for many applications. To realize high-speed (MHz or GHz) spatial light modulators, a new material platform and its associated architecture are needed.

1.3 Emerging electro-optic modulation platforms

Several emerging SLM platforms are currently under research. Thermo-optic effect in silicon photonics [25] and micro-electromechanical systems (MEMS) [26] are promising for independent optical amplitude and phase control, but since the underlying thermo-optic effect and mechanical effect have response time in the µs range, the refresh rate is still limited to 100 kHz.

Other electro-optic effects have promised faster speeds, including quantum-confined Stark effect in quantum wells [27], free carrier dispersion effects in semiconductors

or epsilon-near-zero materials (such as indium tin oxide ITO) [28, 29], electro-optic effect in 2D materials [30], and the linear electro-optic (Pockels) effect [31, 32]. In these platforms, since the electro-optic effects are associated with band-bending, charge carrier dynamics, or atomic displacement, the faster timescale allows modulation in excess of GHz.

However, these modulation mechanisms are weaker compared to those of LCs and DMDs, due to either the small voltage-induced change in the refractive index ($\Delta n < 0.01$) or the small volume where the change can happen (atomic layer in 2D materials or surface layer in ITO). Therefore, a new SLM architecture where these weak effects can be enhanced is needed to ensure CMOS-compatible driving voltages.

This thesis describes the development of a compact, high-speed, electro-optic SLM architecture based on two-dimensional arrays of tunable microcavities. Chapter 2 discusses the general theoretical methodology that can be used for the design and optimization of the tunable microcavity pixels along with an outlook for the fabrication and CMOS integration process of this architecture. Chapter 3 investigates the electro-optic material platform graphene and describes an experimental technique for surface electrical gating of graphene at the nanoscale. Chapter 4 describes a few photonic device concepts based on electrically-modulated graphene. The thesis ends with an outlook on the future realization of a high-speed electro-optic spatial light modulator.

Chapter 2

High-Speed Spatial Light Modulators with Tunable Cavity Arrays

This chapter discusses the proposal of a high-speed spatial light modulator architecture based on two-dimensional arrays of microcavities, whose resonant wavelengths can be tuned with externally applied voltages via high-speed electro-optic effect. The chapter starts with an introduction of this architecture, followed by a detailed illustration of the design methodology for each microcavity pixel and a numerical demonstration of a phase-only SLM with a standard-CMOS-compatible operation voltage and a high diffraction efficiency. The same design methodology is also used for the design of an amplitude modulator. The chapter ends with an overview of the fabrication process for such designs and a discussion of its potential integration with complementary metal–oxide–semiconductor (CMOS) back-end-of-line (BEOL) process.

2.1 Tunable microcavity array SLMs

To take advantage of the high-speed electro-optic effects that are typically much weaker than LC and DMD's modulation effects, I propose an SLM architecture that consists of a two-dimensional array of microcavities whose resonant frequency is modulated through an active electro-optic material embedded in the cavity. One example geometry of such microcavities is illustrated in the inset of Fig. 2-1.

To illustrate the device concept, Pockels effect, also known as the linear electro-optic effect, is used here as an example. An applied electric field shifts the refractive index of the active material according to

$$\Delta\left(\frac{1}{n^2}\right)_i = \sum_{j=1}^{3} r_{ij} E_j \tag{2.1}$$

where r_{ij} is the electro-optic tensor. The Pockels effect has two key properties. First, only the real part of the refractive index is modified, leading to high $\Delta n/\Delta k$ ratio and phase-only modulation. Second, most common Pockels materials, including ferroelectric oxides, have ultrafast response times in the femtosecond range.

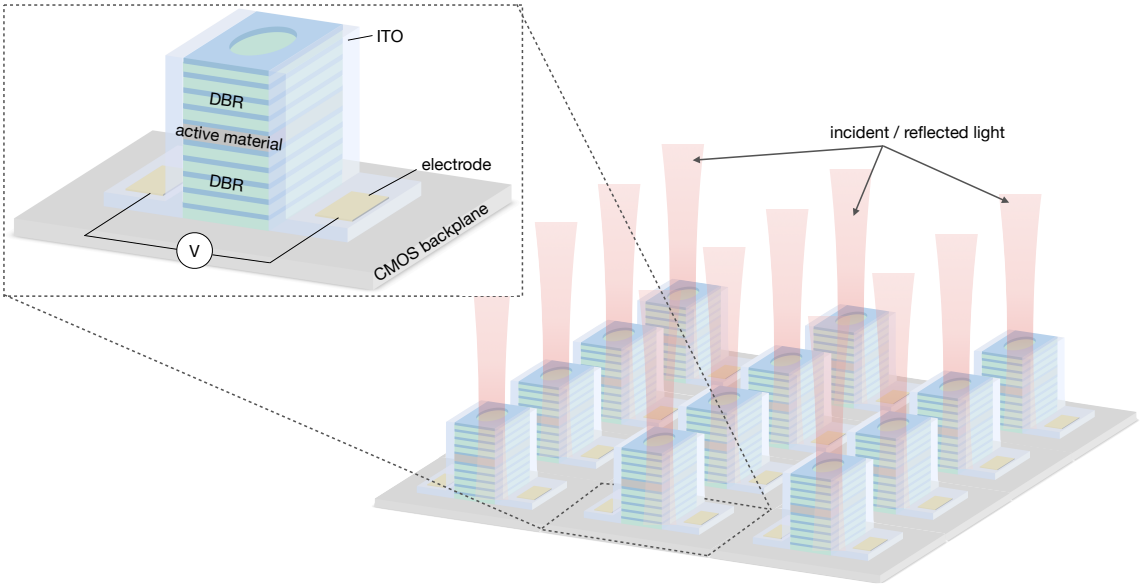

Figure 2-1: Spatial light modulators with two-dimensional tunable microcavity arrays. Each phase shifter pixel consists of a one-sided vertical microcavity capable of modulating the phase of the reflected light. An array of phase shifter elements can modulate the spatial profile of the reflected wavefront and generate a desirable far-field radiation pattern. DBR: distributed Bragg reflector. ITO: indium tin oxide. CMOS: complementary metal–oxide–semiconductor.

Similar to other high-speed electro-optic effects, the downside of Pockels effect is that it is relatively weak ($\Delta n \sim 0.01$), so it is difficult to achieve a phase change of π under voltages that for practicality of driving electronics should be below $\sim$ 10 V. For example, for a high electric field of 10 V/µm, reflection through a 1 µm

layer of barium titanate (Pockels coefficient $r_{42} = 923\,\mathrm{pm/V}$ [32]) would yield a phase modulation change of only $\Delta\phi = \frac{2\pi}{\lambda}\Delta n(2h) \sim 0.15\pi$ at $\lambda = 1550\,\mathrm{nm}$. Hence to address this problem, I propose the design of a one-sided microcavity to amplify the modulated phase.

The spatial light modulator is then composed of a two-dimensional array of such vertical microcavities, as illustrated in Fig. 2-1. Each microcavity pixel is a free-space phase-only modulator that works in the reflection mode, allowing incident light to be reflected with a phase delay controlled by an electrical voltage applied through the metal interconnect contacts in the CMOS backplane underneath. The 2D array of phase shifter pixels, when controlled independently and simultaneously, can impose a spatially variant phase distribution on the wavefront of the reflected light, generating a far-field radiation pattern according to

$$U(x,y,z) = \int_{-\infty}^{\infty}\int_{-\infty}^{\infty} A(f_x,f_y,0)e^{j2\pi\sqrt{\frac{1}{\lambda^2}-f_x^2-f_y^2}}e^{j2\pi(f_x x+f_y y)}df_x df_y \tag{2.2}$$

where $U(x,y,z)$ is the far-field radiation field of the reflected light from the SLM, $A(f_x,f_y,0)$ is the Fourier transform of the near-field of the reflected light as a function of the spatial frequencies f_x and f_y and λ is the wavelength of light. Using phase retrieval algorithms such as the Gerchberg-Saxton algorithm [33], the required phase from each pixel can be calculated and set by the corresponding control voltage, allowing an arbitrary desired far-field pattern to be generated.

2.2 Linear electro-optic (Pockels) effect

The electro-optic effect is the change in material's refractive index induced by the presence of a static or low-frequency (up to microwave frequencies) electric field. When the change in refractive index depends linearly on the strength of the electric field, the effect is called the linear electro-optic effect or Pockels effect. It can be

described in terms of a nonlinear polarization by [34]

$$P_i(\omega) = 2\epsilon_0 \sum_{j,k=1}^{3} \chi_{ijk}^{(2)}(\omega = \omega + 0) E_j(\omega) E_k(0) \tag{2.3}$$

where $\chi_{ijk}^{(2)}$ is the material's second-order nonlinear susceptibility, $E_j(\omega)$ is the electric field of the light, $E_k(0)$ is the applied low-frequency electric field and ϵ_0 is the free-space electric permittivity.

This section starts with a brief review of the mathematical formalism for modeling Pockels effect [34], followed by a discussion of two material choices with high Pockels coefficients, along with the method to determine the material's optimal crystalline orientation in an electro-optic device.

For an anisotropic crystal that is lossless and non-optically active, the surfaces of constant energy density in the space of the field vector $\vec{D}$ are ellipsoids and the shape of these ellipsoids can be described with the spatial coordinates (x, y, z) themselves. This shape is known as the *optical indicatrix* and is described by the following equation

$$\left(\frac{1}{n^2}\right)_{11} x^2 + \left(\frac{1}{n^2}\right)_{22} y^2 + \left(\frac{1}{n^2}\right)_{33} z^2 + 2\left(\frac{1}{n^2}\right)_{23} yz + 2\left(\frac{1}{n^2}\right)_{13} xz + 2\left(\frac{1}{n^2}\right)_{12} xy = 1 \tag{2.4}$$

where n is the refractive index of this anisotropic crystal and is related to the material's dielectric permittivity tensor by

$$\left(\frac{1}{n^2}\right)_{ij} = (\epsilon^{-1})_{ij} = (\epsilon^{-1})_{ji} \tag{2.5}$$

With the indicatrix, the refractive index can be determined by intersecting a plane perpendicular to the propagation direction and calculating the semi-major and semi-minor axes of the resultant ellipse, with the polarization of the corresponding field vector $\vec{D}$ given by the orientations of these axes.

In the crystal's principal-axis coordinate system, the indicatrix takes its simplest

form

$$\left(\frac{1}{n^2}\right)_{11} x^2 + \left(\frac{1}{n^2}\right)_{22} y^2 + \left(\frac{1}{n^2}\right)_{33} z^2 = 1 \tag{2.6}$$

When a low-frequency electric field is applied to this crystal, the $(\frac{1}{n^2})_{ij}$'s can be expressed as a power series in the strength of the components E_k of the applied electric field as

$$\left(\frac{1}{n^2}\right)_{ij} = \left(\frac{1}{n^2}\right)^{(0)}_{ij} + \sum_{j=1}^{3} r_{ijk} E_k + \sum_{j,k=1}^{3} s_{ijkl} E_k E_l + \cdots \tag{2.7}$$

where r_{ijk} and s_{ijkl} describe the linear and quadratic electro-optic effects, respectively. Due to the symmetry of the dielectric permittivity tensor ϵ_{ij} and consequently the symmetry of the linear electro-optic tensor r_{ijk}, there are six independent dielectric permittivity elements and a contracted notation can be adopted to represent the third-rank tensor r_{ijk} as a two-dimensional (6×3) matrix according to the prescription

$$h = \begin{cases} 1 \text{ for } ij = 11 \\ 2 \text{ for } ij = 22 \\ 3 \text{ for } ij = 33 \\ 4 \text{ for } ij = 23 \text{ or } 32 \\ 5 \text{ for } ij = 13 \text{ or } 31 \\ 6 \text{ for } ij = 12 \text{ or } 21. \end{cases} \tag{2.8}$$

The linear electro-optic effect can then be written as

$$\Delta\left(\frac{1}{n^2}\right)_i = \sum_{j=1}^{3} r_{ij} E_j \tag{2.9}$$

where r_{ij} are known as the electro-optic (Pockels) coefficients, E_j represents the components of the applied electric field and the $\Delta(\frac{1}{n^2})_i$ represents the change of refractive index in one of the six independent indices.

2.2.1 Pockels effect in thin film $BaTiO_3$ and $LiNbO_3$

Two materials with high Pockels coefficients, thin film crystalline barium titanate ($BaTiO_3$) and lithium niobate ($LiNbO_3$), are promising candidates as the active material of the tunable microcavities.

Barium titanate (also known as BTO), with a bulk Pockels coefficient r_{42} of 1640 pm/V [34], has emerged as an excellent material for integrated electro-optic modulators owing to a recently developed epitaxial thin film synthesis process that maintains its tetragonal lattice structure in the thin film and shows a high thin-film Pockels coefficient, characterized to be as large as $r_{42} = 923$ pm/V [32]. Pockels modulation in BTO has sub-ps response time. A Si-integrated BTO electro-optic modulator has been demonstrated for high speed operation up to 65 GHz [32]. The epitaxial growth process is possible on standard silicon wafers and the material is chemically and thermally stable [35]. Direct wafer bonding process [36] using Al_2O_3 adhesion layers with a temperature budget well within the limits of the BEOL process (< 300 °C) has also expanded the possibility of thin film BTO integration to silicon-on-insulator wafers and CMOS backplanes [32, 37].

BTO's tetragonal lattice has the point group symmetry *4mm*. Hence the Pockels tensor is of the form

$$r_{ij} = \begin{bmatrix} 0 & 0 & r_{13} \\ 0 & 0 & r_{13} \\ 0 & 0 & r_{33} \\ 0 & r_{42} & 0 \\ r_{42} & 0 & 0 \\ 0 & 0 & 0 \end{bmatrix}. \tag{2.10}$$

For an electro-optic device to operate at a lower voltage, it is necessary to take advantage of the maximum element in the tensor $r_{42} = 923$ pm/V and realize the largest possible refractive index change.

Below, the optimal crystalline orientation with respect to the applied electric field direction for maximum Pockels effect is determined.

Figure 2-2 illustrates the coordinate system of the crystalline orientation, XYZ

(with BTO's <100> along Z-direction), and the coordinate system of the applied electric field, $X'Y'Z'$. In epitaxially grown BTO thin film with a thickness of several hundreds of nanometers, the <100> axis is oriented in-plane [35]. Hence X-direction is out-of-plane. X'-direction is chosen to be aligned with the X-direction. The horizontal rotational angle between the two coordinate systems is denoted by θ.

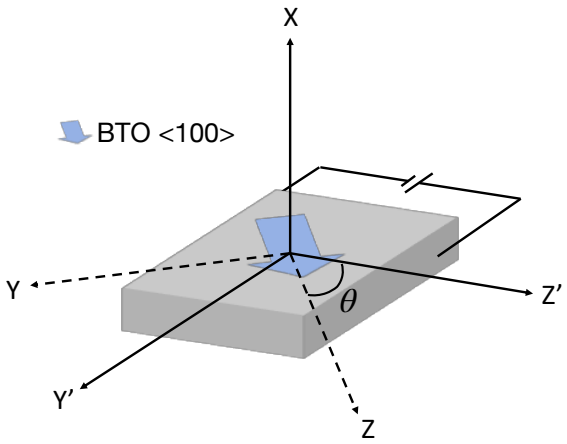

Figure 2-2: Illustration of the thin film BTO layer, its crystalline orientation, the direction of the applied E field, and the two coordinate systems.

The indicatrix in the crystal's principal-axis coordinate system can be written as

$$\left(\frac{1}{n_o^2}+r_{13}E_z\right)x^2+\left(\frac{1}{n_o^2}+r_{13}E_z\right)y^2+\left(\frac{1}{n_e^2}+r_{33}E_z\right)z^2+(r_{42}E_y)2yz+(r_{42}E_x)2zx=1 \tag{2.11}$$

where n_o and n_e are the ordinary and extraordinary refractive indices of the crystal, respectively, r_{13}, r_{33}, and r_{42} are the non-zero electro-optic coefficients for $4mm$ symmetry.

For vertically-oriented microcavities, the propagation direction is along X. Intersecting the perpendicular plane $x=0$ with the indicatrix, one can see that E_x does not contribute to the refractive index change for in-plane polarizations. Hence $\vec{E}$ is in-plane and Z'-direction can be chosen to align with $\vec{E}$'s direction.

Setting $E_x=0$ and transforming the indicatrix equation from the XYZ- into the $X'Y'Z'$-coordinate system by substituting x, y, and z by $x=x'$, $y=\cos\theta y'+\sin\theta z'$,

and $z = -\sin\theta y' + \cos\theta z'$, after some algebra, the equation becomes

$$\begin{aligned}
&\left(\frac{1}{n_o^2} + r_{13}E_z\right)(x')^2 \\
&+\left[\left(\frac{1}{n_o^2} + r_{13}E_z\right)\cos^2\theta + \left(\frac{1}{n_e^2} + r_{33}E_z\right)\sin^2\theta - r_{42}E_y \cdot 2\sin\theta\cos\theta\right](y')^2 \\
&+\left[\left(\frac{1}{n_o^2} + r_{13}E_z\right)\sin^2\theta + \left(\frac{1}{n_e^2} + r_{33}E_z\right)\cos^2\theta + r_{42}E_y \cdot 2\sin\theta\cos\theta\right](z')^2 \\
&+\left[\left(\frac{1}{n_o^2} + r_{13}E_z\right)2\sin\theta\cos\theta - \left(\frac{1}{n_e^2} + r_{33}E_z\right)2\sin\theta\cos\theta\right. \\
&\left.+r_{42}E_y \cdot 2(\cos^2\theta - \sin^2\theta)\right]y'z' = 1
\end{aligned} \tag{2.12}$$

Setting $E_z = 0$ then yields the refractive index for light with polarization along the Z'-direction,

$$n_{z'} = \frac{n_o n_e}{\sqrt{(\sin^2\theta n_e^2 + \cos^2\theta n_o^2)}}. \tag{2.13}$$

When $\vec{E} = E_z\hat{z'}$,

$$\begin{aligned}
\frac{1}{n_{z'}^2}\left(\vec{E} = E_z\hat{z'}\right) &= \frac{\sin^2\theta}{n_o^2} + \frac{\cos^2\theta}{n_e^2} + [(r_{13} + 2r_{42})\cos\theta\sin^2\theta + r_{33}\cos^3\theta]E_{z'} \\
&= \frac{1}{n_{z'}^2}\left(\vec{E} = 0\right) + [(r_{13} + 2r_{42})\cos\theta\sin^2\theta + r_{33}\cos^3\theta]E_{z'}
\end{aligned} \tag{2.14}$$

which then indicates that the effective electro-optic coefficient $r_{z'z'}$ for light with polarization along Z'-direction under E field applied in the same direction is

$$r_{z'z'}(\theta) = (r_{13} + 2r_{42})\cos\theta\sin^2\theta + r_{33}\cos^3\theta \tag{2.15}$$

Similarly, the refractive index $n_{y'}$ and the electro-optic coefficient $r_{y'z'}$ for polarization perpendicular to the E field direction can be obtained using the $(y')^2$ term in Equation 2.12,

$$n_{y'} = \frac{n_o n_e}{\sqrt{(\cos^2\theta n_e^2 + \sin^2\theta n_o^2)}} \tag{2.16}$$

$$r_{z'z'}(\theta) = r_{13}\cos^3\theta + r_{33}\cos\theta\sin^2\theta - 2r_{42}\sin^2\theta\cos\theta \tag{2.17}$$

Figure 2-3(a) plots the effective electro-optic coefficients $r_{z'z'}$ and $r_{y'z'}$ as a function of the angle θ between the applied E field and the BTO <100> axis, where experimentally measured values for r_{13}, r_{33}, and r_{42} of BTO thin film from Ref [32] are used. The maximum coefficient occurs at $\theta \approx 40°$ for $r_{z'z'}$. Hence, to maximize the refractive

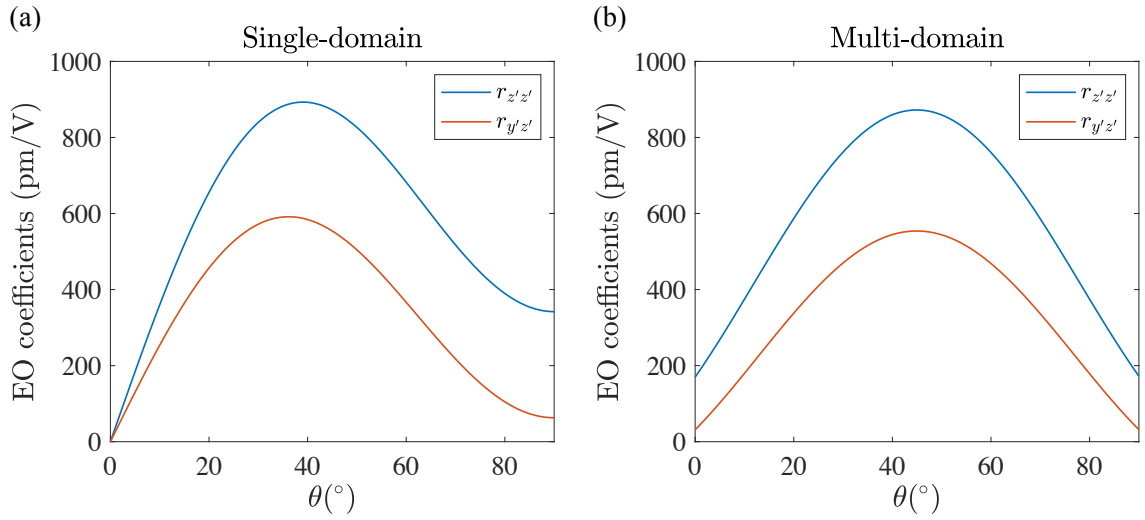

Figure 2-3: Optimization of BTO's crystalline orientation. (a) The electro-optic coefficients $r_{z'z'}$ and $r_{y'z'}$ as a function of the angle θ between the applied E field and the BTO <100> axis for a single-domain BTO thin film. (b) The electro-optic coefficients $r_{z'z'}$ and $r_{y'z'}$ as a function of the angle θ between the applied E field and the BTO <100> axis for a multi-domain BTO thin film.

index change for a given applied E field, the polarization of the light should be along the same direction as the applied E field, and the BTO crystal should be oriented such that the <100> axis is at 40° angle from the E field direction. When multi-domain BTO thin film is considered, where the <100> axis of the rectangular-shaped domains points in one of the two perpendicular in-plane directions, the effective $r_{z'z'}$ and $r_{y'z'}$ are the linear combinations of the EO coefficients for each single domain. Assuming the number of domains pointing in each of the two directions are equal, for symmetry reason, the effective $r_{z'z'}$ and $r_{y'z'}$ for multi-domain BTO thin film are then calculated and plotted in Fig. 2-3(b). The maximum coefficient now occurs at $\theta \approx 45°$ for $r_{z'z'}$. To maximize the refractive index change for a given applied E field, the polarization of the light should be along the same direction as the applied E field,

and the BTO crystal should be oriented such that the <100> axis is at 45° angle from the E field direction.

The maximum effective EO coefficient is $r_{z'z',max} = 872.01\,\text{pm/V}$ and the refractive index for this orientation is $n_{z'} = 2.289$. These parameters are used in simulation in later sections of this chapter.

The BTO thin film considered in this study requires high tetragonality and minimal porosity. Ref. [38] has provided a roadmap for achieving high electro-optic performance through the synthesis of this thin film.

Lithium niobate, with bulk Pockels coefficients r_{33} of 30.9 pm/V, is another material whose thin film form has emerged as a promising platform for integrated high-speed electro-optic modulators [31, 39, 40]. $LiNbO_3$'s crystalline lattice has the point group symmetry *3m* with a Pockels tensor in the form of

$$r_{ij} = \begin{bmatrix} 0 & -r_{22} & r_{13} \\ 0 & r_{22} & r_{13} \\ 0 & 0 & r_{33} \\ 0 & r_{42} & 0 \\ r_{42} & 0 & 0 \\ r_{22} & 0 & 0 \end{bmatrix}. \tag{2.18}$$

The indicatrix in the crystal's principal-axis coordinate system can be written as

$$\left(\frac{1}{n_o^2} - r_{22}E_y + r_{13}E_z\right)x^2 + \left(\frac{1}{n_o^2} + r_{22}E_y + r_{13}E_z\right)y^2 + \left(\frac{1}{n_e^2} + r_{33}E_z\right)z^2 + (r_{42}E_y)2yz + (r_{42}E_x)2zx + (r_{22}E_x)2xy = 1 \tag{2.19}$$

From this, one can see that the maximum Pockels effect with coefficient $r_{33} = 30.9\,\text{pm/V}$ can be achieved for light polarized in $LiNbO_3$'s <001> direction by applying an electric field along the same direction. With $LiNbO_3$ thin film, this can be done with a X-cut thin film with a horizontal electric field or a Z-cut thin film with a vertical electric field.

2.3 Design of phase-only SLMs

Spatial light modulators are divided into two main categories: phase-only SLMs and amplitude-only SLMs. Both types of devices, combined with appropriate techniques, can be used to create complex amplitude modulation and propagate into arbitrary optical fields [14, 41]. However, due to the amplitude modulation nature, amplitude-only SLMs has much lower energy efficiency compared to phase-only SLMs [42].

In practice, liquid crystal SLMs and micromirror SLMs both have implementations of the phase-only mode, but almost all other emerging high-speed electro-optic platforms are fundamentally incapable of phase-only operation. This is because in these modulation mechanisms (free carrier dispersion, quantum-confined Stark effect, and epsilon-near-zero materials), the refractive index change is associated with a change in the extinction coefficient as well, leading to an amplitude modulation coupled with the phase modulation. This unwanted coupled amplitude change contributes to undesirable diffraction of light that reduces the energy efficiency and causes inaccuracy of the image formation.

Phase-only operation is possible with the proposed SLM architecture of tunable microcavity arrays with Pockels materials. Due to the wide band gaps and the high transparency of $BaTiO_3$ and $LiNbO_3$, the Δk associated with Δn is negligible. The microcavity resonators are also designed to be over-coupled with the incident waves, which allows phase change from 0 to 2π with minimal amplitude change for the reflected waves.

This section discusses the design of phase-only SLMs based on tunable microcavity arrays. It starts from a review of the key figure-of-merits for phase-only SLMs, followed by a detailed illustration of the phase shifter pixel design methodology that combines analytical calculations with full-wave finite-difference-time-domain (FDTD) simulations. Several key concepts that are included enable the design of a high-speed phase-only spatial light modulator with CMOS-compatible driving voltages and a high diffraction efficiency.

2.3.1 Microcavity phase shifter design methodology

Portions of this section have appeared in Reference [43].

Phase-only SLMs have several key figure-of-merits: operation speed, driving voltage, diffraction efficiency, pixel size, and array size. The diffraction efficiency can be sub-divided into figure-of-merits including fill factor (the relation is explained in more detail in Sec. 2.3.2), reflection/transmission efficiency, amount of coupled amplitude change associated with the phase change, and fabrication accuracy. Table 1.1 summarizes these figure-of-merits for commercial SLMs.

To address the figure-of-merits of driving voltage, fill factor, reflection efficiency, and pixel size, I propose two concepts: (1) designs of asymmetric vertical microcavity resonator that operates in the over-coupled regime, enabled by a special design optimization methodology discussed in this section, and (2) a phase mask concept that improves the fill factor of the pixels which will be the topic of Sec. 2.3.4.

In this section, I present a systematic general approach for achieving the optimized phase shifter element design. To illustrate this design methodology, this section is based on the example geometry of a micropillar vertical cavity, shown in Figure 2-1.

In each phase shifter pixel, there is a micropillar vertical cavity with the Pockels material (BTO is used in this example) embedded inside the cavity. The layer of BTO has a thickness of one wavelength and is sandwiched between two distributed Bragg reflectors (DBRs) with alternating quarter-wavelength thickness layers of TiO_2 and SiO_2, creating a Fabry-Perot optical cavity with strongly enhanced optical field in the BTO layer. A pair of transparent conductive oxide layers on the two opposite sides of the vertical microcavity, using materials such as indium tin oxide (ITO), form a parallel plate capacitor that generates a horizontally-oriented electric field across the BTO layer when a voltage is applied. This E-field then changes the refractive index n of BTO, which in turn shifts the resonant wavelength of the optical cavity and produces a phase shift on the reflected light propagating away from the microcavity. The transparent oxide electrodes are connected to the CMOS backplane's metal contacts, allowing each pixel to be individually electrically addressed with CMOS circuits.

The complex reflection coefficient of a one-sided resonator, calculated using the temporal coupled-mode theory (TCMT), can be expressed as [44]

$$r(\omega) = \frac{(\frac{1}{\tau_e} - \frac{1}{\tau_0}) + j(\omega_0 - \omega)}{(\frac{1}{\tau_e} + \frac{1}{\tau_0}) - j(\omega_0 - \omega)} \tag{2.20}$$

where $\frac{1}{\tau_0}$ and $\frac{1}{\tau_e}$ are the intrinsic loss rate of the resonator and the coupling rate between the resonator mode and the free-space mode, respectively, and ω_0 is resonance frequency. This indicates that a detuning of the frequency from the resonance results in changes in the reflectance amplitude and phase. For the phase shifter resonator, as the voltage applied changes the refractive index of the active material BTO, the shifts in the resonant frequency then results in a detuning of the frequency from the resonance that modifies the amplitude and phase of the reflection wavefront as desired.

The regime of coupling between the resonator mode and the free space mode places an upper bound on the resonator's quality factor. Depending on the relative magnitude of the intrinsic loss rate $\frac{1}{\tau_0}$ and the resonator-free-space coupling rate $\frac{1}{\tau_e}$, the resonator's coupling to the free space mode can be categorized into three regimes: under-coupled ($\frac{1}{\tau_0} > \frac{1}{\tau_e}$), critically-coupled ($\frac{1}{\tau_0} = \frac{1}{\tau_e}$), and over-coupled ($\frac{1}{\tau_0} < \frac{1}{\tau_e}$) regimes, as illustrated in Fig. 2-4. To make sure that a full 0 to 2π reflectance phase

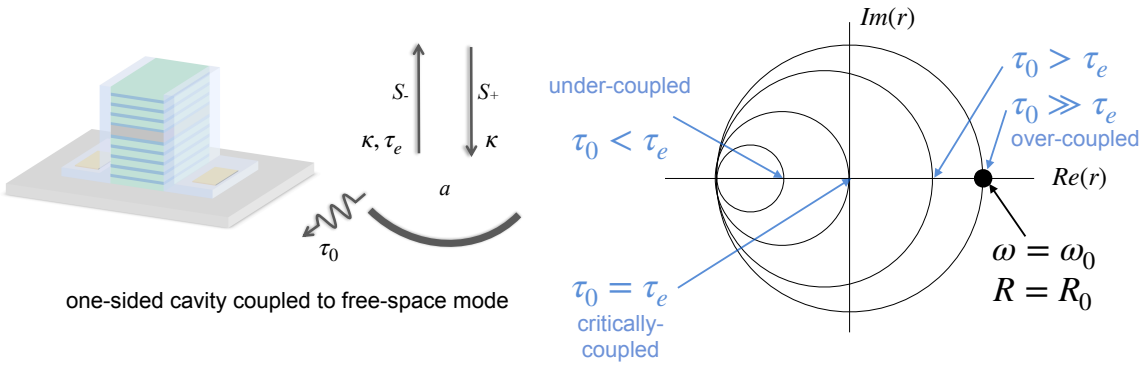

Figure 2-4: Schematic illustration for the one-sided vertical cavity coupled to the free-space mode and the reflectance in different coupling regimes between the resonator mode and the free-space mode.

shift and a minimal variation of amplitude can be achieved, the resonator mode

should be over-coupled to the free-space mode. From Equation (2.20), the reflection coefficient of the resonator at the resonance frequency $\omega = \omega_0$ can be expressed in terms of the resonator's quality factors as

$$R_0 = R(\omega = \omega_0) = \left(\frac{\frac{1}{\tau_e} - \frac{1}{\tau_0}}{\frac{1}{\tau_e} + \frac{1}{\tau_0}} \right)^2 = \left(\frac{\frac{1}{\tau_e} + \frac{1}{\tau_0} - \frac{2}{\tau_0}}{\frac{1}{\tau_e} + \frac{1}{\tau_0}} \right)^2 = \left(\frac{\frac{1}{Q_{tot}} - \frac{2}{Q_{int}}}{\frac{1}{Q_{tot}}} \right)^2 \tag{2.21}$$

where Q_{int} and Q_{tot} are the resonator's intrinsic Q and loaded Q, respectively. For the resonator to be over-coupled to the free-space and its reflection on resonance to be greater than a given value R_0, this equation then places an upper bound on the resonator's loaded Q:

$$Q_{tot} \leq \frac{1 - \sqrt{R_0}}{2} Q_{int} \tag{2.22}$$

On the other hand, the amount of frequency detuning that can be produced by a given applied voltage places a lower bound on the resonator's loaded Q. The frequency detuning can be expressed in terms of the change of the material's electric permittivity ϵ using perturbation theory as

$$\Delta\omega = -\frac{\omega_0}{2} \frac{\int d^3\vec{r} \Delta\epsilon(\vec{r}) |\vec{E}(\vec{r})|^2}{\int d^3\vec{r} \epsilon(\vec{r}) |\vec{E}(\vec{r})|^2} + \mathcal{O}(\Delta\epsilon^2) \tag{2.23}$$

The second term represents the second and higher order effects and is negligible when $|\Delta\epsilon/\epsilon| < 1\%$. Since $n = \sqrt{\epsilon}$, we have $\Delta\epsilon \approx 2\epsilon\Delta n/n$. The detuning can then be written as

$$\begin{aligned} \Delta\omega &= -\frac{\omega_0}{2} \frac{\int d^3\vec{r} 2\epsilon(\vec{r}) \Delta n(\vec{r})/n(\vec{r}) |\vec{E}(\vec{r})|^2}{\int d^3\vec{r} \epsilon(\vec{r}) |\vec{E}(\vec{r})|^2} \\ &= -\omega_0 \frac{\int_{BTO} d^3\vec{r} \epsilon(\vec{r}) \Delta n(\vec{r})/n(\vec{r}) |\vec{E}(\vec{r})|^2}{\int d^3\vec{r} \epsilon(\vec{r}) |\vec{E}(\vec{r})|^2} \\ &= -\omega_0 \frac{\Delta n}{n_0} \frac{\int_{BTO} d^3\vec{r} \epsilon(\vec{r}) |\vec{E}(\vec{r})|^2}{\int d^3\vec{r} \epsilon(\vec{r}) |\vec{E}(\vec{r})|^2} \\ &= -\omega_0 \frac{\Delta n}{n_0} \frac{U_{BTO}}{U_{tot}} \end{aligned} \tag{2.24}$$

where n_0 is the refractive of BTO without applied E field. From Equation (2.20), the

detuning needed to produce a π phase shift (from $-\pi/2$ to $\pi/2$) is

$$\Delta\omega_\pi = 2\left(\frac{1}{\tau_e} - \frac{1}{\tau_0}\right) = \frac{\omega_0}{Q_{tot}} - \frac{2\omega_0}{Q_{int}} \tag{2.25}$$

which according to Equation (2.24) corresponds to a refractive index change of

$$\begin{aligned} \Delta n_\pi &= -n_0 \frac{\Delta\omega_\pi}{\omega_0} \frac{U_{tot}}{U_{BTO}} \\ &= -n_0 \left(\frac{1}{Q_{tot}} - \frac{2}{Q_{int}}\right) \frac{U_{tot}}{U_{BTO}} \end{aligned} \tag{2.26}$$

Hence for a given Δn to produce a phase shift greater than π,

$$Q_{tot} \geq \frac{1}{\frac{\Delta n}{n_0}\frac{U_{BTO}}{U_{tot}} + \frac{2}{Q_{int}}} \tag{2.27}$$

This is a lower bound on the resonator's loaded Q.

Figures 2-5(a) and 2-5(b) illustrate Q_{max} and Q_{min}, the upper and lower bounds for the loaded Q, respectively, for various values of reflection on resonance and applied electrical voltages.

The intrinsic Q for microcavities with varying widths D is calculated by simulating the resonator with perfectly reflecting DBR mirrors on both sides of the BTO layer. 15 pairs of TiO_2/SiO_2 quarter-wavelength stacks are found to exhibit approximately perfect reflectivity with negligible longitudinal transmission loss. The optical absorption in BTO is assumed to be zero in the simulation because BTO is a highly transparent material and optical waveguides with very low loss have been demonstrated in thin-film BTO in both visible and near-infrared wavelengths [45, 32]. The value of the fraction of energy in the BTO layer U_{BTO}/U_{tot} simulated for the intrinsic cavity is used to plot Q_{min}, hence representing a stricter lower bound. The Δn corresponding to the voltage applied is calculated assuming a parallel-plate capacitor is formed by the two vertical ITO layers.

Having established the upper and lower bounds of the resonator's loaded Q, the design parameters of the resonator (the width of the vertical micropost D and the

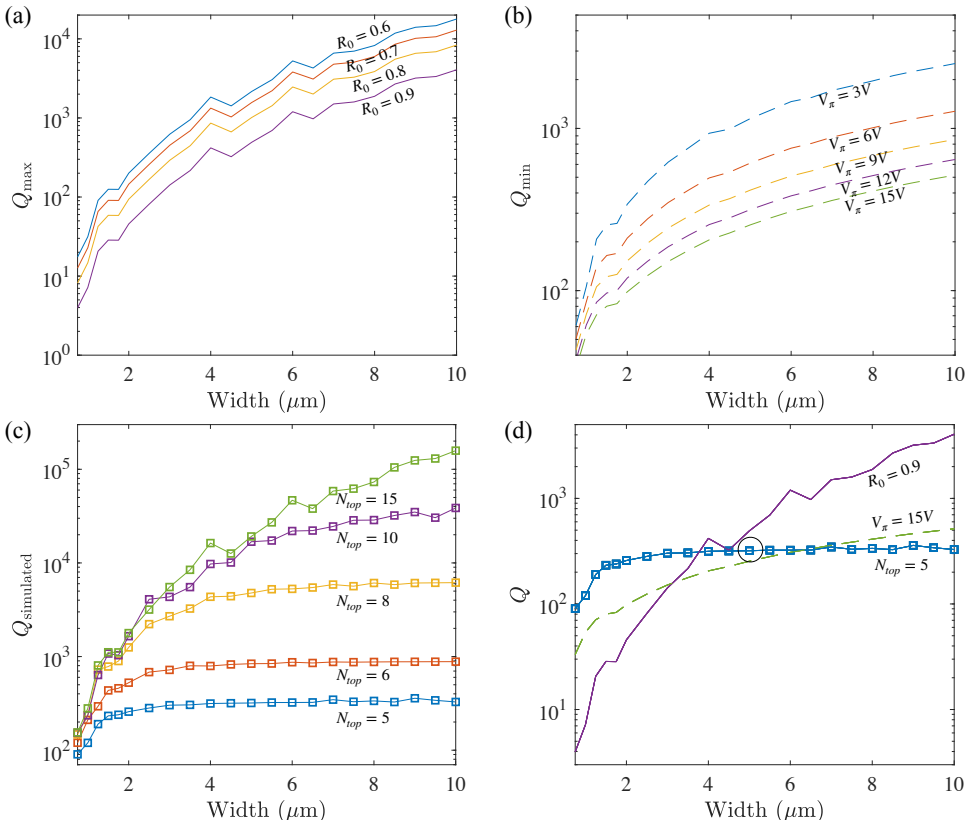

Figure 2-5: Quality factor analysis of the microcavity resonators. (a) Maximum loaded Q for the reflectance to be greater than certain values. (b) Minimum loaded Q for V_π, the voltage required to achieve π phase shift, to be less than certain values. (c) Simulation of cavity loaded Q for different micropost widths D and number of TiO_2/SiO_2 quarter-wavelength pairs N_{top}. (d) For $D = 5\,\mu m$ and $N_{top} = 5$, the reflectance can be maintained above $R = 0.9$ and the voltage for π phase shift is $< 15V$.

number of pairs of TiO_2/SiO_2 quarter-wavelength stacks in the top DBR mirror N_{top}) can then be selected by sweeping the parameters and searching for the optimal design that satisfies the bounding restrictions. Figure 2-5(c) shows the simulated loaded Q for resonators with various D and N_{top}. If we narrow the design criteria to be $R_0 > 0.9$ and $V_\pi < 15V$ while keeping the resonator width (hence the pixel pitch of the SLM) as small as possible, we then end up with a set of design parameters: $D = 5\,\mu m$ and $N_{top} = 5$, as illustrated in Fig. 2-5(d).

Optimized phase shifter elements resonator design

The optimized phase shifter element design achieves a full 0 to 2π phase control of the reflected light while keeping the reflectance amplitude nearly constant, enabling phase-only modulation. Figure 2-6(a) shows the reflectance spectrum of the optimized resonator and Fig. 2-6(b) shows the modulation characteristics of the resonator as a function of the modulated refractive index of the active material BTO. The reflectance

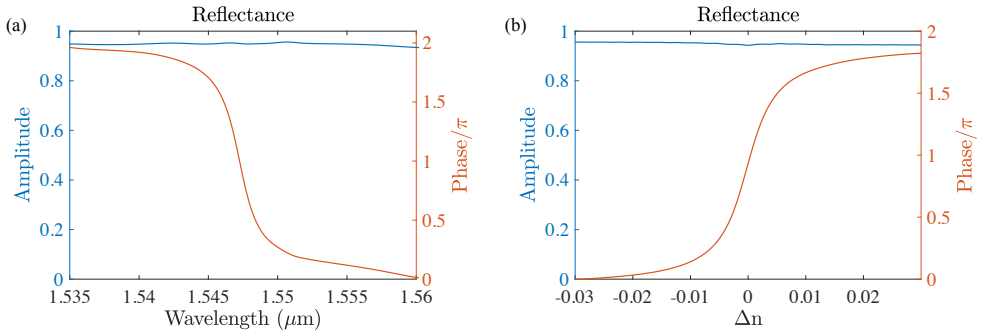

Figure 2-6: Optimized phase shifter element with design parameters $D = 5\,\mu m$ and $N_{top} = 5$. (a) The reflectance spectrum. (b) The modulation characteristics as a function of the refractive index change of the active layer BTO.

amplitude is maintained at $R > 0.9$ across the modulation range, and the required voltage to reach a π phase shift (corresponding to $\Delta n \sim 0.01$) is $V_\pi = 9.3V$, both agree well with the prediction from the quality factor analysis performed above.

To facilitate coupling of the cavity mode with the free-space mode, higher-order waveguide modes that can propagate vertically in the DBR layers of the micropost should be suppressed. This can be achieved by adding an extra quarter-wavelength layer of TiO_2 to the top of the micropost and etching a circular hole at the center

of the layer, as illustrated in Fig. 2-1(a). This extra quarter-wavelength layer causes constructive interference at the center of the micropost and destructive interference at the peripheral areas, effectively enhancing the fundamental mode of the DBR waveguide layers and suppressing the higher-order modes. Figure 2-7(a) illustrates the E field intensity and phase profile at the top surface of the micropost. The

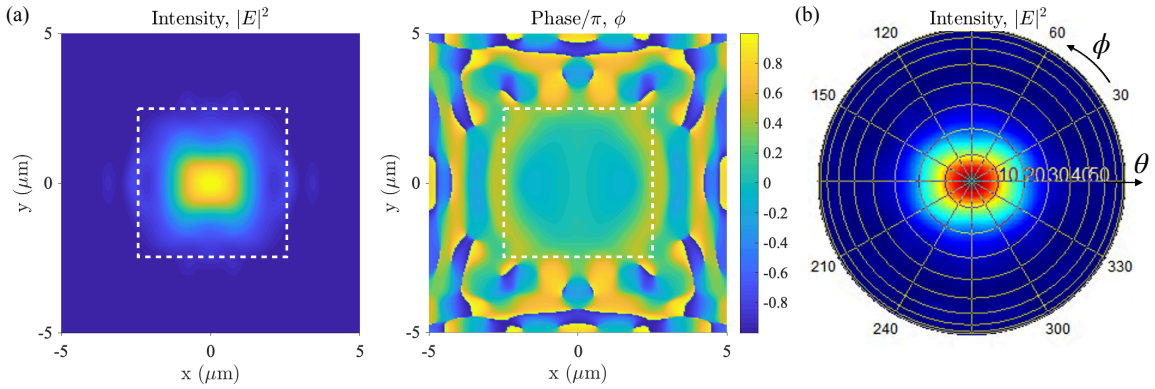

Figure 2-7: Optimized phase shifter element with design parameters $D = 5\,\mu\text{m}$ and $N_{top} = 5$. (a) Near-field intensity and phase profiles of the top surface of the microcavity at $\lambda = 1547\,\text{nm}$. The dashed box represents the outline of the microcavity's top surface. (b) Far-field intensity profile of the microcavity's radiation at $\lambda = 1547\,\text{nm}$.

concentrated E field at the center of the post indicates the fundamental waveguide mode is successfully maintained as the cavity mode propagates vertically through the DBR waveguide layers. The uniform phase distribution in regions that present strong field intensities ensures that all light reflected from a single phase shifter has the same correct phase set by the applied voltage. The far-field radiation profile of this single element is shown in Fig. 2-7(b), which according to Equation 2.2 represents the envelope function of the far-field radiation profile of the entire two-dimensional microcavity array. The strongly concentrated field strength at the center indicates that the majority of the reflected power is distributed to the first few diffraction orders in the far field. This ensures high diffraction efficiency for most applications, where only the main diffraction lobe is of interest.

Further mode matching between the free-space mode, for example an incident light beam that has a Gaussian mode profile, and the resonator mode can be accomplished by placing a phase mask or a microlens array in front of the two-dimensional micro-

Table 2.1: **Parameters used in FDTD simulation of micropillar vertical cavities.**

Parameter	Description	Value
λ_d	Design wavelength	1550 nm
n_{SiO_2}	Refractive index of SiO_2	1.457[47]
n_{TiO_2}	Refractive index of TiO_2	2.3893[47]
n_{BTO}	Refractive index of BTO	2.286[32]
$n_{b,BTO}$	Optical birefringence of BTO	0.03[32]
r_{42}, r_{33}, r_{13}	Pockels coefficients of BTO	923, 342, −63 pm/V[32]
d	Thickness of the cavity layer	678 nm
N_{top}	Pairs of DBRs above the cavity layer	5
N_{bottom}	Pairs of DBRs below the cavity layer	15
D	Width of the vertical microcavity pillar	5 µm

cavity array to change the wavefront of the incident beam to a designed wavefront profile so that the light incident on each phase shifter is matched to the waveguide mode of the input port of each microcavity.

The simulation is done with the finite-difference time-domain method using the commercially available software Lumerical FDTD Solutions [46]. The parameters used in the simulation are summarized in Table 2.1. The determination of effective Pockels coefficient of BTO used in the simulation is discussed in Section 2.2.1.

2.3.2 Wavefront modulation and far-field beam forming

Portions of this section have appeared in Reference [43].

As mentioned earlier, when the vertical microcavities are arranged in a 2D array, where each of them is controlled independently and simultaneously, a spatially variant phase distribution on the wavefront of the reflected light can be generated and then propagated to the far field to form an arbitrary optical field. The far-field radiation pattern is related to the near-field profile according to

$$\begin{aligned} U(x,y,z) &= \int_{-\infty}^{\infty}\int_{-\infty}^{\infty} A(f_x,f_y,0)e^{j2\pi\sqrt{\frac{1}{\lambda^2}-f_x^2-f_y^2}}e^{j2\pi(f_x x+f_y y)}df_x df_y \\ &= U_1(\theta,\phi,z)F_a(\theta,\phi,z) \end{aligned} \tag{2.28}$$

where $U(x,y,z)$ is the far-field spatial profile of the reflected light from the SLM,

$A(f_x, f_y, 0)$ is the Fourier transform of the near-field spatial profile of the reflected light as a function of the spatial frequencies f_x and f_y, $U_1(\theta, \phi, z)$ is the far-field radiation field of a single pixel, $F_a(\theta, \phi, z)$ is the array factor of the system and λ is the wavelength of light.

Essentially, the far-field profile of the SLM consists of light reflected into a number of diffraction orders, the polar and azimuth angles of which are determined by the pixel pitch of the SLM. If there are many pixels in the SLM, there will be negligible overlap of different diffraction orders. The field distribution within each diffraction order can be controlled by the spatial phase distribution of the wavefront reflected from all the pixels. Using phase retrieval algorithms such as the Gerchberg-Saxton algorithm [33], the required phase from each pixel can be calculated and set by the corresponding control voltage, allowing an arbitrary desired far-field pattern to be generated in each diffraction order.

The power distribution of light reflected into each diffraction order is determined by the single pixel far-field pattern $U_1(\theta, \phi, z)$ which can be thought of as an "envelope" function. If the fill factor is close to 1, this envelope function would span an angular range such that the power diffracted to the 1st order or higher is negligible. On the contrary, if the fill factor is much less than 1, more diffraction orders would fit in the envelope function and less power would be in the 0th order that is of interest. This is the reason why a larger fill factor leads to a higher diffraction efficiency.

With the optimized phase shifter elements design, this section demonstrates dynamical beam steering and beam focusing using the phase-only spatial light modulator consisting of the phase shifters arranged in a large-scale two-dimensional array.

Dynamical 2D continuous beam steering can be achieved by assigning a phase profile to the shifter array that represents a phase gradient in the steering direction

$$\frac{d\phi}{dx} = \frac{2\pi}{\lambda} \sin(\theta_r) \tag{2.29}$$

where ϕ is the phase of the reflected light, x is the spatial coordinate along the steering direction and θ_r is the reflection angle of the reflected light. Figure 2-8(a)

shows simulation of the continuous beam steering for a range of phase gradients $\frac{d\phi}{dx}$ from 0.2π / pixel to π / pixel where the intensity of the E field $|E|^2$ in the far-field is plotted. Figure 2-8(b) shows two line-cuts from Fig. 2-8(a), representing $\frac{d\phi}{dx} = 0.35\pi$ / pixel and $\frac{d\phi}{dx} = 0.85\pi$ / pixel respectively. The peaks in the far-field intensity

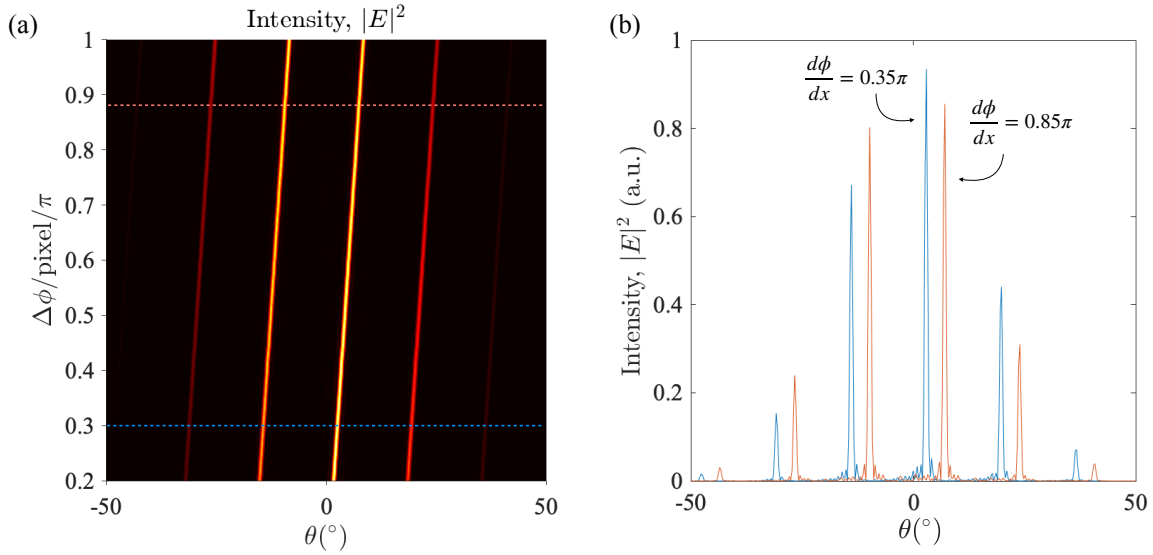

Figure 2-8: Demonstration of dynamical continuous beam steering using a 20×20 array of phase shifters. (a) Far-field reflection pattern for phase profile representing phase gradients ranging from 0.2π / pixel to π / pixel. (b) Line-cuts from (a) corresponding to $\frac{d\phi}{dx} = 0.35\pi$ / pixel (blue) and $\frac{d\phi}{dx} = 0.85\pi$ / pixel (red).

correspond to the zeroth, first, and second diffraction orders, due to larger pitch size $a = 5.2\,\mu\text{m}$ of the phase shifter array compared to the wavelength of light $\lambda = 1550\,\text{nm}$ used. Power diffracted to orders higher than the second are negligible. The diffraction efficiency (fraction of power directed to the 0th order beam) is $\sim 16\%$ and is similar for all steering angles considered. Importantly, no unsteered beams ("ghost spots") remain at 0 phase gradient diffraction locations. This is a result of the phase-only modulation capability of the individual phase shifters which contributes to the high diffraction efficiency of the spatial light modulator design.

The far-field intensity profile is calculated by first sampling the simulated near-field profile of each phase shifter above the Nyquist limit (corresponding to 18 points per pixel), then combining the individual profiles to form a large-scale profile of the 2D array, and finally analytically propagating the near-field profile to the far field using

Angular Spectrum Method. The simulated near-field profile of the individual phase shifter is sampled at 45 discrete phase levels in an index change range of $\Delta n = 0.06$. In this simulation, a 20×20 array of phase shifters are arranged into a two-dimensional array with pitch size $a = 5.2\,\mu\text{m}$. Negligible coupling between the individual phase shifters is confirmed by checking that the FDTD-simulated far-field profile agrees with the analytical far-field profile calculated with Angular Spectrum Method.

Similarly, a dynamically tunable varifocal lens can be achieved by assigning a phase profile to the shifter array that follows a hyperbolic relation

$$\phi(x, y) = \phi(0, 0) + \frac{2\pi}{\lambda}(f_0 - \sqrt{x^2 + y^2 + f_0^2}) \tag{2.30}$$

where $\phi(0, 0)$ is the reflected phase of the center pixel and f_0 is the focal length of the lens. Phase profiles that correspond to different focal lengths can be dynamically

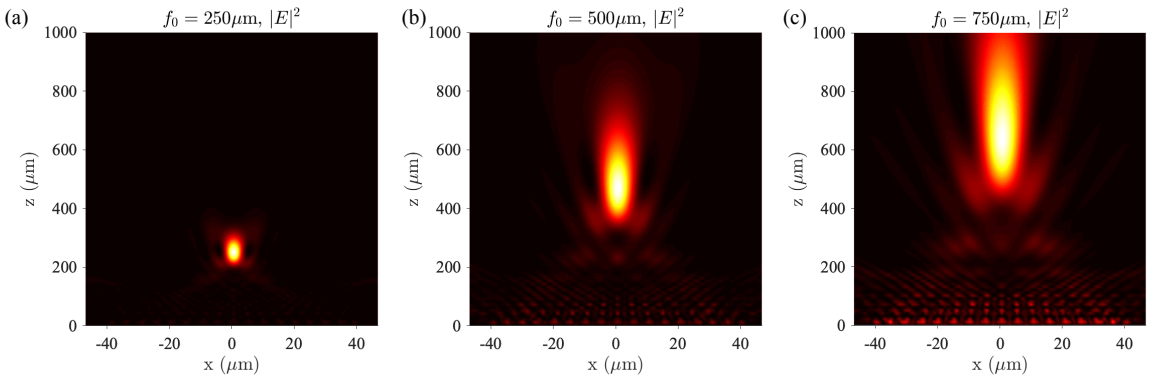

Figure 2-9: Demonstration of dynamical beam shaping (a varifocal metalens) using a 16×16 array of phase shifters. Intensity profiles for focusing of light at focal lengths (a) $f_0 = 250\,\mu\text{m}$, (b) $f_0 = 500\,\mu\text{m}$, and (c) $f_0 = 750\,\mu\text{m}$. z is the direction of reflected light propagation.

assigned to the SLM pixels and the reflected light can then be focused at different distances from the SLM surface. Figure 2-9 demonstrates the dynamical tuning of the focal length of the reflected light, with the focal length set to $f_0 = 250\,\mu\text{m}$, $f_0 = 500\,\mu\text{m}$, and $f_0 = 750\,\mu\text{m}$, respectively. The focusing efficiency (fraction of power in the 0th order beam) is calculated to be $\sim 17.5\%$ and is similar for all three focal lengths demonstrated.

2.3.3 Design for CMOS-compatible driving voltages

The conceptually simple micropillar geometry considered in Sec. 2.3.1 and Sec. 2.3.2 requires a voltage of $9.3V$ to modulate the reflected phase from 0 to π. This is a significant increase in the phase shift compared to that provided by a Pockels thin film of the same thickness without microcavity amplification. However, it is still challenging for standard high-speed CMOS transistor backplanes nowadays to provide driving voltages that are higher than $5V$ [48].

With the same Pockels materials and coefficients, the only ways to further reduce the driving voltage is to increase the loaded Q of the microcavity and decrease the width across which the electric field is applied. This section demonstrates another vertical microcavity design that promises a higher loaded Q, a smaller footprint, and hence a smaller driving voltage that is standard-CMOS-compatible.

As seen in Sec. 2.3.1, the loaded Q of the microcavity is upper-bounded by the microcavity's intrinsic Q by

$$Q_{\text{tot}} \leq \frac{1-\sqrt{R_0}}{2} Q_{\text{int}} \tag{2.31}$$

where R_0 is the reflectivity of the microcavity at the resonant wavelength. This implies that to increase the loaded Q, the microcavity's intrinsic Q needs to be increased. The intrinsic Q of the cavity, defined as the Q of the cavity where both the upper and lower DBRs have infinite reflectivity, is determined by the transverse scattering loss due to the small lateral size of the vertical cavity. This can be understood from a perspective of spatial Fourier transform of the mode profile of the microcavity. When the mode is highly confined in the spatial domain in the (x, y)-direction, the wave-vector components (k_x, k_y) are then not well-confined, leading to light waves escaping from the cavity and a degraded cavity quality factor.

To reduce the transverse scattering loss and increase the cavity's Q as an attempt to reduce the driving voltage, I propose using an one-sided vertical cavity geometry where the lateral mode confinement is provided by a Gaussian-shaped defect. This vertical microcavity geometry is illustrated in Fig. 2-10. The confinement of the

optical mode in the vertical direction is provided by distributed Bragg reflectors above and below the active material layer, and in the horizontal direction, a Gaussian-shaped confinement potential is provided by an index perturbation created by a "defect" above the active material layer. Previous work by Ding et al. [49] has shown that a

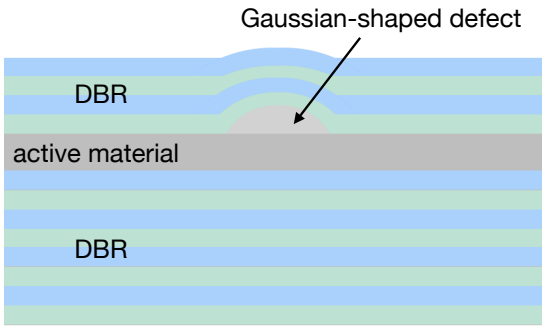

Figure 2-10: Spatial light modulator phase shifter pixel consisting of an one-sided vertical microcavity where the lateral optical confinement is provided by a Gaussian-shaped defect. DBR: distributed Bragg reflector.

theoretical intrinsic Q of up to 10^5 can be achieved even when the width of the defect is well below 1 µm. This is in stark contrast to micropillar vertical cavities introduced in previous sections, whose intrinsic Q drops to below 100 when the width becomes smaller than 1 µm.

In addition, a Gaussian-shaped defect also shows superior cavity intrinsic Q compared to defects of other shapes, including mesa and spherical shapes. The simulated intrinsic Q for these different defect shapes and a variety of geometrical parameters is summarized in Fig. 2-11, demonstrating a one to two orders of improvement of intrinsic Q for vertical cavities with Gaussian-shaped defects.

With the higher intrinsic Q, the upper bound of the loaded Q, according to Eq. 2.31, can be elevated. At the same time, since this high intrinsic Q is maintained even when the defect width becomes less than 1 µm, the same driving voltage can induce a stronger electric field thanks to a shortened voltage drop distance, leading to a larger refractive index change and a lowered $Q_{\min}$, according to Eq. 2.27. The net result of this expanded range of possible loaded Q's is that now a design with standard-CMOS-compatible driving voltage is possible in the phase-only modulation

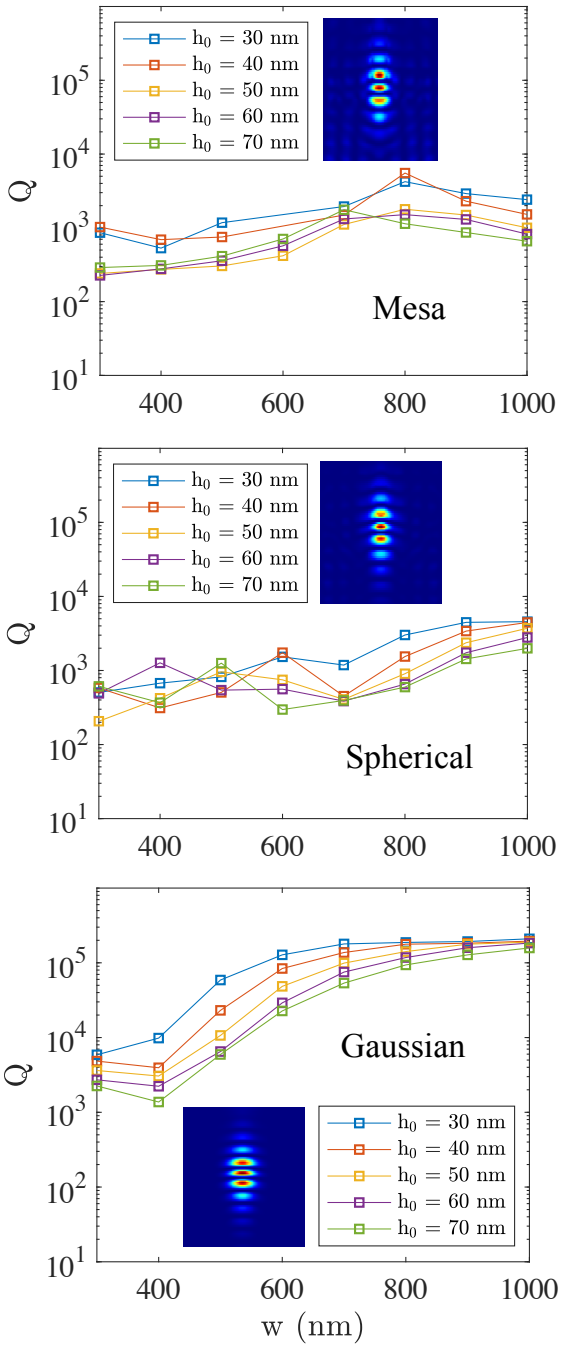

Figure 2-11: Intrinsic quality factors of vertical microcavities whose lateral optical confinement is provided by defects with mesa, spherical, and Gaussian shapes. $h0$: Height of defect. w: Width of defect.

regime with Pockels effect.

Fig. 2-12(a) illustrates $Q_{\max}$ and $Q_{\min}$, the upper and lower bounds for the loaded Q, respectively, for various values of reflection on resonance and applied electrical voltages. Fig. 2-12(b) shows the region of acceptable loaded Q with design criteria $R_0 > 0.9$ and $V_\pi < 2\,\mathrm{V}$. Fig. 2-12(c) shows the simulated loaded Q for resonators with various w and N_{top}, overlaid on Fig. 2-12(b). This then indicates that a vertical microcavity with $w = 600\,\mathrm{nm}$ and $N_{\mathrm{top}} = 7$ can reach a reflectance on resonance of above $R = 0.9$ and a V_π below $2\,\mathrm{V}$.

The modulation characteristics of this optimized resonator design is shown in Fig. 2-13, confirming that the reflectance amplitude is maintained at $R > 0.9$ across the modulation range, and the required voltage to reach a π phase shift is $V_\pi < 2\,\mathrm{V}$ which is compatible with standard CMOS processes, both agree well with the prediction from the quality factor analysis performed above.

2.3.4 Design for high diffraction efficiencies

With this design, the SLM phase shifter pixels can be driven at a voltage level that is compatible with the state-of-the-art standard CMOS circuits, where post process steps will be used to deposit the dielectric layers required and define pixels with corresponding metallic contacts. A schematic cross section of this two-dimensional array of phase shifter pixels on a CMOS backplane is illustrated in Fig. 2-14.

As discussed previously in Sec.2.3.2, the diffraction efficiency of an SLM design is directly related to the fill factor of each pixel's near-field profile. However, due to the following reasons, the fill factor is limited for the current design:

1. The laterally-confined nature of the microcavity's optical mode results in a confined near field profile, as shown in Fig. 2-15.

2. Due to the anisotropic nature of the Pockels material under consideration ($BaTiO_3$), the electric field has to be applied horizontally, implying that the electrodes have to be in the same plane as the active material and occupy some area of the pixel.

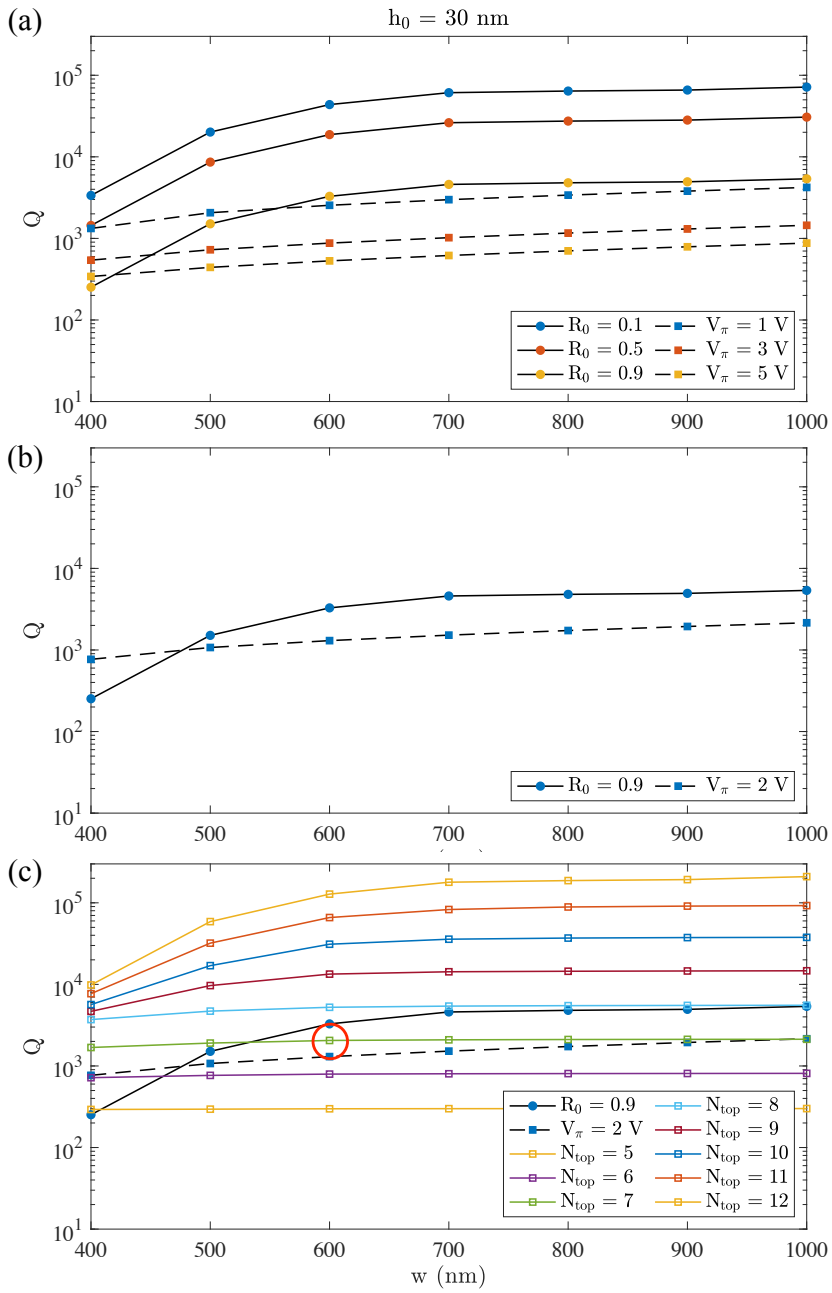

Figure 2-12: Quality factor analysis of the Gaussian-defect vertical cavity. (a) Maximum (solid) and minimum (dash) loaded Q for the reflectance to be greater than certain values and for the voltage required to achieve a π phase shift to be less than certain values. (b) Maximum and minimum loaded Q for the reflectance to be greater than 0.9 and for the V_π to be less than 2 V. (c) Simulation of cavity loaded Q for different defect widths, w, and number of TiO_2/SiO_2 quarter-wavelength pairs in the top DBR, N_{top}. For $w = 600$ nm and $N_{\text{top}} = 7$, the reflectance can be maintained above $R = 0.9$ and the voltage for π phase shift is < 2 V.

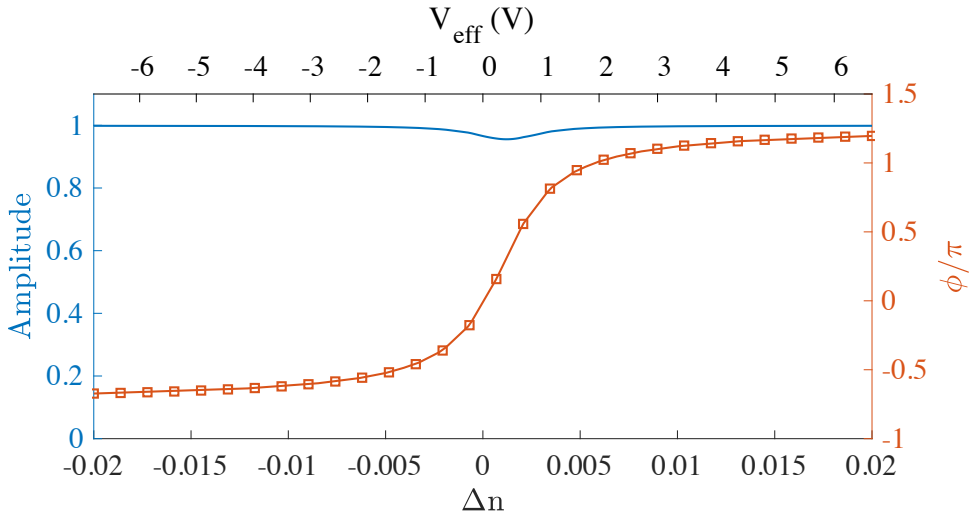

Figure 2-13: Modulation characteristics of the optimized Gaussian-defect vertical microcavity phase shifter element with design parameters $D = 600\,\text{nm}$ and $N_{\text{top}} = 7$.

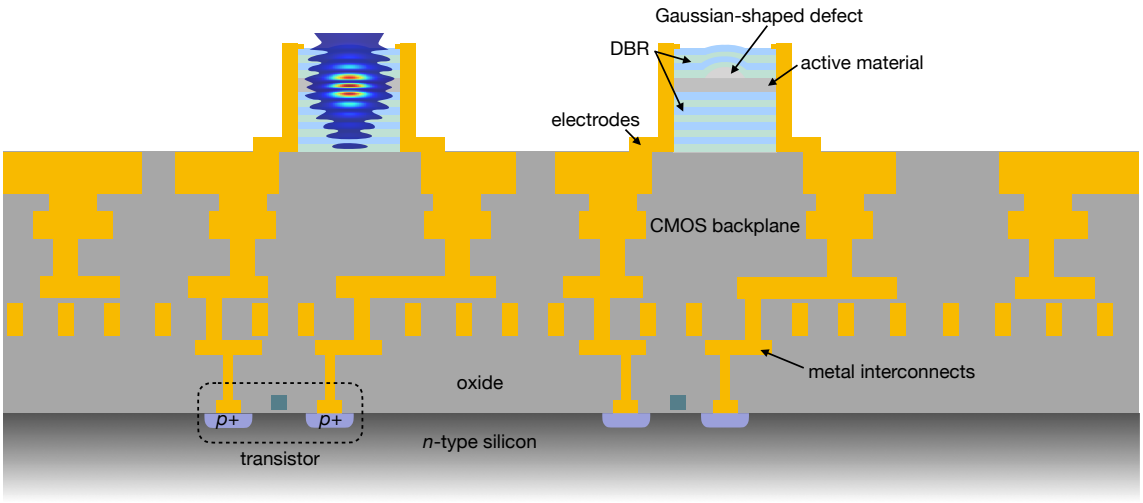

Figure 2-14: Schematic cross section of spatial light modulators with two-dimensional tunable microcavity arrays on a complementary metal-oxide-semiconductor (CMOS) backplane. Each phase shifter pixel consists of a one-sided vertical microcavity laterally confined by a Gaussian-shaped defect, with electrical contacts connected to the CMOS driving circuit.

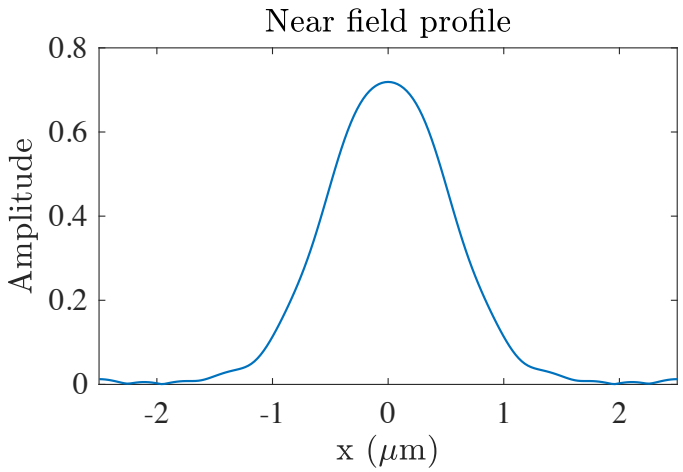

Figure 2-15: The near-field profile of the optimized Gaussian-defect vertical microcavity phase shifter element with design parameters $D = 600\,\text{nm}$ and $N_{\text{top}} = 7$.

3. Optical coupling and cross-talk between neighboring pixels can significantly influence the phase relationship between those pixels. To ensure independent addressing of the pixels, it is best to place them far enough apart such that there is minimal optical coupling.

To enhance the fill factor and subsequently the diffraction efficiency of the proposed SLM architecture, I propose the insertion of a phase mask a short distance above the near field of the pixels, aiming to convert the limited fill factor at the pixel near field to an almost unity fill factor, without compromising the intended phase pattern of the phase shifter arrays.

This phase mask concept is illustrated in Fig. 2-16. The optical mode coupled out from each phase shifter pixel starts out with a small factor. The outgoing wave propagates a short distance from the pixel surface (at z_1), during which the optical mode expands due to diffraction to fill up the full pixel at z_2. From z_1 to z_2, the optical waves from neighboring pixels do not interfere, hence remaining the same phase relation as the near field which is controlled by each pixel's voltage. However, the wavefront within each pixel has gained a curvature due to the diffraction, which means that at the plane z_2, each pixel has a high fill factor but the phase is nonuniform. This curved wavefront would lead to an envelope of the far-field radiation that has a broad angular range. Multiple diffraction orders within this envelope then degrades

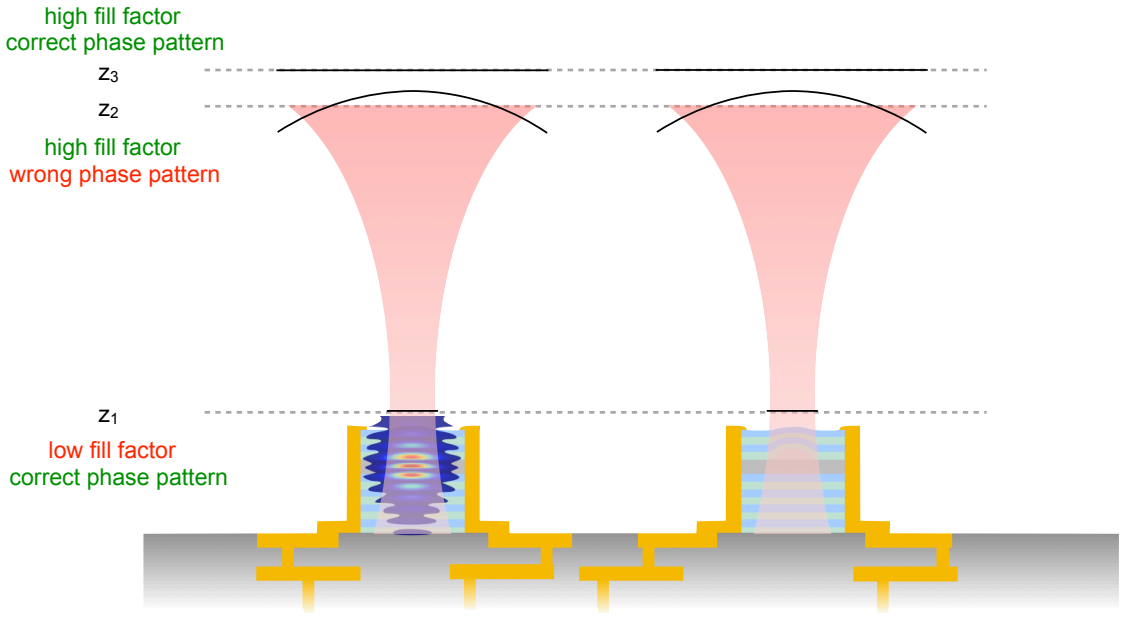

Figure 2-16: The insertion of a phase mask at a short distance above the phase shifter pixels allows conversion of a small fill factor to near unity without compromising the intended phase pattern.

the diffraction efficiency. If, instead of this curved wavefront, a flat wavefront is generated by inserting a static phase mask that compensates the phase difference due to diffraction within each pixel, then a high fill factor can be realized at the same time with a flat wavefront and the correct phase pattern set by the pixels. This would then lead to a far-field radiation envelope with smaller angular range and a higher power fraction that is diffracted into the 0th diffraction order.

The phase profile of the phase mask can be obtained using the following procedure.

1. Simulate the out-coupled microcavity mode;
2. Propagate this mode to the location of the mask;
3. Calculate the phase of the optical field at this location;
4. Use the inverse of the phase profile calculated in Step 3 as the phase profile of the mask.

Since there is no interference of waves during the propagation between the near field and the phase mask, the phase extracted from Step 3 accurately represents the

phase curvature within each pixel. Assuming that the phase profile of the microcavity near field remains the same for different modulated phase settings (which is true for single mode microcavities under consideration here), the same phase mask then correctly converts the wavefront when the phase shifter pixel is set to a different phase value. In other words, a static phase mask is capable of the fill factor conversion even when the phase shifter pixels are dynamically modulated.

The effect of this phase mask concept is numerically demonstrated in Fig 2-17. Fig 2-17(a)-(b) plot the amplitude and phase of the out-coupled microcavity mode during propagation from the near field to the phase mask, where the near field is obtained from the FDTD simulated profile of each phase shifter using the same sampling method as discussed in Sec. 2.3.2. This propagation shows the increase of the fill factor and the curving of the wavefront. Fig 2-17(c) plots the far field of the SLM array without the phase mask, showing the presence of several diffraction orders. If

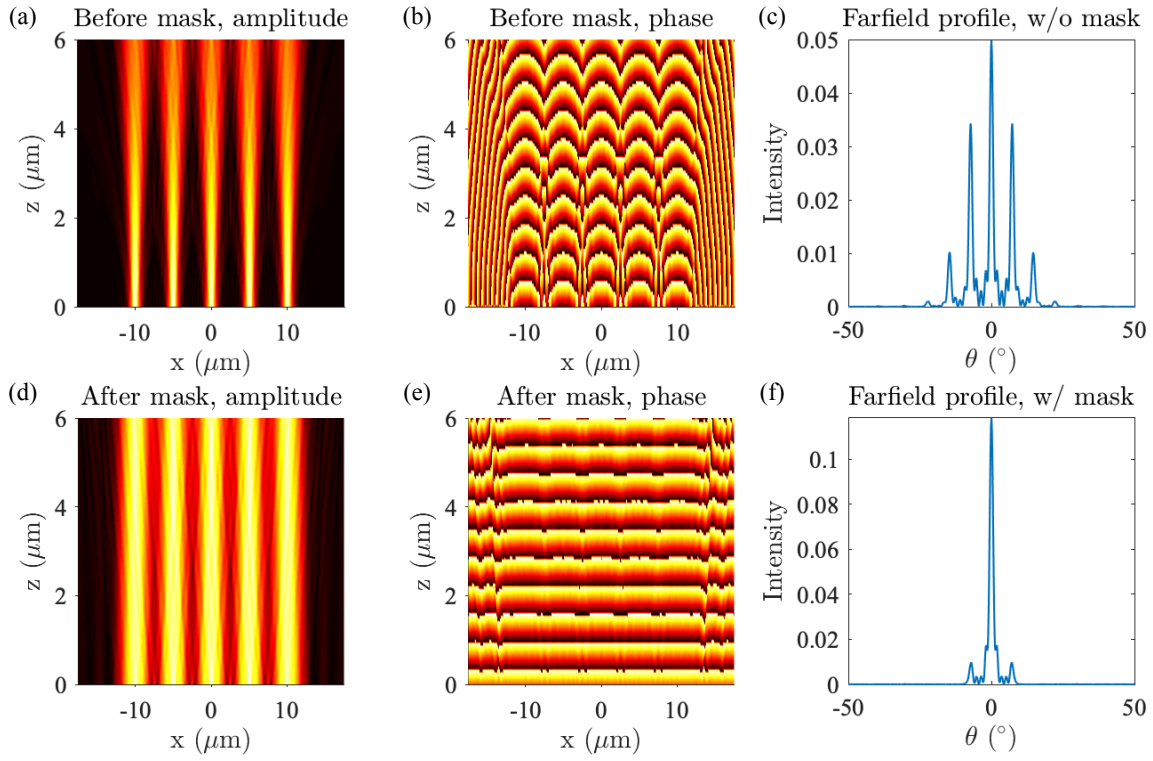

Figure 2-17: The fill factor conversion phase mask. (a)

the phase mask is inserted at $z_2 = 6\,\mu\text{m}$ to correct the curved wavefront, the optical waves after the phase mask would then resemble those coming from a near field with

almost unity fill factor with a flat phase within each pixel, as shown in Fig 2-17(d)-(e). The resultant far field profile of this SLM array with the phase mask, plotted in Fig 2-17(f), then shows only the 0th order diffraction peak with a very small amount of power diffracted to the 1st orders.

Fig. 2-18 demonstrates dynamical continuous far-field beam steering of this architecture, showing enhanced diffraction efficiency as a result of this phase mask concept. By assigning a phase profile to the shifter array that represents a phase gradient in the steering direction, the beam is scanned to different angles in the far field. Fig. 2-18(a) shows the far field without the phase mask, while Fig. 2-18(b) shows that with the phase mask. Again, without the phase mask, the small fill factor leads to several

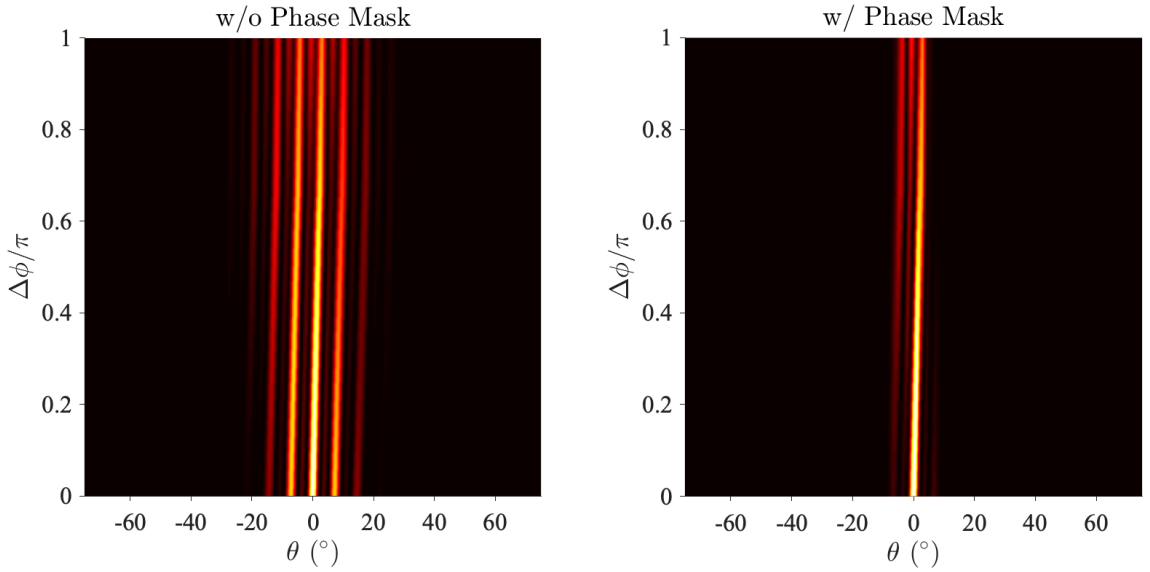

Figure 2-18: Comparison of far-field dynamical beam steering. (a) Far-field intensity without the phase mask. (b) Far-field intensity with the phase mask.

diffraction orders in the far field, and with the mask, the enhanced fill factor significantly suppresses power in higher diffraction orders and redirects that power into the 0th order peak, leading to high diffraction efficiency. This dynamical beam steering simulated using the static phase mask, obtained according to the above outlined procedure, also confirms that this phase correction of a dynamically modulated surface can be done with a passive, static phase mask.

The total SLM efficiency can then be calculated by taking into account the diffrac-

tion efficiency from the out-coupled mode to the far-field diffraction order of interest, combined with the in-coupling efficiency from the incoming plane wave to the phase shifter pixels:

$$\text{(Total SLM efficiency)} = \text{(In-coupling efficiency)} \times \text{(Diffraction efficiency)}. \quad (2.32)$$

Due to reciprocity, an incident plane wave passing through the phase mask with the curved phase profile will focus the plane wave onto each phase shifter pixels. This increases the in-coupling efficiency compared to the case where a large amount of the plane wave is incident on the empty space between the pixel's active areas. This process is demonstrated in Fig. 2-19.

Overall, the increased in-coupling efficiency and the increased diffraction efficiency thanks to the insertion of this phase mask results in a high total energy efficiency of the system.

2.3.5 Design for a trivial fabrication process

In an attempt of a proof-of-principle demonstration of a high-speed SLM with tunable microcavity arrays and Pockels thin film materials, I have also designed a vertical microcavity geometry, where the ease of fabrication is the primary concern.

Illustrated in Fig. 2-20, this vertical microcavity array consists of a planar one-sided vertical cavity where the lateral optical confinement is provided by a microlens array outside the cavity. Plane wave incident on the microlens array creates localized focused beams and each of them is incident on a phase shifter pixel containing a set of electrodes that create an electric field across the active material.

This geometry allows the direct integration of a continuous active material thin film without the development of precise etching and 3D lithography process to define the micropillar or Gaussian defect shape. The subsequent deposition of the microlens array can be integrated at large scale with the nanoimprinting method [50]. On the other hand, there are two downsides of this geometry. First, due to the external lateral optical confinement mechanism, to avoid divergence of the beam, the cavity's Q is

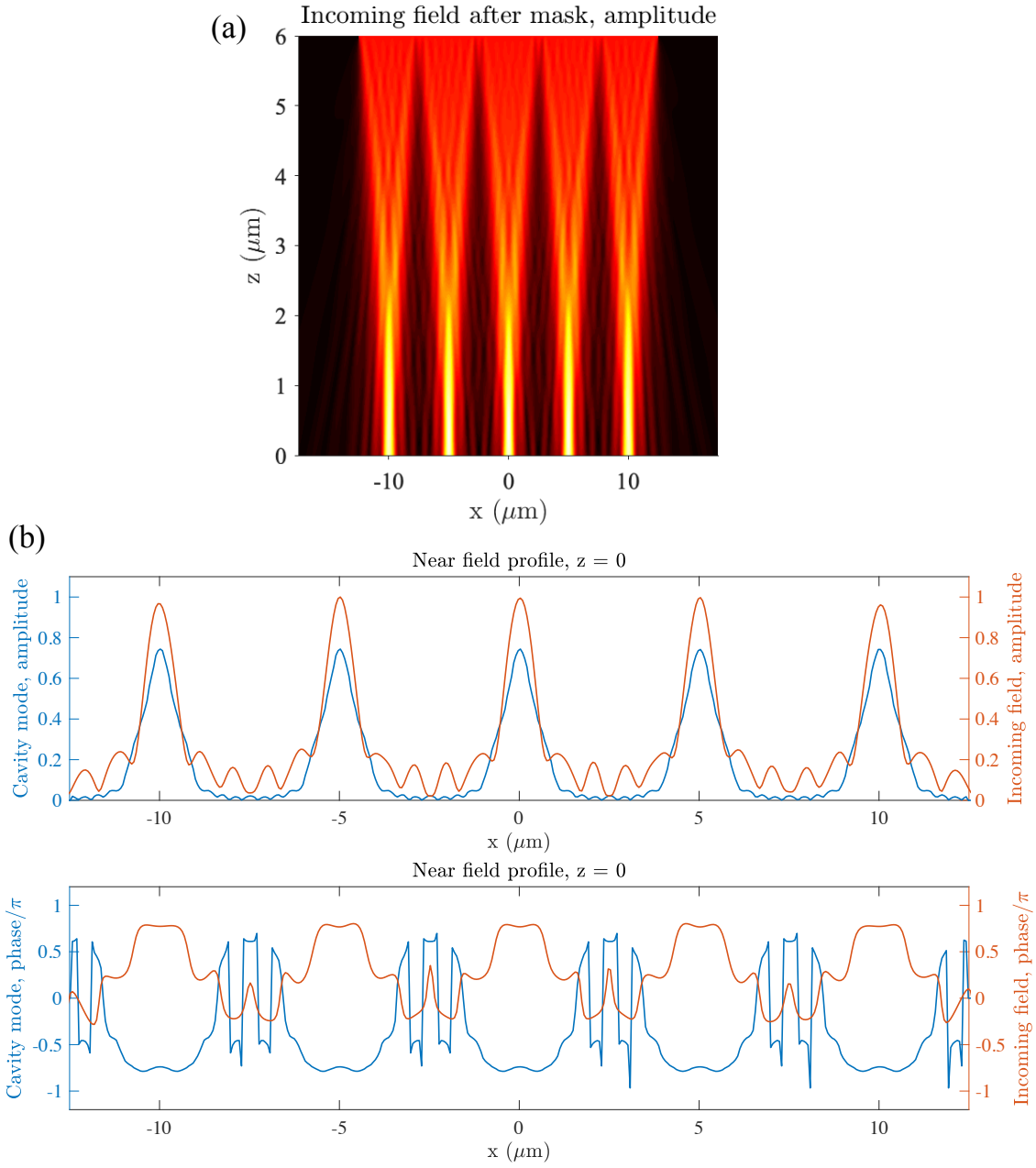

Figure 2-19: In-coupling process of the SLM with a phase correction mask. (a) Propagation of an incoming plane wave after passing through the phase mask. (b) Comparison of the incoming wave's spatial profile with the microcavity's mode profile.

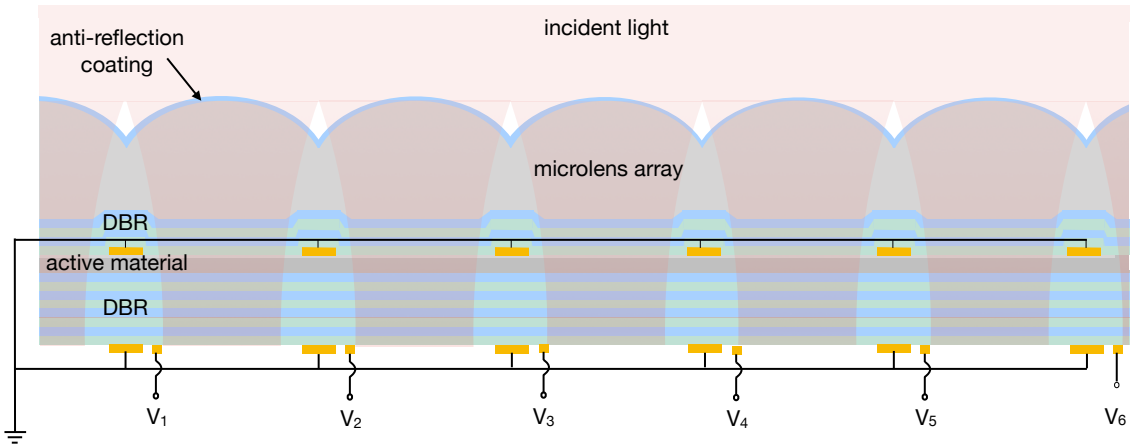

Figure 2-20: Spatial light modulator phase shifter pixels consisting of a planar one-sided vertical microcavity where the lateral optical confinement is provided by a microlens outside the cavity. DBR: distributed Bragg reflector.

limited to a few hundreds. Second, for large-scale two-dimensional arrays of phase shifter pixels where in-plane routing of electrodes is challenging, the signal electrodes are placed at the bottom of the vertical cavity to maintain the continuity of the cavity stack, as illustrated in Fig. 2-20. This results in an attenuated electric field strength in the active material and requires higher operation voltage.

Simulated performance of this design with a $\lambda/2$-thick cavity region is outlined below. The design yields a 10 µm-pitch array of over-coupled optical cavities with a quality factor $Q \approx 330$ and a $V_\pi \approx 40$ V.

The simulated cavity consists of a near-perfect bottom DBR mirror (SiO_2/TiO_2 quarter-wavelength stack), the half-wavelength thick BTO thin film, a partially reflecting top DBR mirror (SiO_2/TiO_2 quarter-wavelength stack), the substrate for the microlens array, the microlens array itself (with spherical surfaces), and an anti-reflection coating above the microlens array. Fig. 2-21 illustrates the target design, with parameters used in the simulation summarized in Table 2.2. The mode profile shown in Fig. 2-21(b) indicates lateral confinement of the cavity mode enabled by the microlens array on top. The near field intensity and phase profiles above the microlens surface, illustrated in Fig. 2-21(a), show that the majority of the emission from the cavity has a nearly uniform phase front. The reflection spectrum of the cavity array

in Fig. 2-21(c) shows that the cavity array is over-coupled with the free-space mode, resulting in a close to unity amplitude reflection response and a 2π phase change across the cavity resonance. The quality factor of the cavity mode is approximately 330.

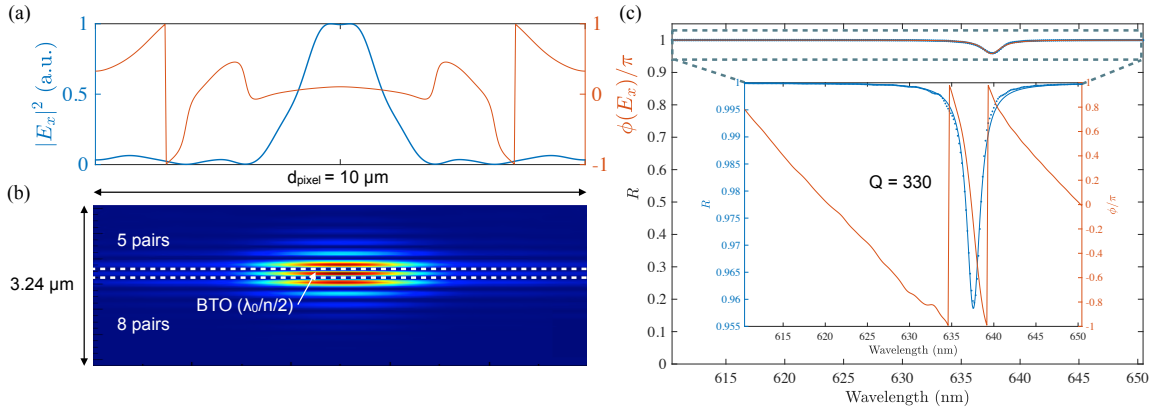

Figure 2-21: FDTD simulations of the target design for the planar reflector-based microcavity array. (a) Near field intensity and phase spatial profile of a pixel. (b) Cross-sectional intensity spatial profile of the cavity mode in a pixel. (c) Reflection amplitude and phase spectrum of the microcavity array.

As the refractive index of the BTO thin film is changed through electrical actuation, the cavity resonance shifts, as illustrated in Fig. 2-22(a). This changes the reflection amplitude and phase at the cavity resonant wavelength $\lambda = 637\,\text{nm}$, which are shown in Fig. 2-22(b). The cavity quality factor of approximately 330 corresponds to a V_π of 40 V.

Parameter	Description	Value
λ_d	Design wavelength	633 nm
n_{SiO_2}	Refractive index of SiO_2	1.457 [47]
n_{TiO_2}	Refractive index of TiO_2	2.3893 [47]
n_{BTO}	Refractive index of BTO	2.289 [32]
r_{eff}	Effective Pockels coefficients of BTO	892.86 pm/V [32]
d	Thickness of the cavity layer	138.3 nm
N_{top}	Number of pairs of DBRs above the cavity layer	5
N_{bottom}	Number of pairs of DBRs below the cavity layer	8
D	Width of the vertical microcavity pillar	10 μm
ROC	Radius of curvature of microlens	15 μm
d_{spacer}	Thickness of the microlens substrate	3 μm

Table 2.2: **Parameters used in FDTD simulation of planar cavity with external microlens.**

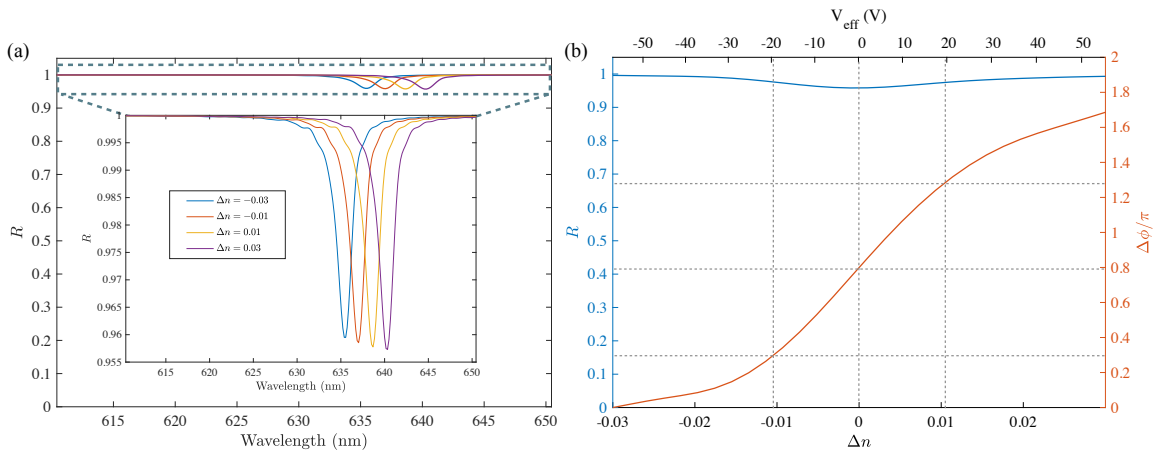

Figure 2-22: FDTD simulations of the target design for the planar reflector-based microcavity array. (a) Reflection amplitude spectra of the microcavity array for different BTO refractive indices. (b) Reflection amplitude and phase at $\lambda = 637\,\text{nm}$ as a function of the refractive index change Δn of BTO and the corresponding effective voltage V_{eff}.

2.4 Design of amplitude SLMs

Amplitude SLMs, as discussed earlier, typically have lower energy efficiency compared to phase-only SLMs due to their amplitude modulation nature. However, in some applications such as amplitude-shift keying (ASK) in data communications, a high-speed two-dimensional array amplitude SLM can be directly applied to increase the data transmission speed and the number of data channels.

This section discusses the design of amplitude SLMs based on tunable vertical microcavity arrays and Pockels effect. Two types of implementation are possible. In the first design, the same design methodology described in Sec. 2.3.1 is used with a design requirement of $R_0 = 0$. This results in a vertical microcavity that is critically coupled to the free space mode and a high on/off resonance extinction ratio at a low voltage. In the second design, the same optimized phase-only modulator is used in combination with some subsequent polarization optics to convert the phase modulation to amplitude modulation.

The critically-coupled microcavity design has the advantage of a higher loaded Q and hence a lower driving voltage. The polarization contrast design has the advantage that a phase-only SLM can be converted to an amplitude SLM without modification

to the phase shifter pixels.

2.4.1 Critically-coupled microcavity amplitude SLMs

In a critically-coupled vertical microcavity, the intrinsic cavity decay rate due to transverse and scattering loss is equal to the rate of coupling between the cavity mode and the incoming free-space mode. In Fig. 2-4, this is represented by the circle that intersects with the origin of the complex plane. As a result, the reflectivity amplitude of the cavity undergoes the most change as the wavelength is detuned from the resonance. This can be used for the design of an amplitude modulator.

In the case of an one-sided cavity, the total decay rate κ_{tot}, which is the sum of the intrinsic loss rate κ_0 and the coupling rate with the incoming free-space mode κ_{e}.

$$\kappa_{\mathrm{tot}} = \kappa_0 + \kappa_{\mathrm{e}} \tag{2.33}$$

For a critically-coupled cavity where $\kappa_0 = \kappa_{\mathrm{e}}$,

$$\kappa_{\mathrm{tot}} = \kappa_0 + \kappa_{\mathrm{e}} = 2\kappa_0, \tag{2.34}$$

while for an over-coupled cavity where where $\kappa_{\mathrm{e}} \gg \kappa_0$,

$$\kappa_{\mathrm{tot}} = \kappa_0 + \kappa_{\mathrm{e}} \gg 2\kappa_0. \tag{2.35}$$

Therefore, for a cavity geometry with the same intrinsic Q, an amplitude modulator based on a critically-coupled cavity can have much larger loaded Q compared to a phase-only modulator based on an over-coupled cavity.

This allows the design of an amplitude SLM where each pixel is a critically-coupled vertical microcavity. Thanks to the high-Q nature of the critically-coupled cavities, this amplitude SLM can have a very high on/off extinction ratio ($> 30\,\mathrm{dB}$) with a CMOS-compatible driving voltage.

The same methodology in Sec. 2.3.1 can be applied to this design, where instead of a design requirement $R_0 \approx 1$, a new design requirement of $R_0 = 0$ is used for realizing

high extinction ratio amplitude modulation. In terms of the numerical bounds of the loaded Q, a lower R_0 leads to a higher Q_max, consistent with the coupling rate picture above.

Fig. 2-23(a) illustrates $Q_{\max}$ and $Q_{\min}$, the upper and lower bounds for the loaded Q, respectively, for various values of reflection on resonance and applied electrical voltages. Fig. 2-23(b) shows the region of acceptable loaded Q with design criteria $R_0 = 0$ and $V_\pi < 0.1\,\mathrm{V}$. Fig. 2-23(c) shows the simulated loaded Q for resonators with various w and N_{top}, overlaid on Fig. 2-23(b). This then indicates that a vertical microcavity with $w = 600\,\mathrm{nm}$ and $N_{\mathrm{top}} = 11$ can get as close as possible to a reflectance on resonance of 0 and a V_π below $0.1\,\mathrm{V}$.

The modulation characteristics of this optimized amplitude modulator design is shown in Fig. 2-24. For a better extinction ratio, transmission mode instead of reflection mode is chosen to avoid degraded extinction due to specular reflection. Fig. 2-24(a) shows the transmission spectrum of the cavity for different refractive index values of the active material $BaTiO_3$, demonstrating the cavity's high quality factor ($Q = 63700$) and index-dependent resonance. Fig. 2-24(b) plots the transmission at a fixed wavelength of 631.275 nm as a function of the refractive index change and the corresponding voltage required to reach the index change, confirming that for this amplitude modulator, a high extinction ratio in excess of 30 dB can be achieved with a CMOS-compatible voltage of less than 1 V.

2.4.2 Polarization contrast amplitude SLMs

The following scheme, illustrated in Fig. 2-25 can be used to convert the phase-only modulators designed in Sec. 2.3.1 and Sec. 2.3.3 to amplitude modulators. Consider light linearly polarized at an angle 45° from y'- and z'-axis is incident on the cavity. When an in-plane E field is applied along the z'-direction, light polarized parallel to the E field and perpendicular to the E field has different Pockels coefficients $r_{z'z'}$ and $r_{y'z'}$. Calculation in Sec. 2.2.1 shows that if $\vec{E}$ is 45° from BTO's <100> axis, $r_{z'z'}$ and $r_{y'z'}$ are both large, and with opposite signs (shown in Fig. 2-26), which creates a phase retardation δ between the two polarizations when the light is reflected back.

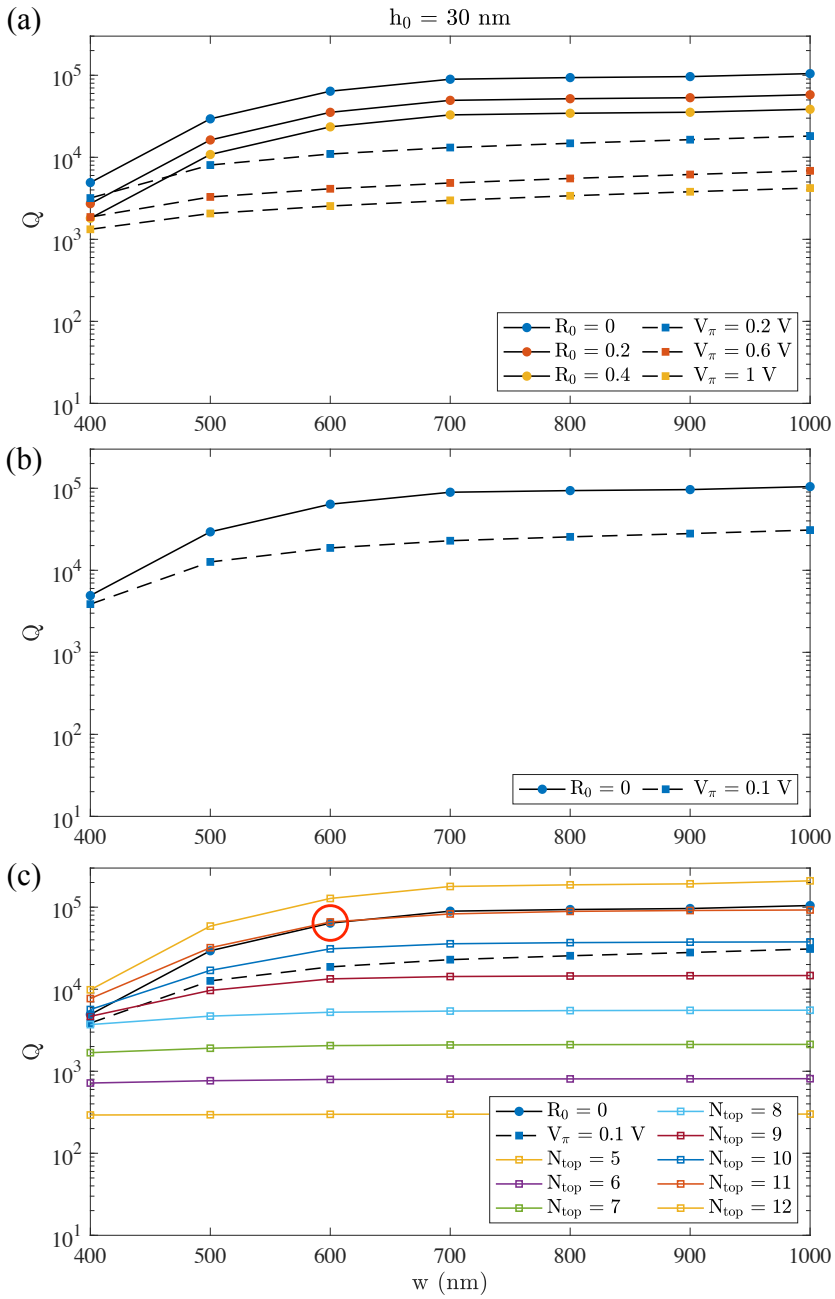

Figure 2-23: Quality factor analysis of the Gaussian-defect vertical cavity. (a) Maximum (solid) and minimum (dash) loaded Q for the reflectance to be greater than certain values and for the voltage required to achieve a π phase shift to be less than certain values. (b) Maximum loaded Q for the cavity to be not under-coupled and minimum loaded Q for the V_π to be less than 0.1 V. (c) Simulation of cavity loaded Q for different defect widths, w, and number of TiO_2/SiO_2 quarter-wavelength pairs in the top DBR, N_{top}. For $w = 600$ nm and $N_{\text{top}} = 11$, the cavity is close to critically-coupled and the voltage for π phase shift is < 0.1 V.

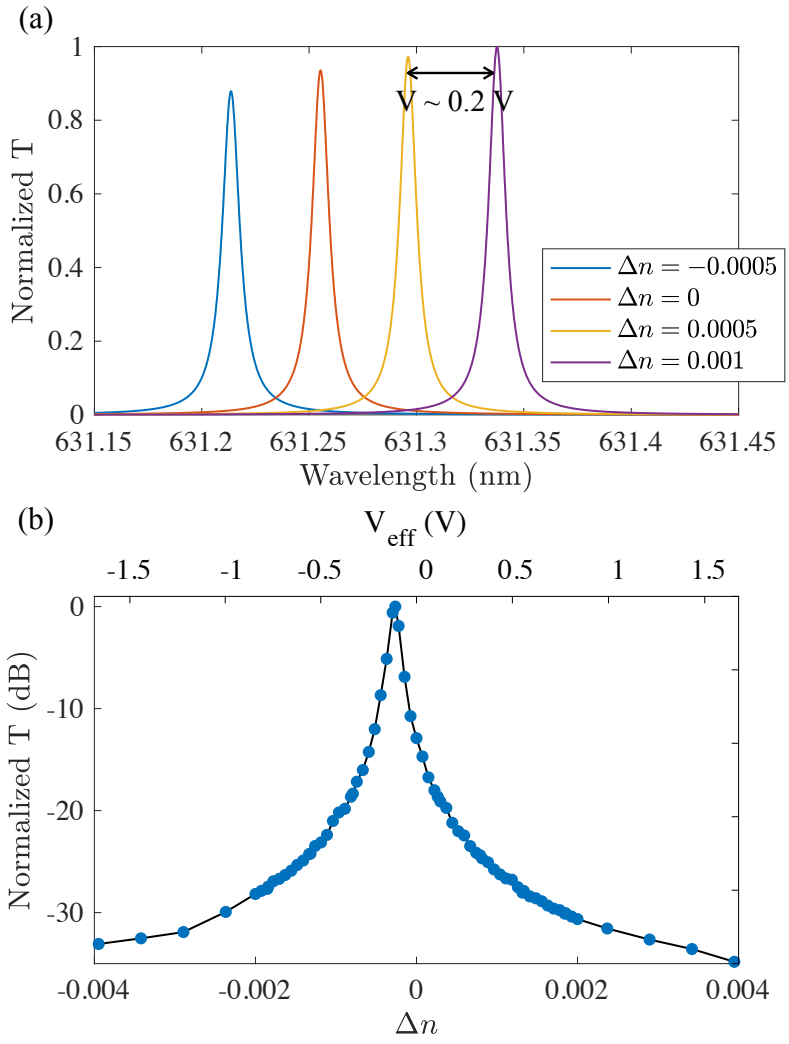

Figure 2-24: Modulation characteristics of the optimized Gaussian-defect vertical microcavity phase shifter element with design parameters $D = 600\,\text{nm}$ and $N_{\text{top}} = 7$.

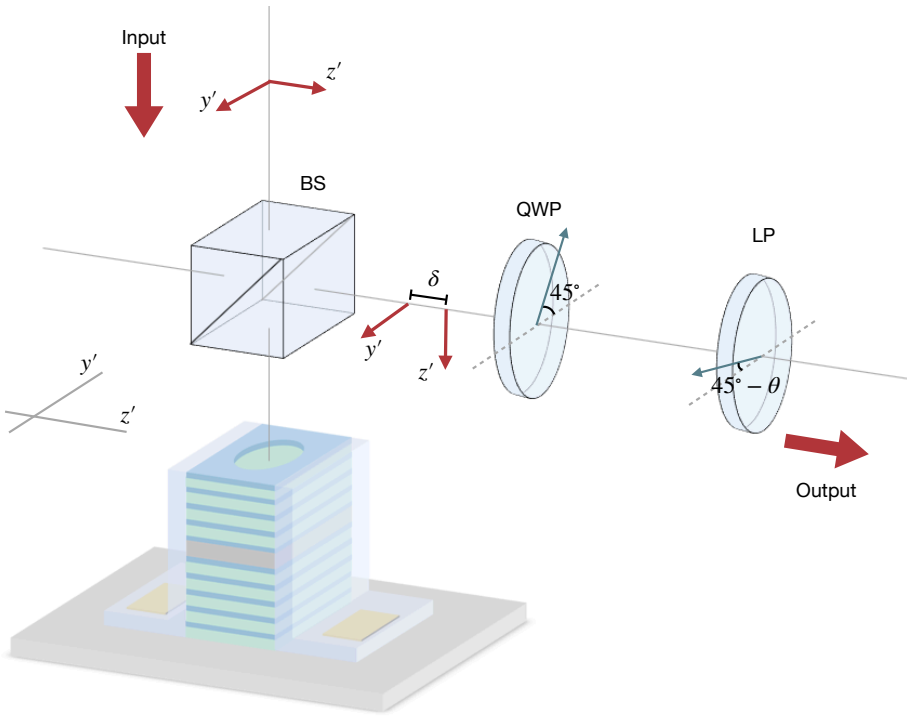

Figure 2-25: Illustration of the polarization contrast scheme that can be used to convert a phase-only modulator to an amplitude modulator. The red arrows represent the polarization of light. The green arrows represent the fast axis of the QWP and the transmission axis of the LP, respectively. BS: Beam splitter. QWP: Quarter-wave plate. LP: Linear polarizer.

This retardation can then be transformed into a modulated amplitude if a quarter-

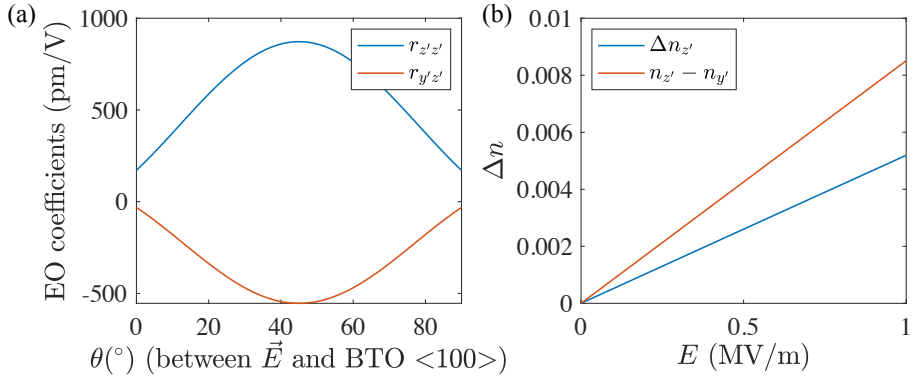

Figure 2-26: (a) The Pockels coefficients of BTO $r_{z'z'}$ and $r_{y'z'}$ as a function of the angle θ between the applied E field and the BTO <100> axis. (b) The refractive index change for light polarized in z' compared to the refractive index difference between light polarized in z' and y', both as a function of the applied electric field strength.

wave plate (QWP) and a linear polarizer (LP) are inserted afterwards.

Mathematically, this process can be described by the Jones matrix formalism as follows. Define $|H\rangle = \begin{pmatrix} 1 \\ 0 \end{pmatrix}$ as light linearly polarized at an angle 45° from y'- and z'-axis. In this coordinate system, the action of the phase-only SLM, the QWP, and the LP can be represented by

$$J_{\text{SLM}} = \frac{1}{2}\begin{pmatrix} 1 & 1 \\ -1 & 1 \end{pmatrix}\begin{pmatrix} e^{-i\frac{\delta}{2}} & 0 \\ 0 & e^{i\frac{\delta}{2}} \end{pmatrix}\begin{pmatrix} 1 & -1 \\ 1 & 1 \end{pmatrix} \tag{2.36}$$

$$J_{\text{QWP-H}} = \begin{pmatrix} 1 & 0 \\ 0 & -1 \end{pmatrix} \tag{2.37}$$

$$J_{\text{LP}} = \begin{pmatrix} \cos\theta & -\sin\theta \\ -\sin\theta & \cos\theta \end{pmatrix}\begin{pmatrix} e^{-i\frac{\delta}{2}} & 0 \\ 0 & e^{i\frac{\delta}{2}} \end{pmatrix}\begin{pmatrix} \cos\theta & \sin\theta \\ -\sin\theta & \cos\theta \end{pmatrix} \tag{2.38}$$

Multiplying the matrices and the input vector together in the proper order, the output vector then becomes

$$|\text{Output}\rangle = \begin{pmatrix} \sin^2\theta\cos\left(\frac{\delta}{2}\right) - \cos\theta\sin\theta\sin\left(\frac{\delta}{2}\right) \\ -\cos\theta\sin\theta\cos\left(\frac{\delta}{2}\right) + \cos^2\theta\sin\left(\frac{\delta}{2}\right) \end{pmatrix} \tag{2.39}$$

The intensity of the output is then

$$I \propto \sin^2(\theta - \frac{\delta}{2}) = \frac{1}{2} - \frac{1}{2}\cos(2\theta - \delta) \tag{2.40}$$

From this, one can see that, by modulating the phase retardation δ through changing the strength of the applied E field, the output intensity can be modulated. The minimum, 0, is achieved when $\delta = 2\theta$, while the maximum, $\frac{1}{2}I_{\text{Input}}$, is achieved when $\delta = 2\theta \pm \frac{\pi}{2}$. The extinction ratio will depend on the phase-tuning range at certain voltage level, the reflectivity amplitude for the two polarizations, and the degree of perfection of the polarization optics.

In the illustration, bulk optics version of the beam splitter (BS), the quarter-wave plate (QWP), and the linear polarizer (LP) are shown. In an integrated SLM system, the BS can be eliminated by aiming the input beam at a small angle from the vertical axis to separate it from the output beam. The QWP and the LP can be replaced by their integrated versions including those based on high-contrast dielectric metasurfaces [51].

2.5 Outlook: Fabrication and CMOS integration of tunable modulator arrays

2.5.1 Process overview

The proposed vertical microcavities can be integrated with the CMOS BEOL process to form two-dimensional arrays and to take advantage of the high-speed large-scale CMOS driving circuitry. Fig. 2-27(a)-(i) outline the steps of this integration process, using the Gaussian-defect vertical microcavity geometry as an example.

A CMOS backplane with high-speed driving electronics is first stripped of its top passivation layer and deposited with a layer of oxide (SiO_2, Al_2O_3, HfO_2) as a bonding layer. A donor wafer consisting of a silicon handle and the active material thin film, which can be obtained from external sources such as companies (for example, NanoLN

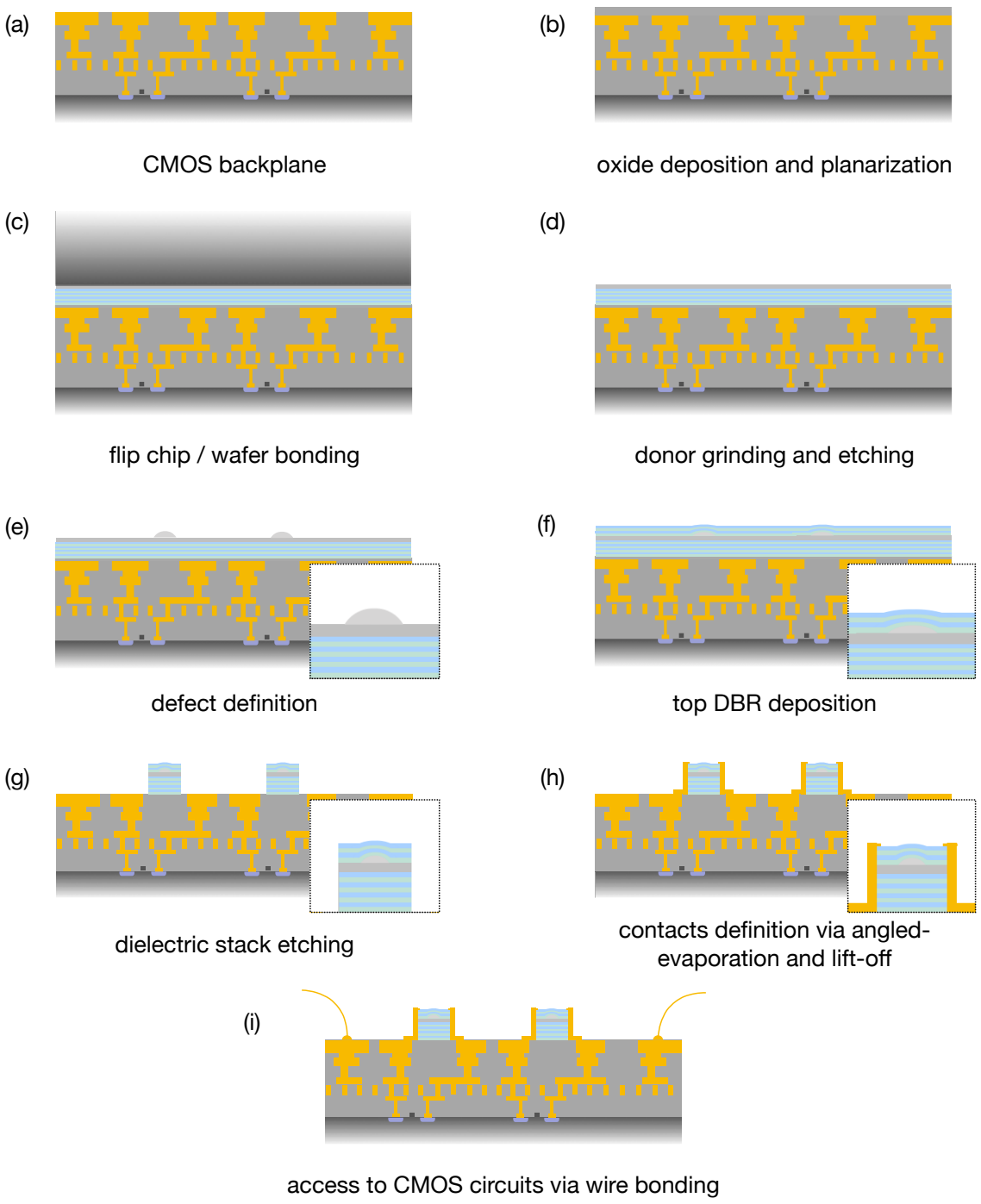

Figure 2-27: Fabrication steps for integration of vertical microcavity arrays with CMOS backplanes. Details can be found in the text.

Jinan Jingzheng Electronics Co. Ltd.) or other research groups, is deposited with a high reflectivity dielectric DBR stack via evaporation or sputtering. A similar layer of bonding oxide is also deposited above the DBR. The donor wafer is then flipped and bonded with the CMOS backplane using fusion bonding, after which the donor wafer's silicon handle is removed by coarse mechanical grinding followed by more controlled etching, exposing the active material thin film.

The active material is then formed into Gaussian-shaped defects. This can be achieved by lithographical patterning of a resist layer above the active material followed by a thermal reflow of the resist and a subsequent etching step to transfer the shape to the active material. A low reflectivity dielectric DBR stack is then deposited above the defects to form the vertical microcavity arrays. To expose the metals on the CMOS backplane, a photolithography process can be used where the patterning resolution exceeds the requirement for pixel size of a few microns. A layer of photoresist is first spun coat on the entire chip and exposed with ultra-violet (UV) light and developed. The whole dielectric stack is then etched using reactive ion etching (RIE) until the top metal layer of the CMOS backplane is exposed, leaving µm-sized mesas with Gaussian-shaped defects at their centers. Another step of photolithography is then used to define contacts that extend from the CMOS top metals to the sides of the dielectric mesas for generating electric fields across the active material. In this step, the photoresist is first patterned, and metal is deposited by two runs of angled-evaporation to conform to the mesa sidewalls, and finally lift-off allows definition of the electrode shape according to the patterned resist. The size of the mesa is several times the size of the optical mode of the Gaussian-defect vertical microcavity. Hence the metal side contacts have enough distance from the mode that there is negligible scattering or absorption loss of the cavity mode due to the reflective and absorptive nature of the metal.

Finally, the CMOS electronics can be accessed and connected to off-chip components (such as a computer) through external electrical wires bonded to the control metal pads in the CMOS top metal layer.

2.5.2 Finished process developments

The external microlens array in the design discussed in Sec. 2.3.5 can be fabricated with the large-scale nanoimprinting method [50, 52] or, for research lab prototypes, with the 3D direct laser writing lithography method aided by two-photon polymerization process. This section discusses the development of a 3D direct laser writing process for microlens array prototyping using the commercially available tool Nanoscribe 3D Lithography System [53].

The 3D structures can be formed basically above any surfaces. To start with, the substrate is cleaned with solvents and baked at 180 °C for 5 to 10 minutes to get rid of condensation. This cleaning step improves the adhesion of resist to substrates. A photoresist IP-dip consisting of monomers is then drop cast onto the surface. A 63× objective is immersed into the resist drop and a pulsed laser with wavelength of $\lambda = 780\,\text{nm}$, pulse duration $\sim 100\,\text{fs}$, and peak power 25 kW is focused onto the interface between the substrate and the resist. Resist exposed with a laser power above the two-photon polymerization threshold will cross-link to form polymers. Subsequent scanning and switching of the focused laser according to a three-dimensional design file then exposes the resist based on a predefined shape. Finally, the sample is developed using the developer PMGEA (propylene glycol monomethyl ether acetate) for 20 minutes and is rinsed in IPA (isopropyl alcohol) for 2 minutes.

Fig. 2-28 demonstrates two microlens arrays written using this process on fused silica substrates.

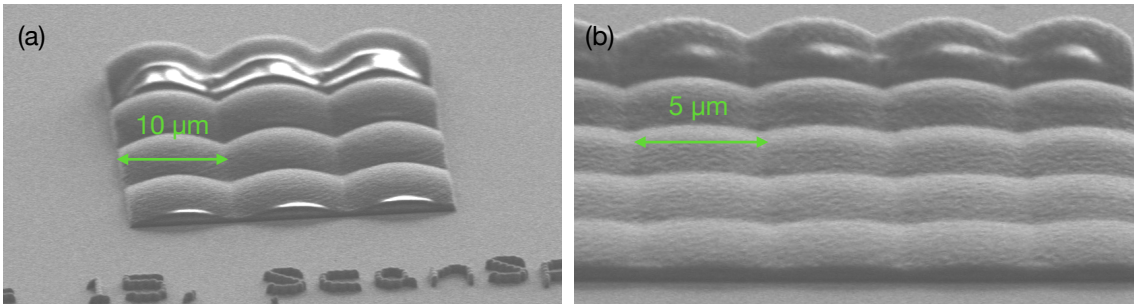

Figure 2-28: Scanning electron micrographs of microlens arrays fabricated with 3D direct laser writing method.

Surface analysis of fabricated microlens

To investigate the effect of surface roughness on the microcavity's reflection spectrum, atomic force microscopy (AFM) is first used to characterize the root-mean-square (RMS) roughness σ and the height-height correlation length L of the surface. The RMS roughness quantifies the degree of surface height variation and the height-height correlation length quantifies the surface features' lateral size. Fig. 2-29(a) shows the surface profile of one microlens and Fig. 2-29(b) fits a cross cut of this surface to a spherical curve. Fitted parameters suggest that the RMS roughness $\sigma \approx 25\,\text{nm}$. The

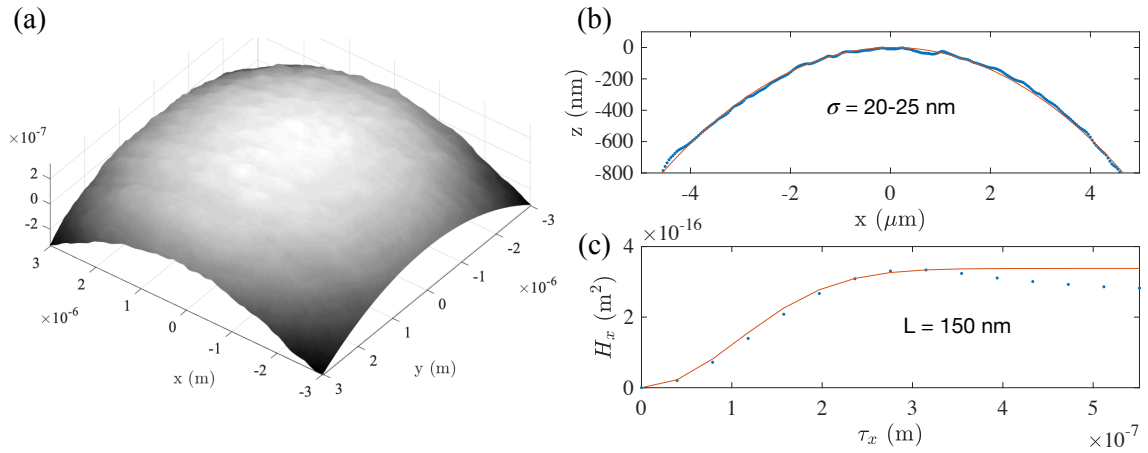

Figure 2-29: Surface analysis of microlens array fabricated with 3D direct laser writing method. (a) Surface profile of a microlens characterized by atomic force microscopy. (b) A cross cut of the AFM surface profile and a fitted spherical curve. (c) Height-height correlation function of the characterized surface.

height-height correlation length L is extracted by fitting the correlation function to a Gaussian curve according to

$$H(\tau_x) = 2\sigma^2\left[1 - exp\left(-\frac{\tau_x^2}{L^2}\right)\right] \tag{2.41}$$

where τ_x is the distance between two points x_1 and x_2. The correlation length is extracted to be $L \approx 150\,\text{nm}$.

The rough surface is then modeled in the FDTD simulation using these two surface parameters to evaluate their effects on the microcavity's spectrum. Fig. 2-30(a) illustrates modeled surfaces with the same RMS roughness and different correlation

lengths. Fig. 2-30(b) shows the simulated reflectivity at off-resonant wavelengths as

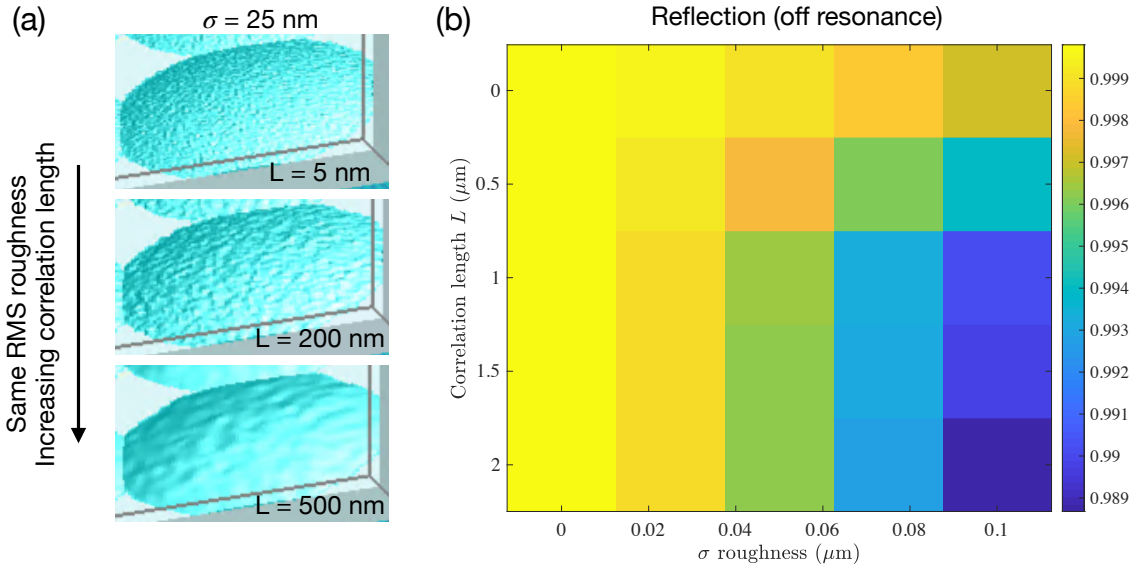

Figure 2-30: FDTD models of rough microlens surfaces and the simulated reflectivity off resonance as a function of RMS roughness σ and height-height correlation length L.

a function of the two surface parameters. Since the microlens array is outside the microcavity and the optical mode is tightly confined between the two DBRs, it is expected that the surface roughness of the microlenses has negligible effects on the overall reflectivity of the microcavities.

Focusing with fabricated microlens arrays

Finally, the focusing ability of the fabricated microlenses can be tested by inputting a plane wave on one side of the microlens array and examining the focused beam profile as a function of the longitudinal distance on the other side of the microlens array.

Fig. 2-31 illustrates the imaged beam profile as the imaging plane moves from below to above the focal plane of the microlens array. Since the microlens arrays are fabricated with different radius of curvatures (ROC) and hence different focal lengths, the imaged beam profiles show focused beams in sequence as the image plane is scanned in the longitudinal distance. As expected, the microlens with the smallest ROC and hence the largest focal length produces a focused beam when the image

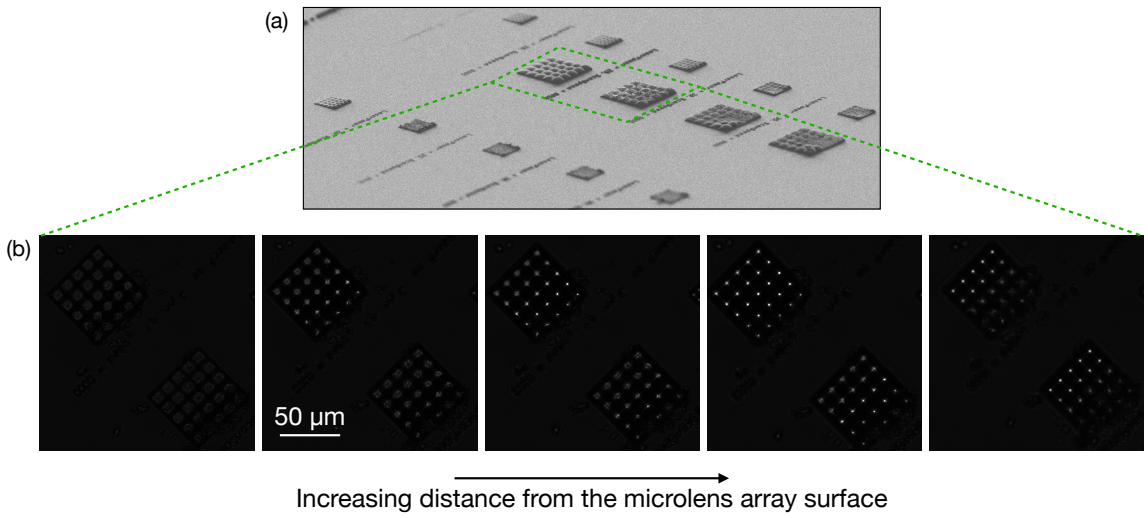

Figure 2-31: Focusing with fabricated microlens arrays. (a) Scanning electron micrographs of microlens arrays fabricated with different pitches and radii-of-curvature (ROC). (b) Imaged beam profiles at several image planes in the longitudinal direction, for a plane wave incident from the back of the microlens arrays.

plane is farthest away from the microlens surface. To quantify the focal lengths, a subsequent experiment can be performed with a piezo-controlled stage to obtain a full 3D stack of beam profile images along with the coordinate information.

Chapter 3

Graphene Surface Nanoscale Electrical Gating Technique

Graphene, a two-dimensional lattice of carbon atoms, possesses electro-optic effects that are consequences of their electrically-tunable electronic band structure. These electrically-induced carrier dynamics have a response time in the picosecond range, promising electro-optic effects with speed in excess of GHz. As a two-dimensional material, graphene is also a natural candidate as a programmable surface. Using an electrical gating approach, graphene surface can be patterned to exhibit a landscape of spatially varying Fermi level, which is critical for the realization of graphene-based metasurfaces and graphene photodetectors.

This chapter introduces this high-speed electro-optic material, graphene, and discusses the development of a technique for generating spatially varying Fermi levels on graphene surfaces at the nanoscale.

3.1 Graphene as an electro-optic material

Graphene has a 2D honeycomb lattice structure with one atom thin thickness ($\sim 3.3\,\text{Å}$). In the reciprocal momentum space, the lattice structure is honeycomb as well. The band structure near the lattice symmetry points K and K' are linear in all

directions with the same slope, forming a conical shape which is called Dirac cone:

$$E_{\pm}(\vec{k}) = \pm v_F|\vec{k}| \tag{3.1}$$

where $\vec{k}$ is the Bloch momentum, $v_F \simeq 10^6$ m/s is the Fermi velocity, and the plus and minus signs denote the conduction band and the valence band, respectively.

3.1.1 Carrier density modulation by electric field effect

Because of graphene's two-dimensional nature, its Fermi level is easily affected by its charge environment. An increase in the electron density will lead to an increase in the Fermi level, and vice versa. The on-demand dynamical change of charge carrier density in graphene is typically achieved via the electric field effect (EFE), where a change in the carrier density Δn is electrostatically induced by an electric field perpendicular to the graphene surface. This technique is effective for low-dimensional materials in general because the Debye screening length λ_D of accumulated charges is typically on the order of 10 nm and can penetrate the whole sample. It is also more flexible compared to another technique commonly used to dope graphene, chemical doping, because it allows *in situ* tuning of graphene's Fermi level which is essential for applications including electro-optic modulation. Doping of graphene without the introduction of additional chemical dopants is also desirable since chemical dopants typically introduce additional disorder that prevents clean study of n-dependent physical properties.

Traditionally electrical gating of graphene and other semiconductor-based field effect transistors (FET) relies on thick ($\sim$ 300 nm) dielectrics such as SiO_2, HfO_2, and Al_2O_3 which are thermally grown or atomic-layer-deposited (ALD) on substrates such as highly doped silicon. A parallel-plate-capacitor model for such dielectrics is shown in Figure 3-1(a). A typical capacitance that can be achieved with this type of dielectrics is $C \sim 10$ nFcm^{-2}, which is limited by the dielectric break-down voltage of material with the given thickness. The highest carrier density induced with these dielectrics is typically on the order of 10^{13} cm^{-2}[54, 55, 56], corresponding to a

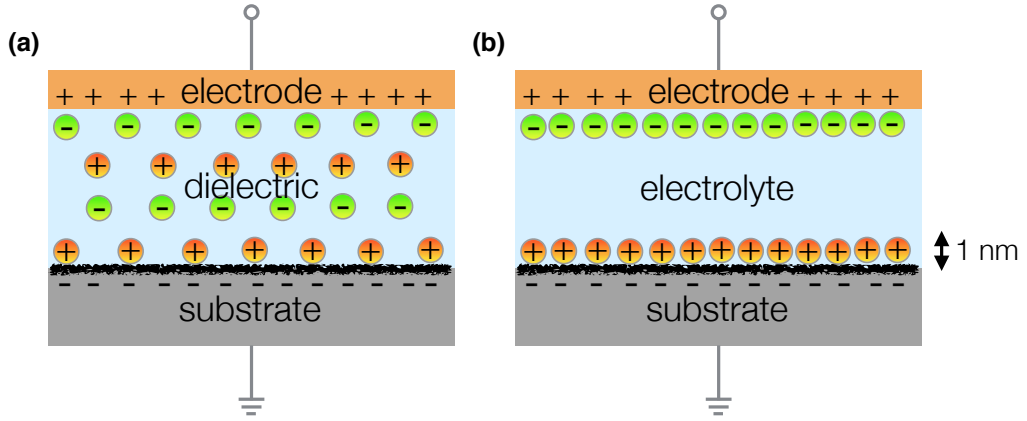

Figure 3-1: Parallel-plate-capacitor models of (a) traditional dielectric (SiO_2, HfO_2, and Al_2O_3) gates, and (b) electrolyte gates. The charges at the interfaces between the sample and the dielectric (electrolyte) schematically represents the Debye screening layer.

graphene Fermi level of $\sim 0.5\,\mathrm{eV}$.

Electrolyte gates are an alternative to the traditional dielectric gates, and come in various types and materials [57, 58, 59]. A parallel-plate-capacitor model for electrolyte gates is shown in Figure 3-1(b). As illustrated in the figure, the main difference between traditional dielectrics and electrolytes is that the Debye layer induced at the interface between the gated material and the electrolyte has a length d of only ~ 1 nm, while the corresponding length for traditional dielectrics is on the order of 10 nm. Therefore the resultant capacitances induced are much higher, reaching a value of $C \sim 5\,\mu\mathrm{F cm}^{-2}$ [60], which is two orders of magnitude higher than that typically achieved in traditional dielectrics. This small Debye length is a result of ionic charges accumulating in direct proximity to the gated material. The capacitance is again limited by the dielectric break-down voltage of the electrolyte material, which is normally accompanied by electrochemical reactions between the electrolyte and the gated sample. The highest reported carrier density induced in graphene with electrolyte gates is on the order of 10^{15} cm^{-2} [60], corresponding to a graphene Fermi level of $\sim 1\,\mathrm{eV}$.

3.1.2 Electrically-tunable optical conductivity of graphene

The electrically-induced change in graphene's Fermi level influences graphene's optical property as well. This can be understood in terms of Drude model for the intraband transition component and in terms of Pauli exclusion principle for the interband transition component. Mathematically, the optical conductivity of graphene can be derived from the Kubo formula within Random Phase Approximation (RPA) [61, 62] and is expressed as

$$\sigma = \sigma_{intra} + \sigma_{inter} \tag{3.2}$$

$$\sigma_{intra} = \frac{ie^2\mu}{\pi\hbar^2(\omega + i\tau^{-1})} \tag{3.3}$$

$$\sigma_{inter} = -\frac{ie^2}{4\hbar}\ln\frac{2|\mu| - (\omega + i\tau^{-1})\hbar}{2|\mu| + (\omega + i\tau^{-1})\hbar} \tag{3.4}$$

where μ is the Fermi level of graphene, τ is the carrier scattering rate, ω is the frequency of light, e is the elementary charge, and $\hbar$ is the reduced Planck constant.

The intraband contribution dominates in the infrared and terahertz range when the graphene is doped and $\mu > \hbar\omega/2$, while for lightly doped graphene ($\mu < \hbar\omega/2$), the interband transition dominates for a wide bandwidth from visible to near-infrared.

Both interband and intraband transitions depend on the Fermi level of graphene, which in turn is related to its carrier density n by $\mu = \hbar v_F\sqrt{\pi n}$ [63]. The electrical tunability of graphene's optical conductivity opens an avenue for using graphene as an electro-optic material.

3.1.3 Photothermoelectric effect in graphene

Electrical gating of graphene can be performed locally to a small region instead of globally on the entire sheet of graphene, which results in a spatial variation of graphene's Fermi level. One phenomenon that can be used to take advantage of this spatial variation and convert incident light to electrical voltages and currents is the photothermoelectric (PTE) effect in graphene.

The mechanism can be understood as follows. The photovoltage generated as a

result of the PTE effect can be written as [64]

$$\mathrm{V_{ph}} = \int S(\mu, x)\frac{dT}{dx}(x)\mathrm{d}x \tag{3.5}$$

where T is the temperature of graphene, S is the Seebeck coefficient, μ is graphene's Fermi level, and x is the spatial coordinate. The Seebeck coefficient in graphene is expressed as [64]

$$S(\mu) = -\frac{\pi^2 k_B^2 T}{3e}\frac{1}{\sigma}\frac{\mathrm{d}\sigma}{\mathrm{d}\mu} \tag{3.6}$$

where σ is the electrical conductivity of graphene, μ is graphene's Fermi level, k_B is the Boltzmann constant, T is the temperature, and e is the elementary charge. For Fermi levels with the same magnitude and the opposite signs, the Seebeck coefficient also has opposite signs.

Suppose light is incident on a uniformly doped graphene. A symmetric temperature profile is generated after light is absorbed. On one side of the junction, the product of the Seebeck coefficient and the temperature gradient produces a photovoltage. On the other side of the junction, the Seebeck coefficient is the same but the temperature gradient is opposite in sign. The integral of the product then produces a photovoltage that cancels out with the previous photovoltage, resulting in zero net voltage and current.

If light is incident on a graphene p-n junction instead. The Seebeck coefficients of the two sides would be opposite in sign and the photovoltages from the two sides would add constructively instead of canceling out. The net effect is then a photovoltage across the p-n junction and corresponding photocurrents.

3.2 Graphene Fermi level spatial variation by electrolyte nanopatterning

Portions of this section have appeared in Reference [65].

Modulation of charge carrier concentration of semiconductors lies at the heart

of many electronic and optoelectronic device operation principles [66, 67]. This modulation is especially essential for two-dimensional (2D) van der Waals materials [68, 61, 69, 70, 71, 72, 73, 74] where the free carrier density change is usually much stronger (2 orders of magnitude) compared to bulk materials and can be dynamically tuned with electrostatic gating methods. In recent years, rapidly developing device concepts and applications impose stronger and stronger requirements on the spatial resolution and highest-achievable carrier concentration of gating techniques. For example, a spatially sharp ($\sim$15 nm) p-n junction and a high carrier density contrast across the junction is the key to the realization of concepts such as tunnel diodes [75] and negative electron refractive index [76]. A strong in-plane electric field across the junction as a result of the junction sharpness facilitates electron-hole pair separation in the photovoltaic (PV) effect [77] and can thus improve the quantum efficiency of PV-based solar cells and photodetectors [78]. Many novel device concepts also rely on the ability to create metamaterials with spatial carrier density variations down to the nanometer scale, including for instance graphene with periodically doped nanodisk or nanoribbon arrays for complete optical absorption in the visible and near-infrared [79, 80], graphene with doped waveguide, bend and resonator patterns for a plasmon-based nanophotonic network [81], and superlattices based on graphene and other 2D materials for concepts such as electron beam supercollimation [82, 83, 84, 85]. Implementing these concepts calls for a gating method that allows for sharp p-n junctions with narrow depletion regions ($\sim$15 nm), a small minimum gating feature size, large carrier density contrasts ($10^{14}\,\mathrm{cm}^{-2}$), strong in-plane electric fields ($> 1 \times 10^{8}\,\mathrm{V\,m}^{-1}$), and the versatility to generate complex spatial doping profiles within a small area.

The state-of-the-art electrostatic gating technique for modulating charge carrier concentration and creating p-n junctions is the metal-dielectric split gate technique [86, 87, 88]. This method is based on the electric field effect [89], described in Sec. 3.1.1, in which electric voltages are applied across a gate dielectric to induce extra charges on the 2D material surface. A p-n junction can be created by applying opposite electric potentials to the two sides of a boundary to induce charges with

opposite polarities. Although this technique is convenient, several limitations restrict its use when more extreme requirements are desirable. In terms of carrier density contrast, dielectric-based gating can only induce a carrier concentration variation Δn of less than $2 \times 10^{13}\,\mathrm{cm}^{-2}$ for typical dielectrics such as SiO_2, HfO_2, SiN, and hexagonal-BN, due to a maximal applicable voltage across the dielectrics before the dielectric breakdown (molecular bond breakage and defects) [54, 55, 56]. In terms of junction sharpness, the carrier density has a slowly varying profile across the junction due to electric field divergence in dielectrics, with a characteristic length similar to the thickness of the dielectric, making it hard to create sharp junctions at nanoscale without using extremely thin (a few nanometers) dielectrics which typically have undesirable leakage and tunneling currents. Furthermore, due to wire-packaging difficulties and fabrication limitation of the electrodes, complex gating patterns and device geometries with large numbers of gating electrodes at the nanoscale is practically challenging.

In this section, I present a nanopatterned electrolytic gating concept that allows for a junction sharpness down to 15 nm and a minimum gating feature size of 30 nm. In contrast to dielectric-based gating, electrolyte gating can concentrate excess charges directly on the surface of the 2D material and reach a capacitance of $C = 3.2\,\mu\mathrm{F\,cm}^{-2}$ (250 times higher than a typical 300 nm SiO_2 gate) [58, 90, 91], which enables carrier density modification up to $\Delta n = 10^{14}\,\mathrm{cm}^{-2}$. Since patterning of electrolyte is challenging, a general method for local electrolyte gates at nanoscale has not been demonstrated so far. To achieve this goal we introduce a lithographic masking technique based on e-beam over-exposed poly(methyl methacrylate) (PMMA) that can screen ions in electrolyte. This e-beam patterned mask can prevent the mask-protected areas from being in contact with, and thus modulated by, the electrolyte gate. Hence this technique effectively creates lithographically-defined local electrolyte gates. Previously, masking of the contacts to create electrolyte gating channels or lateral doping profiles at micrometer scale has been shown with materials such as SU-8 and hydrogen silsesquioxane (HSQ) [92, 93, 94, 95]. However, SU-8 is more commonly used as a photoresist for microstructure patterning. Previous works have demonstrated SU-8 as an e-beam resist for nanometer size patterning, but only for large pitch structures

(∼ hundreds of nm) [96], which makes it unsuitable for creating nanoscale electrolyte gates. HSQ is a high resolution e-beam resist that is capable of creating sub-10 nm patterns. However, no previous studies have been performed on the usage of HSQ as a mask for electrolyte at the nanoscale or investigated HSQ's impenetrability against electrolyte ions. Here I demonstrate patterning of electrolyte gates at the nanoscale. To argue that this technique can create nanometer-sharp junctions and spatial carrier density profiles with feature sizes down to tens of nanometers, I study the junction profile and provide several experimental proofs for the ion-impenetrability of the mask.

3.2.1 Overview of the electrolyte nanopatterning technique

Figure 3-2 illustrates the technique for a graphene sheet. When a voltage is applied between the electrolyte top gate and the graphene, ions in the electrolyte accumulate on the graphene surface, only in regions that are uncovered by the PMMA mask, creating an electrolyte gating pattern defined by the shape of the mask. An additional SiO_2 back gate allows weak p or n doping of the regions covered by the mask.

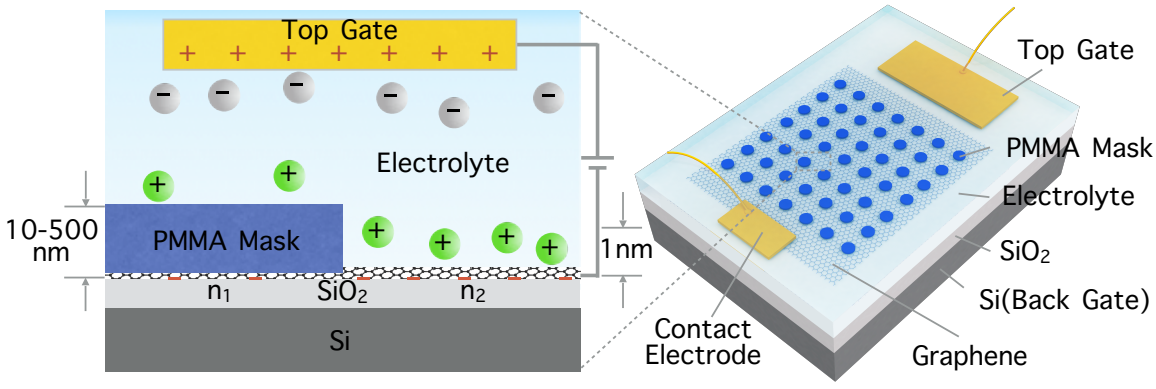

Figure 3-2: Geometry and working principle of nanoscale electrolytic doping of 2D materials with a PMMA screening mask. n_1 and n_2 denote charge carrier densities in the mask-protected region and the exposed region, respectively. The charge carrier density contrast is defined as $\Delta n = |n_1 - n_2|$.

3.2.2 Simulated spatial carrier density profile

For an electrolyte gate voltage of 15 V, a carrier density contrast of $\Delta n \sim 10^{14}\,\mathrm{cm}^{-2}$ can be created at the PMMA mask boundary across only $\sim 15\,\mathrm{nm}$, as shown in the blue curve in Figure 3-3(a), produced by finite element simulations with COMSOL-Multiphysics [97]. Plotted in Figure 3-3(b) in the blue curve is the calculated in-plane

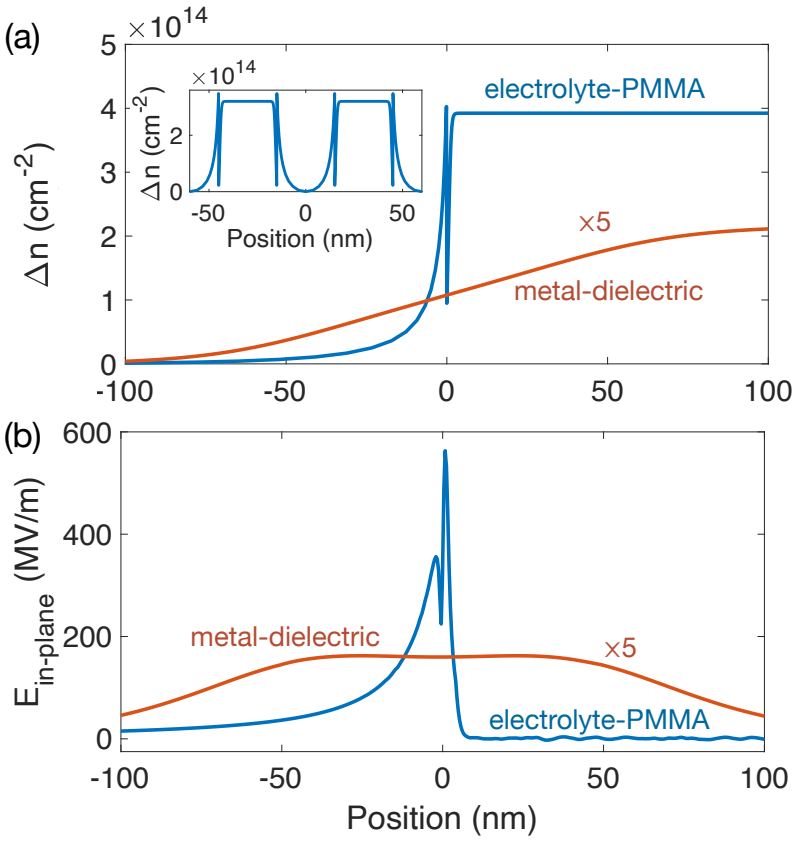

Figure 3-3: Simulated charge carrier density n profile for a single junction, compared between the proposed electrolyte-PMMA-mask gating scheme and a metal-dielectric split gating scheme. Inset: Simulated charge carrier density n profile for the proposed electrolyte-PMMA gating scheme with a periodic PMMA mask with width $l = 30\,\mathrm{nm}$ and thickness $d = 100\,\mathrm{nm}$. (d) Simulated in-plane electric field intensity $\mathrm{E_{in-plane}}$ for a single junction, compared between the proposed electrolyte-PMMA-mask gating scheme and a metal-dielectric split gating scheme. Simulation parameters used in (c) and (d) are summarized below: The gate voltages are $\mathrm{V_{tg}} = 15\,\mathrm{V}$ for the electrolyte-PMMA gating scheme, and $\mathrm{V_{lg}} = -60\,\mathrm{V}$ and $\mathrm{V_{rg}} = 60\,\mathrm{V}$ for the metal-dielectric gating scheme. The dielectric gate has a thickness of 60 nm. The PMMA mask has a thickness of 100 nm. A gap of 100 nm is assumed between the two metal split gates. In the calculation of $E_{\text{in-plane}}$, an additional hexagonal boron nitride capping layer of 1 nm on top of the 2D material is included.

electric field intensity across the junction, showing a maximum magnitude as high as $E_{\mathrm{in-plane}} = 550\,\mathrm{MV\,m^{-1}}$ at the close vicinity of the mask boundary. The simulation assumes a Stern-Gouy-Chapman electrical double layer model [98] of the electrolyte ions and calculates the electric potential and the flux of ions under the influence of both ion diffusion due to the ionic concentration gradient and ion migration due to the electric field. This process is governed by the Poisson-Nernst-Planck equations. The discontinuity in the carrier density profile is caused by the difference in the electric permittivity between electrolyte medium and cross-linked PMMA mask ($\epsilon_{\mathrm{PEO}} = 5$ and $\epsilon_{\mathrm{PMMA}} \sim 20$).

For comparison, the simulated doping contrast and the in-plane electric field are much lower in a metal-dielectric split gate, as indicated in the red curves in Figure 3-3, rescaled for better visibility with a factor of 5. A carrier density contrast of at most $\Delta n = 2 \times 10^{13}\,\mathrm{cm^{-2}}$ (1 order of magnitude lower than that with the electrolyte-PMMA-mask technique) across a length scale of $\sim 100\,\mathrm{nm}$ is induced when a voltage of $\sim 60\,\mathrm{V}$ is applied, corresponding to an in-plane electric field of $E_{\mathrm{in-plane}} = 3 \times 10^{7}\,\mathrm{V\,m^{-1}}$. This simulation assumes a dielectric constant of 3.9 (SiO_2) and a thickness of 60 nm for the gate dielectric, and a gap of 100 nm between the two gate electrodes, which are typical values in the literature[86, 87]. The dielectric thickness and the gap width between the gate electrodes are the limiting factors for the junction sharpness. To achieve a sharpness of $\sim 15\,\mathrm{nm}$, both the dielectric and the gap width have to be similar in size too (see more details below). The former would result in undesirable leaking and tunneling currents and the latter is currently challenging from a fabrication standpoint.

In summary, this nanopatterned electrolyte gating technique can enable sharp junctions at the nanoscale, and carrier density contrast and in-plane electric field orders of magnitude higher than split metal gate structures.

Model for electrolyte ions and finite element simulation

The Stern-Gouy-Chapman electrical double layer (EDL) model [98, 60] is assumed for ions on the surface of objects immersed in an electrolyte. According to the model,

two parallel layers of charged ions are formed on this surface. The first layer, the Stern layer, accounts for the ions' closest approach to the electrode surface and has a thickness on the order of the ionic radius, giving rise to a linear change in the electric potential. The second layer, the Gouy-Chapman diffuse layer, consists of fully solvated ions that can diffuse but are attracted to the Stern layer through Coulomb interaction, resulting in an exponential change in the electric potential. This model only assumes Coulomb interaction between the ions and a constant electric permittivity throughout the electrolyte, neglecting the viscosity of the electrolyte fluid.

In the COMSOL [97] finite element simulation of the electrolyte-PMMA-mask system, ions are assumed to be mobile but confined to the electrolyte diffuse layer region (verified in Section 3 of this Supplementary Information). The relative electric permittivity of the underlying poly(ethylene oxide) (PEO) polymer matrix is assumed to be 5 [99, 100]. When a gate voltage is applied, the charged ions migrate due to the electric field created by the potential difference, and at the same time diffuse as a result of the ionic concentration gradient. This physical process can be modeled by the Nernst-Planck equation:

$$\frac{\partial c}{\partial t} = \nabla\Big[D\nabla c + \frac{Dze}{k_B T} c\nabla\phi\Big] \tag{3.7}$$

where c is the ion concentration, t is time, D is the diffusivity of the ions, z is the valence of the ionic species, e is the elementary charge, k_B is the Boltzmann constant, T is the temperature, and ϕ is the electric potential. The first and second terms correspond to the diffusion and migration processes, respectively. This equation can then be solved in combination with the Poisson's equation that relates the electric potential to the ionic concentration. An additional layer that has the same electric permittivity but forbids diffusion of ions is incorporated in the simulation to represent the Stern surface layer (a thickness of 1 nm is assumed to account for the ionic radius of PEO$-LiClO_4$ [60, 101]), and a region with relative electric permittivity of 20 represents the PMMA mask. Finally, we assume a perfect conducting surface as the boundary condition at the 2D material surface.

The steady-state solution of the coupled equations for the electric potential enables us to deduce the out-of-plane displacement field at the 2D material surface, which in turn allows us to calculate the induced charge carrier density profile on the 2D material. The in-plane electric field in the junction is then given by [102]

$$e|E_{\text{in-plane}}| = 2.5\hbar v_F \alpha^{1/3} (n')^{2/3} \tag{3.8}$$

where $\hbar$ is the reduced Planck constant, v_F is the Fermi velocity in graphene, α is the strength of Coulomb interactions given by $\alpha = e^2/\epsilon_r \hbar v_F$, and n' is the charge carrier density gradient at the p-n interface. Here we note that in the calculation of $E_{\text{in-plane}}$, the geometry of the electrolyte-PMMA-mask system is slightly modified to incorporate a hexagonal boron nitride capping layer of 1 nm on top of the 2D material to keep the carrier density profile a smoothly varying function so that equation (3.8) can be used.

Since the sharpness of the junction which we deduce from the numerical simulation depends on the electric permittivity values used, we study the sharpness dependencies on these parameters for a range of values. Figure 3-4(a) shows the carrier density profiles for different values of ϵ_{PEO} which vary in the literature from 5 to 25 [100, 103, 104]. These curves indicate that a higher value of ϵ_{PEO} would lead to a sharper junction. For a conservative value of $\epsilon_{\text{PEO}} = 5$, which was used in our simulations, the characteristic decay length of the carrier density profile is ~ 15 nm, and for $\epsilon_{\text{PEO}} > 10$, the decay length is < 10 nm. Figure 3-4(b) shows the carrier density profile for different values of ϵ_{PMMA}. The value of ϵ_{PMMA} was determined to be 20 from model fitting in our electrochemical experiments which will be described in Section 3 of the Supplementary Information. Here the figure shows that allowing an error range from 10 to 25, the sharpness of the junction remains below 15 nm. In addition to these two parameters, Figure 3-4(c) shows that the thickness of the PMMA mask, allowing it to vary from 100 nm to 300 nm, does not alter the sharpness of the junction significantly.

In addition, since the model treats the 2D material as a perfect conductor with a constant electrostatic potential, no charge redistribution is considered in this model.

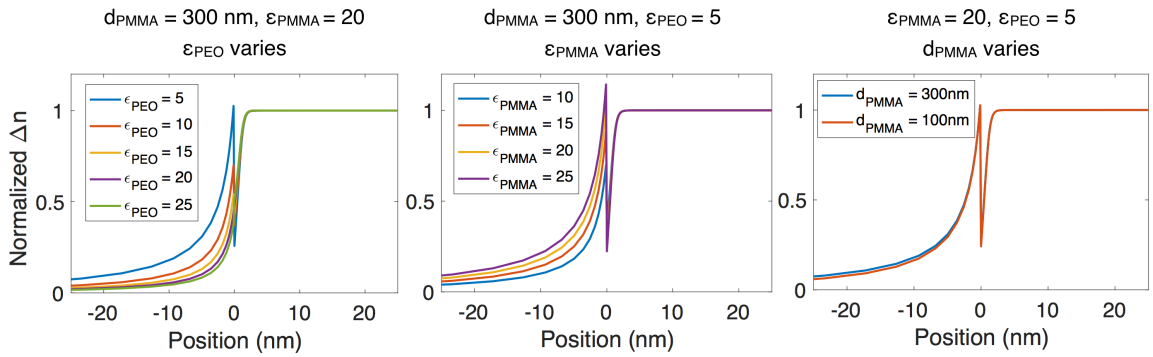

Figure 3-4: Dependence of the sharpness of metal-dielectric split gate junctions on: (a) the gap width between the two split gate electrodes, and (b) the dielectric thickness. Carrier density contrast Δn for each curve is normalized for easier comparison between the profiles. For (a), a constant dielectric thickness of 20 nm is assumed; for (b), a constant gap width of 20 nm is assumed.

In reality, the intense charge carrier density peak on the PMMA side (as seen in Figure 1(c) in the main text and Figure 3-4) will likely subside due to this charge redistribution.

Sharpness limit of metal-dielectric split gate junctions

Two factors limit the sharpness of p-n junctions created by the commonly used metal-dielectric split gate technique: the thickness of the gate dielectric and the gap between the two split gate electrodes. The dependence on the thickness of the dielectric is due to the electric field divergence in dielectric materials. Figure 3-5 illustrates these two dependencies: Figure 3-5(a) shows simulated normalized carrier density profile for metal-dielectric split gate p-n junctions with a constant dielectric thickness of 20 nm and various gap widths; Figure 3-5(b) shows the same profile for junctions with a constant electrode gap width of 20 nm and various dielectric thicknesses.

The curves indicate that when the thickness of the dielectric is larger than the gap width between the electrodes, the sharpness of the junction is limited by the dielectric thickness (Figure 3-5(a)); when thickness of the dielectric is smaller than the gap, the sharpness is limited by the gap width. Thus, to achieve a junction sharpness of a few nanometers, both the dielectric thickness and the gap width have to be only a few nanometers in size too. Unfortunately, the former would result in

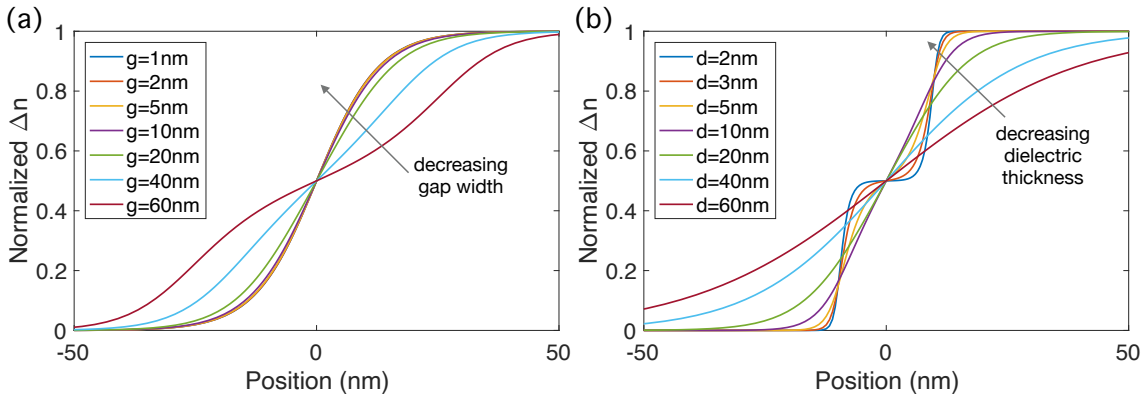

Figure 3-5: Dependence of the sharpness of metal-dielectric split gate junctions on: (a) the gap width between the two split gate electrodes, and (b) the dielectric thickness. Carrier density contrast Δn for each curve is normalized for easier comparison between the profiles. For (a), a constant dielectric thickness of 20 nm is assumed; for (b), a constant gap width of 20 nm is assumed.

undesirable leaking and tunneling currents and the latter is currently challenging from a fabrication standpoint.

3.2.3 Cross-linked PMMA mask: fabrication and validation

To implement this electrolyte gating technique with the screening mask, the choice of material for the mask is essential and several requirements need to be met. To ensure high spatial carrier density modulation resolution, the lithographic resolution of the mask has to be high. To ensure correct junction profile results calculated, the assumptions made in the simulation have to be experimentally verified for the mask of choice, which include the mask's impenetrability to ions in the electrolyte, the straightness of the mask sidewalls, and the ability for the electrolyte to fill, wet and maintain contact with finely patterned nanostructures.

One suitable candidate for the mask is e-beam cross-linked PMMA. In addition to being a high resolution e-beam resist [102, 105], the e-beam cross-linking of this material produces a high carbon atom density material matrix that is nearly impermeable to electrolyte ions. Commonly used as a positive-tone e-beam resist, PMMA becomes negative-tone when exposed at a much higher electron dose ($\sim 20\,000\,\mu C\,cm^{-2}$) which cross-links macromolecules and transforms the resist into higher-density graphitic

nanostructures through a carbonization process [106, 107, 108]. Duan *et al.* [108] have systematically studied the e-beam overexposure cross-linking process of PMMA. When irradiated with electron beams at a normal dose, PMMA in the exposed areas is scissored and decomposed into low-weight molecules and volatile groups (such as CO_2, H_2, CH_3O), resulting in the exposed PMMA being soluble in developers. When the e-beam dose is further increased, the abundant dangling bonds on these low-weight PMMA molecules cross-link to form carbon-carbon covalent bonds, replacing the weaker van der Waals force between the macromolecules in unexposed PMMA and increasing the film density [108]. Since the typical length of such carbon-carbon covalent bonds in organic compounds is 120-154 pm [109], much smaller than the polyethylene-oxide(PEO)-wrapped Li^+ ions ($\sim$ 1 nm) and the ClO_4^- ions ($\sim$ 250 pm) in the electrolyte, the ions cannot penetrate the PMMA mask and reach the 2D material surface. Furthermore, this covalently-bonded structure also enhances the solvent resistance of PMMA, making it insoluble and free from delamination or cracking in common solvents such as acetone, methanol and isopropyl alcohol. Therefore e-beam cross-linked PMMA promises an effective screening mask in our electrolyte/mask selective gating scheme.

Cross-linked PMMA's impermeability to electrolyte ions

To experimentally investigate cross-linked PMMA's impermeability to ions, I first use atomic force microscopy (AFM) to evaluate the morphology of the mask surface and then perform cyclic voltammetry (CV) measurements to examine any potential ion infiltration or ion-induced electrochemical behavior at the surface of mask-protected graphene.

The AFM image of the cross-linked PMMA (Figure 3-6) shows a continuous and smooth surface. Within a 25 um $\times$ 25 um area, the root mean square (RMS) surface roughness is 0.32 nm, indicating a uniform dielectric layer without major defects or pinholes and promising high insulation.

Fig. 3-7 (a) shows the schematic diagrams and an optical micrograph of devices used to investigate the mask impermeability through electrochemical cyclic voltam-

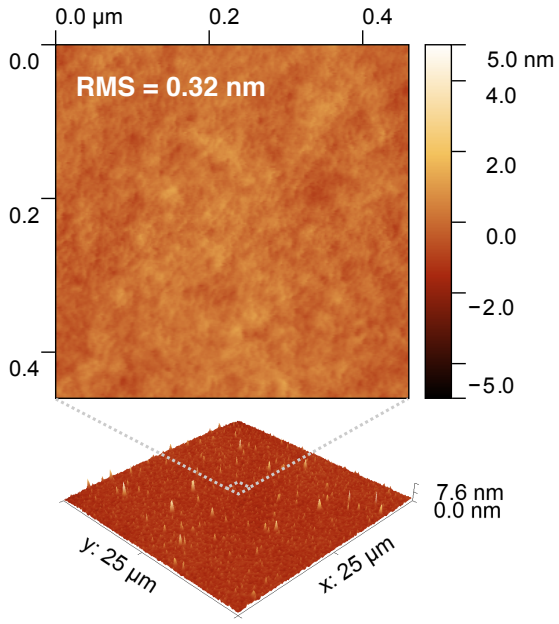

Figure 3-6: Morphology of an e-beam cross-linked PMMA layer, measured by an atomic force microscope. The root-mean-square surface roughness is 0.32 nm.

metry measurements. Five CVD graphene samples are covered with PMMA masks of different thicknesses (250 nm, 80 nm, 40 nm, 35 nm, 10 nm) and solid polymer electrolyte PEO−$LiClO_4$ is then deposited on top of the masked samples. Another sample is exposed directly to the electrolyte. An electrical voltage applied between the gate electrode and the graphene surface follows a sawtooth pattern between −2 V and 2 V at a sweeping rate of 0.5 V/s. Inset of Fig. 3-7 (b) shows the CV curves for different thicknesses of cross-linked PMMA masks from 0 nm to 250 nm. The measured current can be attributed to capacitive charging, electrochemical charge transfer, or charge carrier leakage. The CV curves show that significantly reduced current is observed for the PMMA-mask-protected graphene samples, even for a mask thickness of only 10 nm, qualitatively indicating good impermeability of the mask.

To quantitatively analyze the PMMA impermeability, I calculate from the CV curves the total capacitance C_{tot} of the electrolyte/PMMA mask system as follows:

$$C_{\text{tot}} = \frac{\frac{dQ}{dt}}{\frac{dV}{dt}} = \frac{I}{\frac{dV}{dt}} \tag{3.9}$$

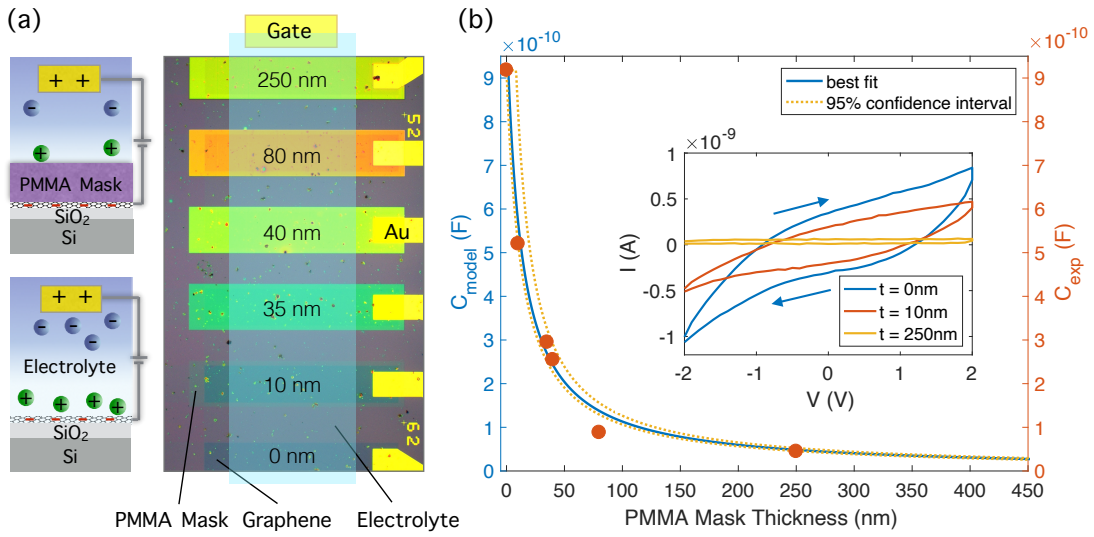

Figure 3-7: Cyclic voltammetry characterization of electrolyte-covered graphene samples protected by PMMA masks of different thicknesses: (a) Measurement schematic diagrams for the cyclic voltammetry (CV) characterization and an optical micrograph of the measured devices. An electrical voltage is applied between the gate electrode and the graphene surface and ramped linearly with time from $-2\,\mathrm{V}$ to $2\,\mathrm{V}$ back and forth at a rate of $0.5\,\mathrm{V/s}$ for a few times. (b) Capacitance of the PMMA-mask/electrolyte system extracted from the CV measurements (red dots) and fitted to a simple model (blue curve) as a function of the mask thickness. The area between the two yellow dotted lines indicates the 95% confidence interval of the fitting. Inset: Measured CV curves for samples with different PMMA mask thicknesses. The arrows indicate the voltage sweeping directions.

where Q is the charge accumulated on the capacitor, I is the measured current, and dV/dt is the voltage sweeping rate. Figure 2(b) in main text plots the instantaneous capacitances (red dots) of the system calculated from currents at $V = 0.2\,\mathrm{V}$ for different mask thicknesses. We model the total electrolyte/PMMA mask system as an electrolyte capacitor in series with a PMMA mask capacitor, with the total capacitance C_{tot} given by

$$\frac{1}{C_{\mathrm{tot}}} = \frac{1}{C_{\mathrm{elec}}} + \max\left(\frac{d - d_0}{\epsilon_{\mathrm{r}}\epsilon_0 A}, 0\right) \tag{3.10}$$

Here the electrolyte has a capacitance of C_{elec}, which can be calculated from the CV curve for the mask-uncovered graphene sample. The PMMA mask is modeled as a parallel plate capacitor with plate area A, dielectric constant ϵ_{r}, original thickness d

and a conjectured ion infiltration layer of thickness d_0 (defined by a layer of PMMA mask that is penetrated and filled by diffused electrolyte ions). Taking the dielectric constant ϵ_r of the PMMA mask and the ion infiltration layer thickness d_0 as fitting parameters, the total capacitance calculated from the CV measurements are fitted to this model. The data points and the model (blue line in Fig. 3-7(b)) show good agreement. The conjectured ion infiltration layer is extracted to be 1.5 nm in thickness, with a standard error of 3.4 nm. The dielectric constant of the PMMA mask is extracted to be 20 (with a 95% confidence interval of $(19, 21)$), in rough agreement with previous experiments [92] where e-beam cross-linked PMMA was used as a gate dielectric. The slight deviation of the experimental data from the model can be accounted for by the nonuniform capacitor plate area in the experiments as a result of the manual drop casting of electrolyte on the graphene samples. This quantitative analysis provides further evidence that the mask provides reliable protection against the ions in the electrolyte, with an estimated ion infiltration layer of thickness 1.5 ± 3.4 nm into the PMMA mask.

Electrolyte wetting of cross-linked PMMA nanostructures

To implement the electrolyte-PMMA-mask gating technique, the electrolyte must be able to fill, wet and maintain contact with finely patterned cross-linked PMMA nanostructures. Due to the balance between adhesive and cohesive forces between a liquid and solid, a liquid drop might have the tendency to avoid contact with the solid surface, which is undesirable in the case of this gating technique.

To verify electrolyte's wetting of the PMMA nanostructures, cross-sectional scanning electron microscopy (SEM) is used to verify the electrolyte wetting. Cross-linked PMMA is patterned into nanowires and electrolyte is deposited on top of the nanostructures. Cleaving of the sample exposes the cross section of the nanowires and the electrolyte. Fig. 3-8 shows the SEM images of these cross sections, where from the homogeneous color of the electrolyte region we confirm the electrolyte's ability to fill narrow slits and remain in contact with the 2D materials. The slits between the PMMA nanowires in Fig. 3-8(b) is roughly 20 nm, so it can be concluded that the

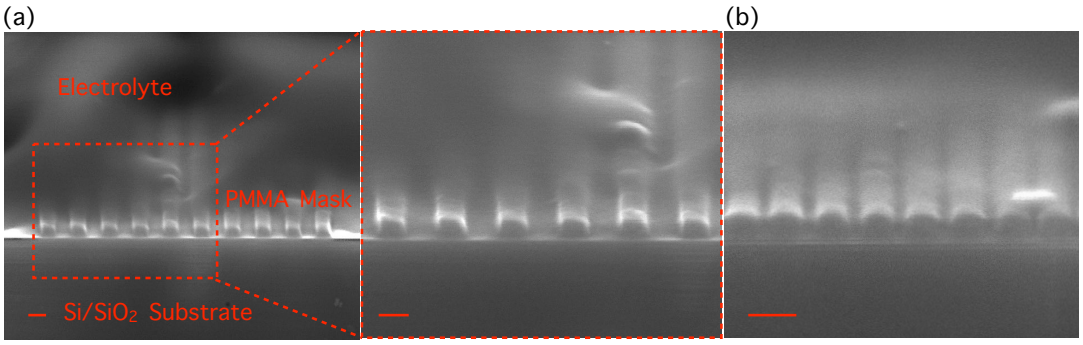

Figure 3-8: Scanning electron micrographs (SEMs) of cross section of PMMA nanostructures on a Si/SiO2 substrate covered by solid polymer electrolyte PEO/LiClO4. Scale bar: 100 nm.

electrolyte is able to wet narrow slits of at least 20 nm and remain good contact with finely patterned nanostructures.

Cross-linked PMMA's spatial patterning resolution

The spatial carrier density modulation resolution of the local electrolytic gates is determined by two factors: the e-beam lithography resolution of the screening mask and the sharpness of the junction. As shown in the simulation, the junction sharpness is ~ 15 nm, and the e-beam resolution has previously been demonstrated to be sub-10 nm[106], so the spatial modulation resolution using this technique is limited by roughly twice the junction sharpness, which is 30 nm. The simulation in the inset of Fig. 3-3(a) indicates a well-defined carrier density modulation profile resulting from periodic local electrolyte gates with a half-pitch of 30 nm.

Fig. 3-9 shows SEM images of examples of PMMA masks on graphene with this resolution and different geometries, including disks and ribbons. The cross section of the resist mask ribbons indicates straight sidewalls.

3.2.4 Proof-of-principle experiments: graphene *p-n* junctions

As proof-of-principle studies, this technique is used to demonstrate the dynamical tuning of a graphene *p-n* junction. The device, shown in Fig. 3-10(a) (top panel), consists of a graphene channel covered in half by a PMMA mask. The graphene is

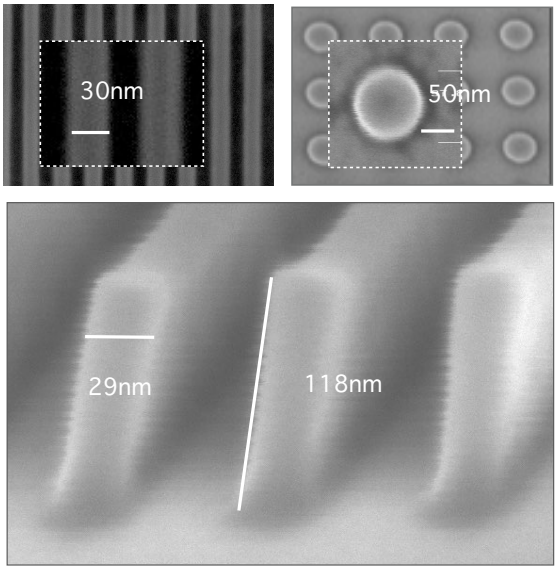

Figure 3-9: Scanning electron micrographs (SEMs) of example fabricated PMMA masks with nanoscale dimensions.

exfoliated onto a 285 nm SiO_2 substrate thermally grown on doped Si. It is then patterned by e-beam lithography and reactive ion etching (RIE) into a channel roughly 10 µm in length and 5 µm in width. A pair of Cr/Au contacts and a PMMA mask are then defined by e-beam lithography. Solid polymer electrolyte PEO$-LiClO_4$ is then drop-casted to cover the entire device.

Large-range doping level control of the two regions in a *p*-*n* junction can be achieved by tuning electrolyte top gate and SiO_2 back gate voltages, where V_{tg} controls the mask-uncovered region and V_{bg} mostly controls the mask-covered region. Fig. 3-10(c) shows the channel resistance R versus V_{tg} and V_{bg}, showing four distinct characteristic regions that indicate gate-voltage-tunable charge density at a *p*-*n* interface [110]. Two intersecting lines of high resistance (white dashed), representing charge neutrality points of the two regions respectively, divide the resistance map into four low-resistance regions: *p*-*n*, *p*-*p*, *n*-*p*, and *n*-*n*. A vertical line trace of the 2D resistance map along the dotted gray line, shown in the blue curve of Fig. 3-10(b), exhibits a distinct Dirac peak indicating modulation of graphene's Fermi level across the charge neutrality point.

Photoresponse observed at the graphene *p*-*n* junction can also be dynamically

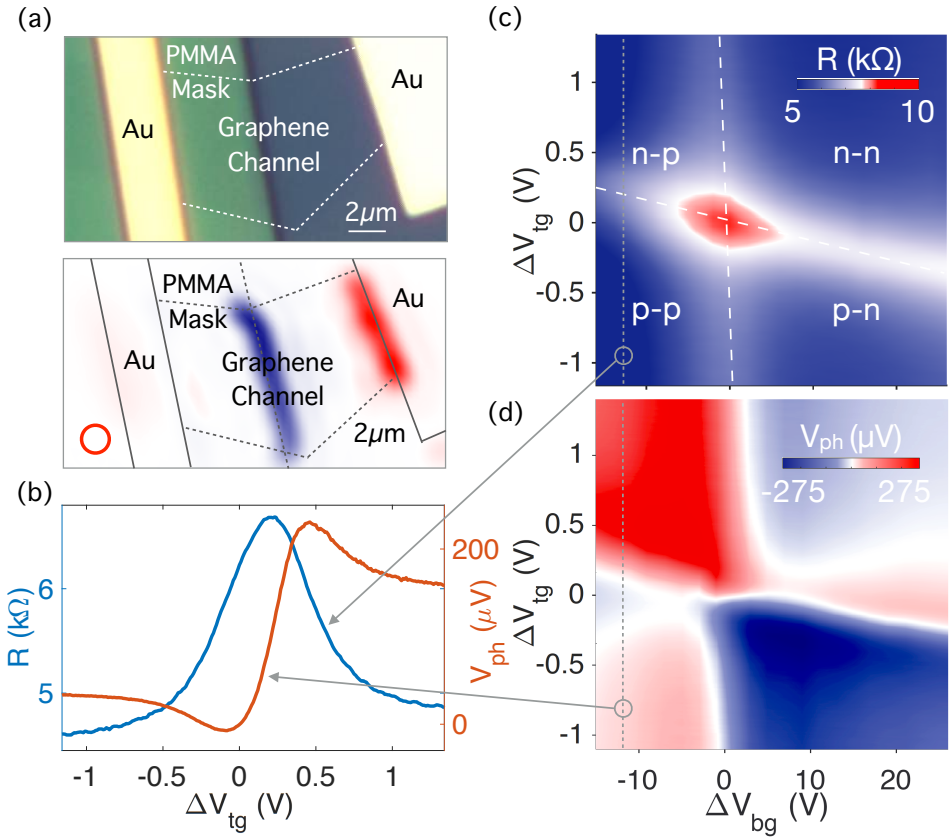

Figure 3-10: Gate-tunable graphene p-n junction and its photoresponse. (a) Top: Optical image of the graphene p-n junction device before covering with the electrolyte. Half of the graphene channel is covered by a PMMA mask. Bottom: Photovoltage V_{ph} spatial mapping of the p-n junction device conducted on a near-infrared ($\lambda = 1.55\,\mu m$) confocal scanning microscopy setup. The red circle indicates the FWHM of the laser spot ($\sim 1.7\,\mu m$). (b) Resistance R and photovoltage V_{ph} as a function of V_{tg}, measured at $\Delta V_{bg} = -12\,V$ (line traces for (c) and (d) along the gray dotted line). (c) Resistance R as a function of V_{tg} and V_{bg}. White dashed lines indicate charge neutrality points of the top- and bottom-gated halves of the channel, and the four regions correspond to four doping configurations of the channel. (d) Photovoltage V_{ph} as a function of V_{tg} and V_{bg}, measured at the p-n interface.

tuned by the gate voltages. Figure 3-10(a) (bottom panel) shows the spatially-resolved open-circuit photovoltage map of the device under zero bias voltage across the channel, conducted on a near-infrared ($\lambda = 1.55\,\mu m$) confocal scanning microscopy setup at room temperature. As the laser excitation is scanned over the device, a large photovoltage V_{ph} is observed at the electrolyte gate defined junction. This photovoltage V_{ph} at the junction as a function of V_{tg} and V_{bg}, plotted in Fig. 3-10(d), exhibits a distinct six-fold pattern with alternating photovoltage signs, showing a strong dependence of the photoresponse on the relative doping level of the graphene junction. This six-fold pattern indicates a photo-induced hot carrier-assisted photoresponse process at the graphene *p-n* junction known as the photo-thermoelectric (PTE) effect [64], discussed in detail in Sec. 3.1.3. A vertical line trace of the 2D photovoltage map along the same dotted gray line, plotted in the red curve of Fig. 3-10(b), shows typical non-monotonic gate voltage dependence as a result of the PTE effect.

3.3 Outlook

The nanoscale electrical gating technique developed in this chapter allows dynamical programming the surface of graphene and other 2D materials. This paves the way for the demonstration of numerous photonic device concepts. One example of a compact graphene thermopile in the mid-infrared is discussed in Sec. 4.1, where a carefully designed Fermi level spatial profile geometry is realized with this gating technique to enhance the photovoltage responsivity. The extreme localization of Fermi level variation also promises to enable the creation of graphene plasmonic nanoresonators with high quality factors. They are building blocks of voltage-tunable graphene metasurfaces.

To further validate this technique, experiments in two directions can be performed. First, by repeating the cyclic voltammetry measurements and the capacitance modeling several times, with an interval of days or weeks, it would be helpful to investigate the diffusion of ions and the penetration depth in the PMMA masks at longer time scales. Second, by designing and fabricating devices with nanoscale Fermi level vari-

ation building blocks (for example, plasmonic nanoresonators), it would be possible to obtain direct experimental proofs of nanoscale gating.

Furthermore, the solid polymer electrolyte PEO/$LiClO_4$ and the cross-linked PMMA mask used here show promising results. However, PEO/$LiClO_4$ electrolyte shows absorption peaks in the mid-infrared wavelengths which could present obstacles for spectroscopy, electro-optic modulation, or photodetection. A complete survey of solid polymer electrolyte ionic types and organic matrix materials would allow optimized choice for wavelengths of interest. Other than cross-linked PMMA, it would be helpful to experiment with other e-beam resists to further improve the spatial patterning resolution.

Chapter 4

Electrically-Modulated Graphene for Photonic Devices

This chapter demonstrates several photonic device concepts based on electrically-modulated graphene. To begin with, a compact graphene thermopile that takes advantage of the spatial Fermi level modulation technique developed in Sec. 3.2 is optimized and demonstrated for the thermal detection of mid-infrared light. Two high-speed photonic devices, including a photodetector and an electro-optic modulator, for the near-infrared are then introduced. Finally, a graphene-insulator-metal heterostructure is used to probe the ultimate limits of plasmon confinement down to the length scale of one atom, enabling new regimes for ultrastrong light-matter interactions.

4.1 Compact graphene thermopile in mid-IR

Portions of this section have appeared in Reference [65].

This section discusses the design and demonstration of a compact mid-infrared graphene thermopile, leveraging the spatial gating versatility of the technique developed in Sec. 3.2 and the PTE effect in graphene. The thermopile has 8 thermocouples connected in series and arranged in a geometry that optimizes voltage collection for free-space incident radiation with a Gaussian profile. The geometry flexibility of the

patterned electrolyte gating technique eases the fabrication process and results in a small device footprint that is comparable to the diffraction limited beam size of mid-infrared light.

In this design a complex doping pattern of graphene is created to enhance the thermopile's photovoltage responsivity. As discussed in Sec. 3.1.3, for PTE effect, the photovoltage generated can be expressed as $V_{ph} = \int S(n,x)\Delta T(x)\mathrm{d}x$, where S is the Seebeck coefficient of graphene, a function of charge carrier density, and ΔT is the increase in electron temperature from the environment. For free-space incident light that has a spherical Gaussian profile, the temperature gradient points in the radial direction, so the photovoltage is maximized when it is collected radially.

The designed thermopile geometry, whose equivalent circuit diagram is illustrated in Fig. 4-1, consists of several thermocouples connected in series whose photovoltages are all collected in the radial direction. Each graphene segment is considered a voltage source with a resistance. For the photovoltage to sum up along the meandering graphene channel, each segment is $p-$ or $n-$doped in an alternating fashion so that neighboring photovoltages point in opposite directions (Seebeck coefficient has opposite signs). The alternating doping is achieved using our gating technique by covering every other segments with the PMMA mask and applying positive V_{tg} and negative V_{bg} respectively. Compared to existing graphene thermopiles such as that in ref. [111], this approach eliminates the need for embedded gates and external wiring of thermocouples, enabling a compact thermopile based solely on graphene.

4.1.1 Experimental demonstration of thermopile in mid-IR

Spatially-resolved open-circuit photovoltage mapping of this thermopile is conducted on a confocal scanning microscopy setup with a mid-infrared laser source at two wavelengths $\lambda = 8.58\,\mu\mathrm{m}$ and $\lambda = 7.15\,\mu\mathrm{m}$. The photovoltage between several sets of terminals (indicated with numbers in Fig. 4-1) are measured to study the individual contributions of thermocouples. As the laser spot is scanned over the device, a maximal photovoltage V_{ph} is observed at the center of the thermopile, as shown in the photovoltage spatial maps in the inset of Fig. 4-2. The spatial maximum for respon-

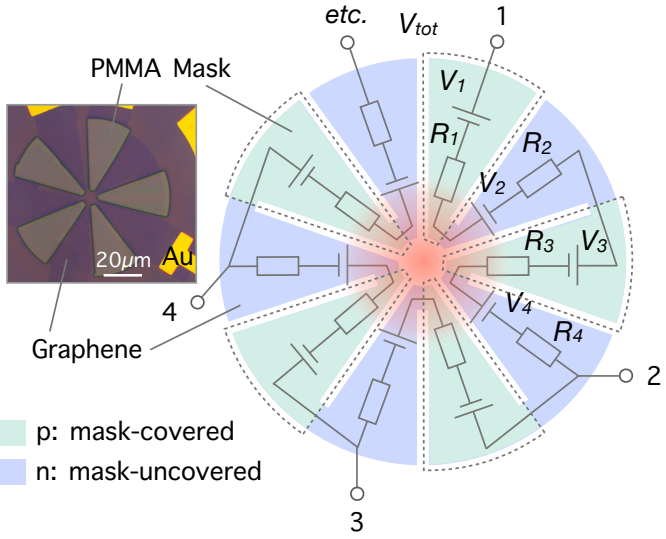

Figure 4-1: Equivalent circuit diagram and optical image of the compact graphene thermopile design. Graphene is etched into a circular channel with a meandering shape, with each segment acting as a voltage source and a serial resistance. The segments are *p*- or *n*-doped in an alternating way to produce photovoltage in the same direction along the channel. The doping pattern is generated by covering every other graphene segments with a PMMA mask and applying appropriate V_{tg} and V_{bg}.

sivity is then plotted as a function of the number of voltage source segments between the terminals. The well-fitted linear relation at both wavelengths confirms the summation of photovoltages from each individual segment. The maximal responsivity of this device is $26.2\,\mathrm{mV\,W^{-1}}$ at $\lambda = 8.58\,\mu\mathrm{m}$, when 8 voltage segments are included in the device. Compared to a previous graphene thermocouple with only one single *p*-*n* junction, studied in similar conditions [112], the carefully designed doping pattern of graphene results in an about 7 times enhancement in photovoltage responsivity. Further optimization of parameters including device dimension and the number of voltage segments can be done to achieve higher responsivity (see Supplementary Information for a detailed discussion), and the device can be suspended as in ref [111] to benefit from higher temperature gradient as well.

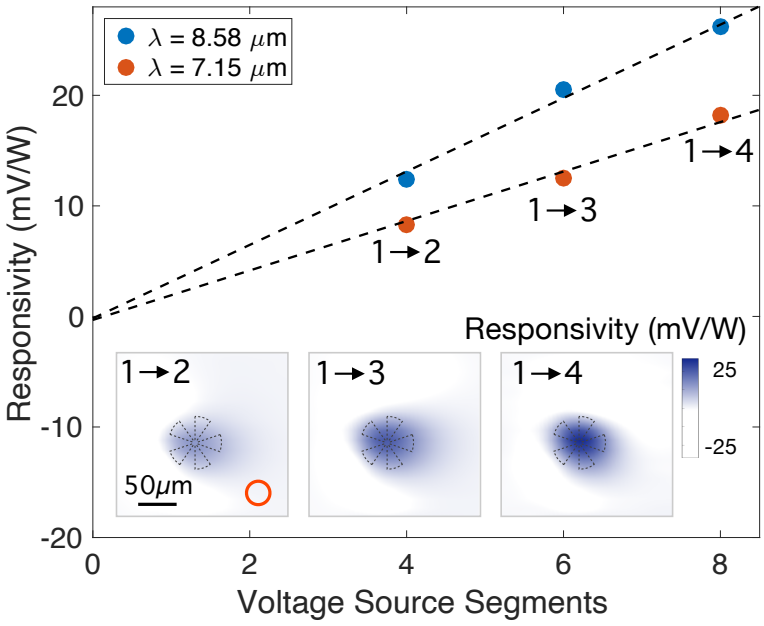

Figure 4-2: Photovoltage responsivity of the thermopile measured at the center of the device as a function of the number of voltage source segments included in the circuit at $\lambda = 8.58\,\mu\text{m}$ and $\lambda = 7.15\,\mu\text{m}$. Data points are fitted with a linear curve indicated by the dashed line. Inset: Photovoltage responsivity spatial mappings of the thermopile measured at $\lambda = 8.58\,\mu\text{m}$, with 4, 6 and 8 voltage source segments included in the circuit, respectively. The dashed circles indicate the size of the thermopile device. The red circle indicates the FWHM of the laser spot ($\sim 30\,\mu\text{m}$).

4.1.2 Thermoelectric simulation and optimization

The geometry of the presented mid-infrared compact graphene thermopile is designed such that the photovoltage can be most efficiently collected for free-space incident radiation with a circularly symmetric Gaussian profile. This section discusses different design parameters that can influence the photovoltage responsivity V_{ph} and the noise equivalent power (NEP) of the thermopile.

In the thermoelectric simulation, the following assumptions are made. First, for graphene on a substrate that is absorptive for the mid-infrared light, the heating of electrons in graphene is dominated by the optical absorption and thermal conduction of the substrate and hence the electron temperature follows that of the substrate temperature [112]. The substrate temperature is in turn determined by the power and the FWHM of the incident laser spot. Second, the Seebeck coefficient of graphene can be tuned to its respective maximum values on both the $n-$doped and $p-$doped segments of the graphene channel and that the doping transition follows a step function. This is a valid assumption since the device scale in this mid-infrared thermopile is much larger compared to the junction transition length of 15 nm which is shown in the main text. We then conclude that the generated photovoltage depends entirely on the geometry of the device given a fixed incident laser spot. With proper selection of design parameters, one can then optimize the geometry of the thermopile to achieve better performance metrics such as photovoltage responsivity and noise equivalent power.

For the proposed thermopile, the geometry is mostly dictated by four parameters: (1) the outer radius, (2) the inner radius, (3) the connecting bridge width, and (4) the number of voltage source segments in a full circle, as illustrated in Figure 4-3(a).

To study the effects of each parameters on the photovoltage and NEP of the thermopile, we use COMSOL [97] finite element simulation to first calculate the temperature distribution of the substrate upon heating by the laser and then use the derived temperature profile as an input to calculate the thermoelectric voltage. The

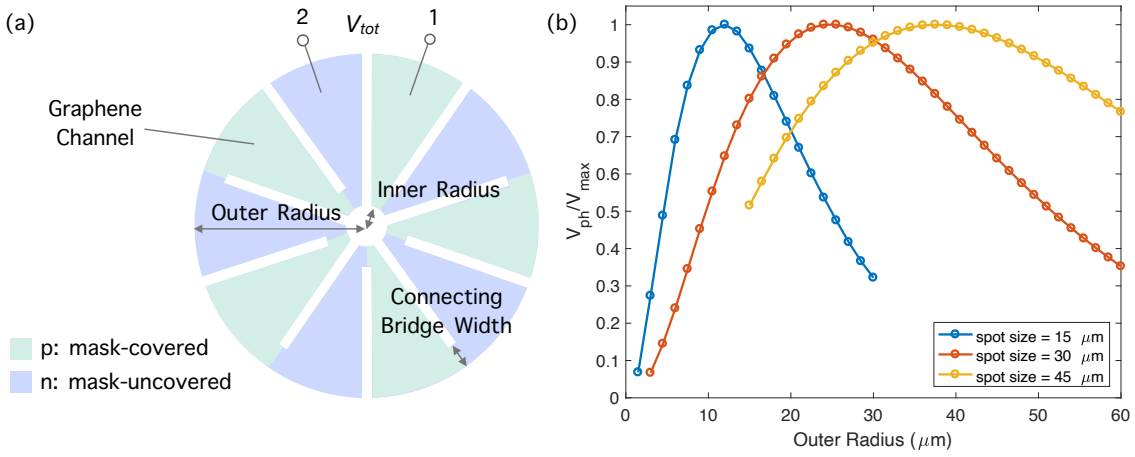

Figure 4-3: (a) Proposed graphene thermopile and the design parameters. (b) Dependence of photovoltage on the dimension of the device, assuming the shape of the device is fixed. Different colors indicate different incident laser spot size.

thermal diffusion in the SiO_2 substrate is governed by the heat equation

$$\rho c_p \frac{\partial T}{\partial t} - \nabla(\kappa \nabla T) = \dot{q} \tag{4.1}$$

where ρ, c_p, and κ are the density, heat capacity, and the thermal conductivity of the material, respectively, and $\dot{q}$ is the heat flux. Constant input laser power with different FWHM spot sizes is inputted as heat flux to the substrate and the resulting temperature profiles at the steady state are obtained. The temperature profiles are then treated as inputs to the thermoelectric process according to equation (3.5) and the photovoltages generated across the thermopile are computed at the two terminals indicated in Fig. 4-3.

Keeping the shape of the device fixed, I first study the influence of the overall device dimension on the photovoltage responsivity for a given laser spot size. Fig. 4-3(b) shows that for a constant laser power profile, the photovoltage obtains a maximum when the outer radius of the thermopile is roughly comparable to the FWHM of the laser power profile. This makes intuitive sense since the majority of the temperature change can be collected along the radial graphene channel when the channel length is comparable to the laser spot radius.

The four parameters mentioned above all have monotonic influence on the pho-

tovoltage responsivity. By increasing the outer radius, decreasing the inner radius, decreasing the connecting bridge width, and increasing the number of voltage source segments of the thermopile, more photovoltage can be collected along the channel because of the increased effective channel length. However, increasing the channel length will also increase the total resistance of the channel, which in turn will result in a larger Johnson-Nyquist noise $v_n = \sqrt{4k_BTR}$ (where k_B is the Boltzmann constant, T is the temperature and R is the total resistance of the device) and increase the NEP of the device, which is another important figure-of-merit for infrared detectors in practice. Figure 4-4 shows the influence of these four parameters on the NEP of the

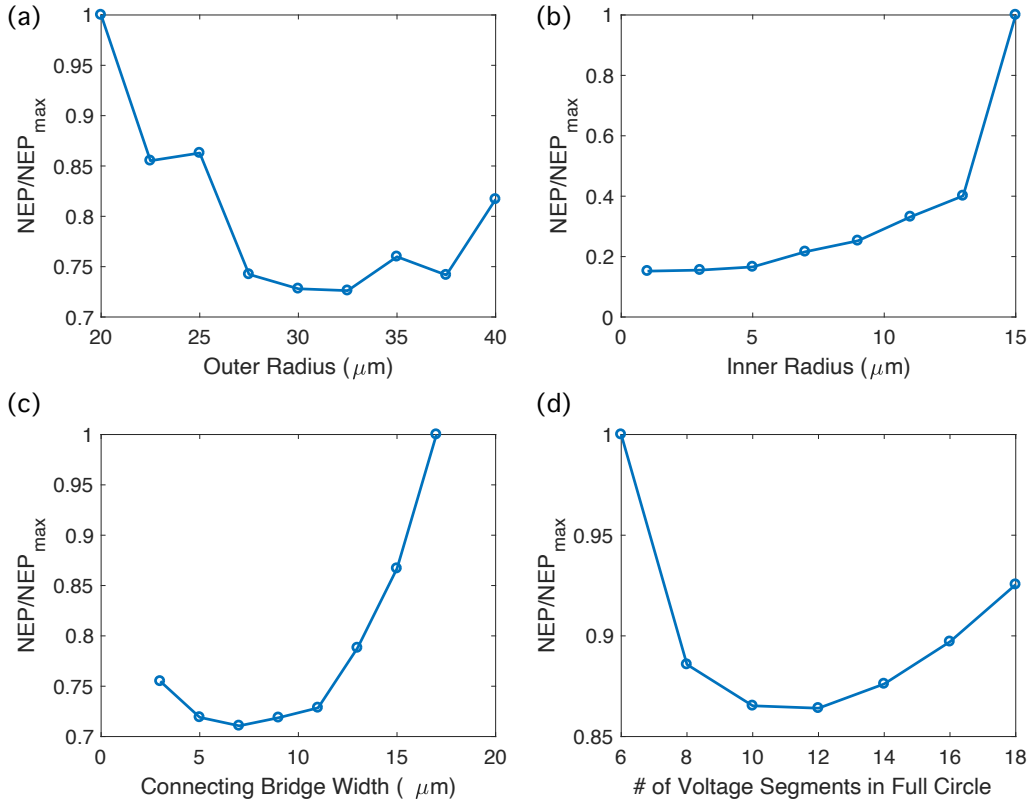

Figure 4-4: Dependence of the noise equivalent power (NEP) of the thermopile on the four design parameters: (a) the outer radius, (b) the inner radius, (c) the connecting bridge width, and (d) the number of voltage source segments in a full circle. The laser spot is fixed to be 30 um.

thermopile. As expected, the monotonic trend in the impact of these parameters on the photovoltage is counter-balanced by the increase of the channel resistance in the

NEP calculation. Therefore an optimized NEP can be achieved by carefully choosing the parameters. Here, I only investigated the effects of each parameters by keeping the other three parameters constant, just to obtain an intuitive understanding of the dependence, but a more comprehensive optimization can be performed across the entire parameter space to achieve a global optimized device design. Such optimization can be done using standard nonlinear optimization algorithms [113].

4.2 High-speed graphene-based photonic devices in near-IR

Thanks to the ultrafast carrier dynamics in graphene that occurs at the picosecond time scale, graphene can respond to rapidly modulated incident light and can generate electro-optic modulation even when driven at a high frequency in excess of GHz. This section summarizes the demonstration of two high-speed graphene-based photonic devices that I have contributed to as part of this thesis. The first is a high-speed graphene photodetector integrated with a silicon photonic waveguide. This detector has a photocurrent responsivity of 0.36 A/W which is comparable to state-of-the-art germanium photodetectors that are used in standard silicon photonic integrated circuits nowadays. The frequency response of the detector exhibits a 3 dB-cutoff of 42 GHz. The second photonic device is a high-speed graphene-based electro-optic modulator integrated with a photonic crystal nanocavity. The nanocavity enhanced light-matter interaction enables efficient electrical tuning of the cavity reflection with a modulation depth of 3.2 dB and a cutoff frequency of 1.2 GHz.

4.2.1 Photodetector in a silicon photonic integrated circuit

Portions of this section have appeared in Reference [8].

The leading photodetector technologies for photonic integrated circuit (PIC) are presently based on bulk semiconductor materials such as Ge [114] and InP [115]. However, the integration of bulk semiconductor-based on-chip detectors has faced

challenges including a spectral response limited by the material's bandgap, an intrinsic speed limited by the material's carrier mobility, and in some cases front-end changes in CMOS processing. The family of 2D materials has emerged as an alternative platform for broadband ultrafast photodetection [116] with its capability to be assembled nearly defect-free into heterostructures and integrated onto PICs.

This section presents the design and demonstration of a graphene-based photodetector integrated with a silicon photonic waveguide. Fig. 4-5(a) illustrates the schematic of this design. The single layer graphene (SLG) is encapsulated by hexagonal boron nitride (hBN). The mobility of BN-encapsulated graphene can reach up to $80\,000\,\mathrm{cm}^2/(\mathrm{Vs})$ at room temperature, exceeding that of traditional semiconductors such as Ge by 1-3 orders of magnitude. The 2D heterostructure is fabricated in a

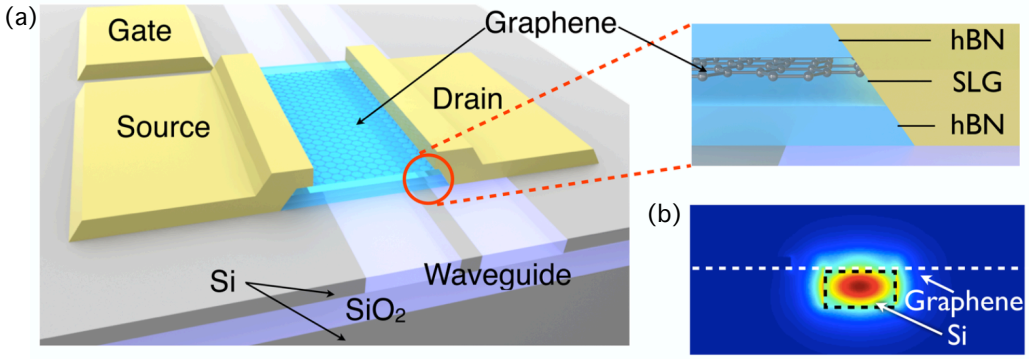

Figure 4-5: (a) Schematic of the hBN/SLG/hBN photodetector on a buried silicon waveguide. (b) The electric field energy density of the fundamental TE waveguide mode, obtained by finite-element simulation. Figure reproduced from [8].

BEOL step on a silicon-on-insulator (SOI) PIC, which was fabricated in a CMOS-compatible process. A waveguide width of 520 nm supports a single transverse-electric (TE) mode shown in the simulated mode in Fig. 4-5(b). The multilayered 2D material stack is assembled onto the photonic chip using van der Waals (vdW) assembly [117]. One-dimensional contacts are formed at the edge of graphene [117], and combined with a wide channel (40 µm) design, enables a device resistance as low as $\sim 77\,\Omega$. Solid polymer electrolyte PEO/$LiClO_4$ is spun on the entire chip to gate the graphene device.

To generate a graphene *p*-*n* junction, one electrode is directly deposited above

the stack on one side of graphene to pin its Fermi level according to the metal's work function. The other side of graphene is electrically gated with electrolyte so its Fermi level is dynamically adjustable. The junction is formed at the edge of the electrode and the electrode is positioned only 200 nm from the waveguide to induce a p-n junction near the optical mode. This process is illustrated in Fig. 4-6(b).

Fig. 4-6(a) presents responsivity measurements as a function of V_{GS} and V_{DS} when the detector is illuminated via the waveguide at 25 µW continuous-wave (c.w.) laser inside the waveguide. Here the responsivity is defined as the ratio of the short-circuit

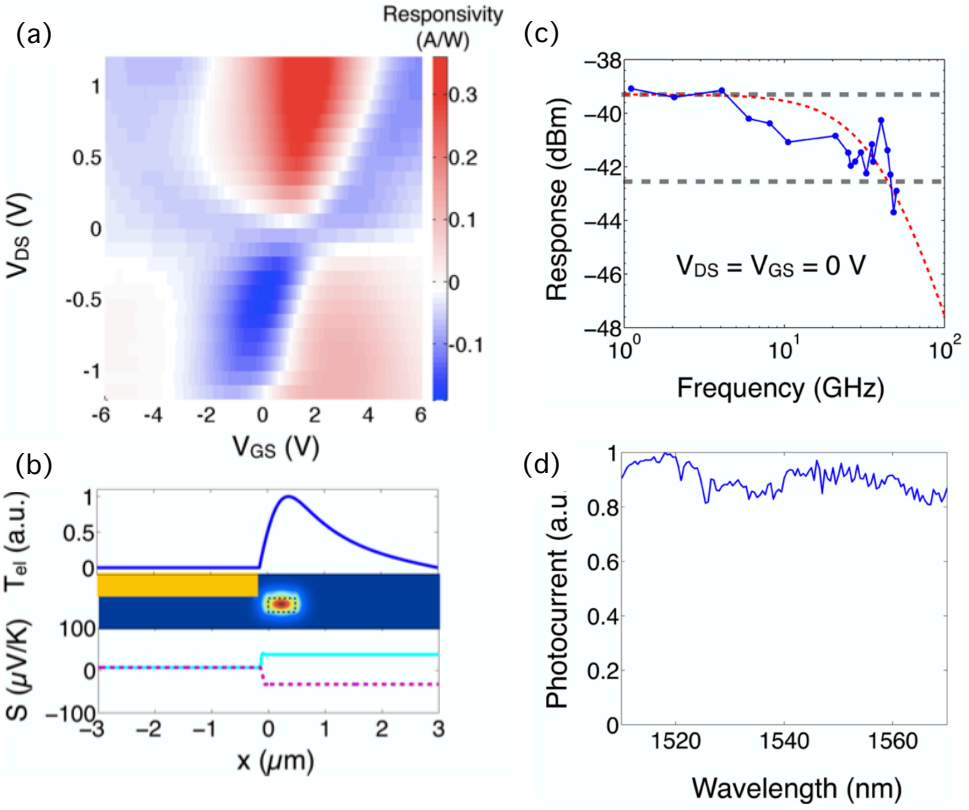

Figure 4-6: (a) Measured responsivity as a function of gate-source V_{GS} and drain-source V_{DS} voltages. (b) Top panel: Electron temperature profile of the SLG under c.w. optical excitation from the waveguide (top panel). Bottom panel: The Seebeck coefficient profiles of the SLG at different V_{GS} and V_{DS}. (c) High-speed response of the graphene photodetector. The red dashed line shows the fitting to the experiment results with a RC low-pass filter model. The extracted 3 dB cutoff frequency is at 42 GHz. (d) Spectral response of the normalized photocurrent for c.w. laser excitation. Figure reproduced from [8].

photocurrent to the optical power in the waveguide, $R = I_{ph}/P_{in}$. The top electrolyte

gate allows independent tuning of graphene's Fermi level across the waveguide mode. Scanning V_{GS} and V_{DS} produces a 6-fold pattern in the photocurrent, which qualitatively matches the behavior of the PTE effect. The photocurrent reaches a maximum of 0.36 A/W at $V_{GS} = 2\,V$ and $V_{DS} = 1.2\,V$, which is a 3-fold improvement over previously reported waveguide-integrated graphene photodetectors [118, 119, 7]

Fig. 4-6(c) shows dynamic response of the detector, measured by coupling two narrowband (1 MHz) laser sources with a detuning frequency Δf ranging from 1 to 50 GHz into the waveguide. The interference of these two laser fields produces an intensity oscillation at frequency Δf. The extracted 3 dB cutoff frequency of this detector is 42 GHz, matching the highest previously reported graphene photodetector speed [120]. The spectral response shown in Fig. 4-6(d) indicates broadband operation wavelength range from 1510 to 1570 nm.

4.2.2 Modulator with photonic crystal nanocavity

Portions of this section have appeared in Reference [9].

This section leverages graphene's high-speed electro-optic property for the demonstration of a graphene-based high-speed free-space amplitude modulator. Previously, several prototype graphene electro-optic modulators have been realized by integrating graphene with cavities [121, 122]. However, these devices require electrolyte gating to change graphene's Fermi level, which is not ideal for dynamic modulation due to the limited modulation speed to kHz.

Here, a modulator device concept based on a graphene-hBN-graphene capacitor integrated with a planar photonic crystal (PPC) cavity is demonstrated. The device geometry is illustrated in Fig. 4-7(a). The PPC cavity greatly amplifies the absorption of light into the two graphene sheets. The modulation occurs as the top and bottom graphene layers are oppositely doped by the induced electrostatic potential; when the respective Fermi levels are shifted to larger than half of the incident photon energy, Pauli blocking suppresses the optical absorption and leads to increased cavity reflectivity. This can be described using graphene's optical conductivity introduced in Sec. 3.1.2 and is conceptually illustrated in the upper panel of Fig. 4-7(b). The

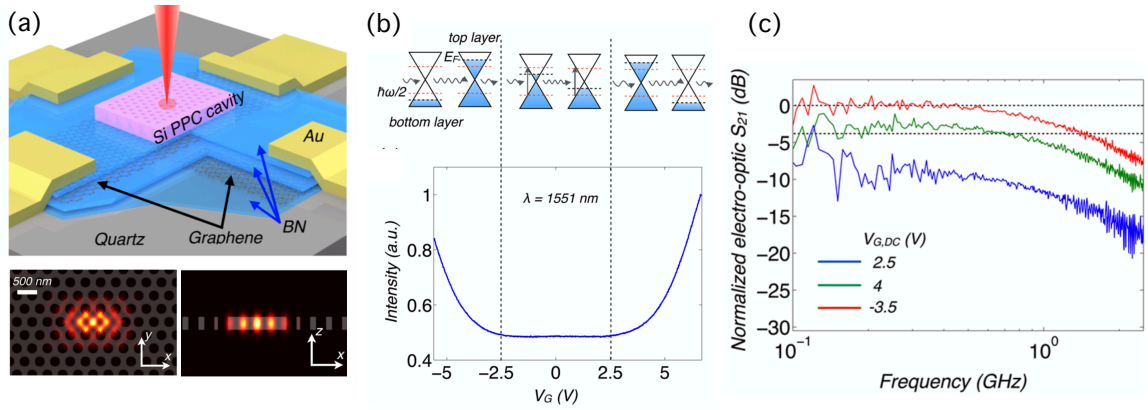

Figure 4-7: (a) Top panel: Schematic of the cavity-graphene electro-optic modulator. Bottom panel: FDTD simulation of the cavity energy intensity from the top and from the side. (b) Top panel: Band diagram of two graphene sheets at different gate voltage illustrating the concept of the modulator. Bottom panel: Normalized reflection intensity of the cavity at $\lambda = 1551\,\text{nm}$ as a function of V_G. (c) Normalized electro-optic S_{21} frequency response of the graphene modulator at different DC gate voltages. Black dashed lines indicate 0 and $-3\,\text{dB}$, respectively. Figure reproduced from [9].

lower panel of Fig. 4-7(b) shows reflectivity modulation with a depth of 3.2 dB within a voltage swing of only 2.5 V.

The dynamic modulation characteristic of this modulator is measured by coupling in RF power from a 20 GHz network analyzer (NWA), detecting the modulated reflected light with an InGaAs avalanche photodiode (APD), and sending the electrical signal of the APD back into the NWA and measuring the S_{21} parameter. Fig. 4-7(c) shows the normalized S_{21} as a function of the modulation frequency for three different gate voltages, indicating a 3 dB cutoff frequency of 1.2 GHz. The cutoff frequency is limited by the RC time constant of the graphene-hBN-graphene capacitor.

4.3 Probing the ultimate confinement of graphene plasmons

Portions of this section have appeared in Reference [10].

Apart from the interests in graphene for modulation and photodetection applications, there are numerous other opportunities offered by graphene in optics and

photonics, including plasmonics, polaritonics, nonlinear optics, to name a few. In particular, plasmons in graphene have promised extreme confinement of light into tiny spatial dimensions, which offers appealing avenues for applications such as microscopy, sensing, and nanoscale lasers. This section summarizes one collaborative effort with the Institute of Photonic Sciences (ICFO, Spain) in the fundamental investigation of the ultimate confinement of plasmons in graphene, where a graphene-hBN-metal platform allows the physical limits of (out-of-plane) confinement of propagating plasmons down to the ultimate physical boundary of a one-atom-thick layer ($\lambda_0/26000$) without sacrifices in damping.

Plasmons have long been regarded as a pathway for confining light below the diffraction limit. For bulk-metal based plasmonic systems, tapers [123], grooves [124], and metal-insulator-metal waveguides [125] have been proposed for confining propagating or resonant plasmons. However, Landau damping in metals imposes a trade-off between optical field confinement and losses. For plasmons in two-dimensional materials, the restoring force by the long-range Coulomb interactions can be controlled by tailoring the external environment. This is fundamentally different from bulk metal-based plasmonic systems. The device geometry discussed in this section aims to achieve out-of-plane plasmon confinement and wavelength compression through engineering of graphene's external environment.

Fig. 4-8(a) illustrates the device consisting of graphene encapsulated by atomically thin dielectric material hBN and covered by a metallic rod array. The advantages of the periodic metal-insulator-graphene system are twofold. First, the presence of the metal results in efficient screening of the graphene plasmons, squeezing the so-called screened graphene plasmons (SGPs) into the graphene-metal gap without reducing their lifetime. Second, metal rods facilitate efficient coupling between far-field light and the strongly confined plasmons, where the width of the rods defines the resonant conditions for the plasmon modes. Fig. 4-8(b) illustrates FDTD simulation of the field profile of a unit cell, showing plasmons launched at the metal edges and confined between the metal and graphene. Bringing the metal closer to graphene enhances the vertical confinement, as shown both in the FDTD simulation and in the graphene

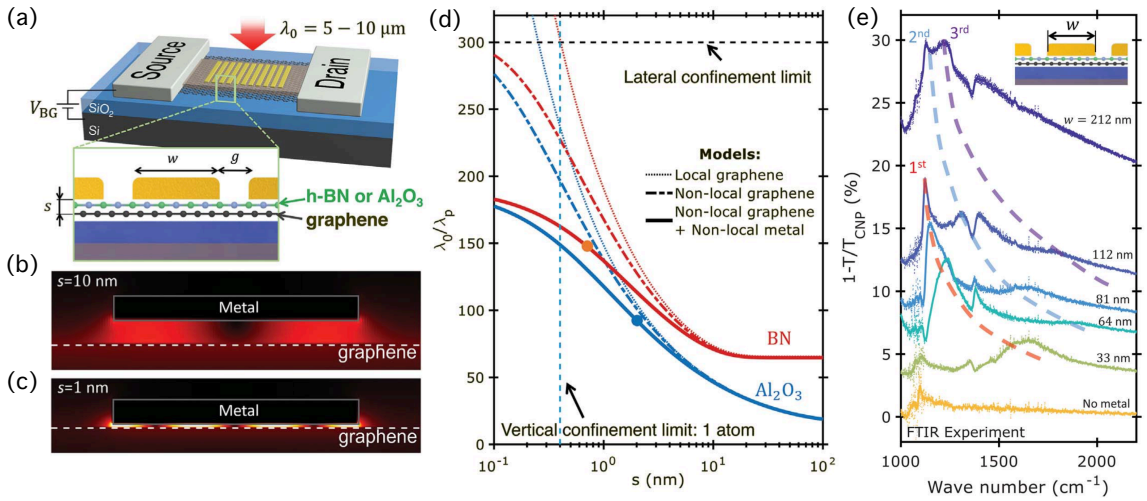

Figure 4-8: (a) Device design for probing ultimate plasmon confinement limits. Graphene is encapsulated in a dielectric and covered by an array of gold rods. A gate voltage V_{BG} is applied between Si and graphene to control the Fermi level of graphene. (b) and (c) Simulated plasmonic field magnitude profiles for metal-graphene separations of 10 and 1 nm. (d) Simulated plasmon wavelength, λ_p, as a function of metal-graphene spacer thickness s for the two materials used in the experiments. The vertical dashed line refers to the fundamental limit: a monolayer h-BN spacer. Colored circles correspond to the two sets of devices discussed in the paper. The dotted lines represent the model where the metal was considered as a perfect conductor in combination with the local graphene conductivity model. The dash-dotted lines represent the nonlocal graphene conductivity model (obtained from the random-phase-approximation), but still metal as a perfect conductor. The solid lines represent the model where nonlocal optical response for both metal and graphene is considered. (e) Extinction spectra for w ranging from 33 to 212 nm, fixed $g = 38 \pm 4$ nm, and fixed $E_f = 540$ meV. Dashed lines are guides to the eye showing the evolution of each resonance with w. Figure reproduced from [10].

conductivity model prediction in Fig. 4-8(b). To this end, in this device a monolayer of hBN spacer is used, vertically confining the plasmon below 1 nm.

The coupling between far-field light and the confined plasmons through metal gratings allows probing the system with Fourier transform infrared (FTIR) transmission measurements. Fig. 4-8(c) shows the extinction spectra obtained for different metal ribbon widths. For all ribbon widths, there are clearly visible graphene plasmonic resonance peaks, indicating that the extreme confinement in the vertical direction does not introduce intolerable optical loss. Even with a ribbon width $w = 33$ nm where both the lateral confinement and the vertical confinement are strong, the graphene

plasmon still shows a visible resonance with high extinction values.

This fundamental investigation shows that 2D-material heterostructures can be considered as a powerful toolbox for nanophotonics with vertical subnanometer precision. The metallic structure can also be used as a nearby efficient gate to enable molecular sensing with even higher resolution, to enhance nonlinear effects, or to design photodetectors with plasmon-enhanced sensitivity and tunability.

4.4 Outlook

The work presented in this chapter are initial demonstrations of photonic devices enabled by electrically-modulated graphene, showing it will be possible to engineer device designs to fully utilize some of graphene's properties that are fundamentally different from those of other materials not atomically thin. However, to gain full advantage of these and to realize performances that can unambiguously beat the state-of-the-art technologies, further improvements are needed in several aspects.

For high-speed graphene electro-optic modulation and photodetection, the currently demonstrated devices are limited by their RC time constant in terms of operation speed. It is necessary to optimize the device geometry and reduce the footprint for smaller resistance and parasitic capacitance in order to push the speed into the intrinsically-limited regime of hundreds of GHz. In addition, free-space graphene modulators based on nanocavities have the potential to be arranged in a two-dimensional array for the realization of the high-speed SLM architecture based on tunable cavity arrays. To this end, a large-scale demonstration of modulator arrays based on chemical-vapor-deposited (CVD) large-area graphene and hBN would be useful. This calls for an improved graphene material platform from a material synthesis perspective as well, where high-quality graphene with little nanoscale strain variation and few defects is required for high carrier mobility. This improved material synthesis process will also benefit further demonstration of device concepts based on graphene plasmons, where currently the quality factor of plasmonic nanoresonators is limited by graphene's low carrier mobility in large-area samples.

Chapter 5

Conclusions and Outlook

We are at an exciting stage in the field of optoelectronic devices for optical control. More and more technologies in data communications, high-performance computing, display, imaging, artificial intelligence, and quantum computation are now demanding a device capable of spatiotemporal modulation of light at high speeds. With the emergence of novel materials, new synthesis methods that enable bulky conventional materials to be presented with new form factors, and the perfection of nanofabrication and manufacturing process and techniques, new avenues are now open where fundamentally different electro-optic phenomena can be exploited to enable new functionalities such as high-speed modulation.

However, the transition from new material platforms to new electro-optic modulation technologies is not straight-forward. To take advantage of the fast intrinsic response provided by the new materials means having to sacrifice other excellent properties of the previously used material or having to abandon mature manufacturing processes that over the years have been perfected for scalability and low cost.

The research presented in this thesis aims to bridge this gap and to explore spatial light modulator designs where new materials can be utilized for their fast response time without having to modify the SLM's other figure-of-merits, including the modulation mode, driving voltage, pixel pitch, efficiency, array size, and the CMOS compatibility. While it was not possible in this thesis to experimentally realize such a holy grail, the work presented here made several initial exploratory attempts in the

theory and design and laid out a road map that should lead to the demonstration of a high-speed spatial light modulator with high diffraction efficiency, CMOS-compatible driving voltages, and a CMOS-compatible manufacturing process.

5.1 High-Speed SLM Architecture with Tunable Microcavity Arrays

This thesis proposes a SLM architecture based on arrays of electrically-tunable microcavites. The microcavities are used as a way to enhance high-speed electro-optic effects that are typically very weak, and also as a method to engineer the amplitude and phase of the reflected light. A general design methodology that combines analytical modeling of the microcavities with FDTD numerical simulations is developed for systematic optimization of microcavities according to design requirements such as reflectivity and driving voltages [43].

This has led to two optimized designs, one for the phase-only modulation mode and another for the amplitude mode, both able to achieve cavity resonance shifts of more than a linewidth at standard-CMOS-compatible voltages of less than 2 V with the Pockels material $BaTiO_3$. While the microcavity's mode confinement is beneficial for light-matter interaction and for avoiding neighboring pixel crosstalk, it limits the fill factor of the pixel which consequently leads to low diffraction efficiency. A phase mask is included in the architecture as a way to expand the fill factor via mode propagation and to compensate the phase curvature as a result of the propagation.

The experimental realization of these designs as a fully functional microcavity array with high-speed independent electronic control to each pixel is the obvious next step. Although a design for trivial fabrication and experimental implementation is proposed and optimized for proof-of-principle demonstration, the performance of this design is less than ideal in terms of driving voltage due to the low cavity quality factor allowed with the external microcavity array design. The ultimate realization of a high-speed SLM with CMOS-compatible driving voltages calls for the implementation of

the micropillar vertical cavity design or the Gaussian defect vertical cavity design. The high-speed individual electronic control of each pixel also necessitates large-scale high-speed logic gates such as those offered by CMOS circuitry. The schematic of such architecture is illustrated in Fig. 5-1.

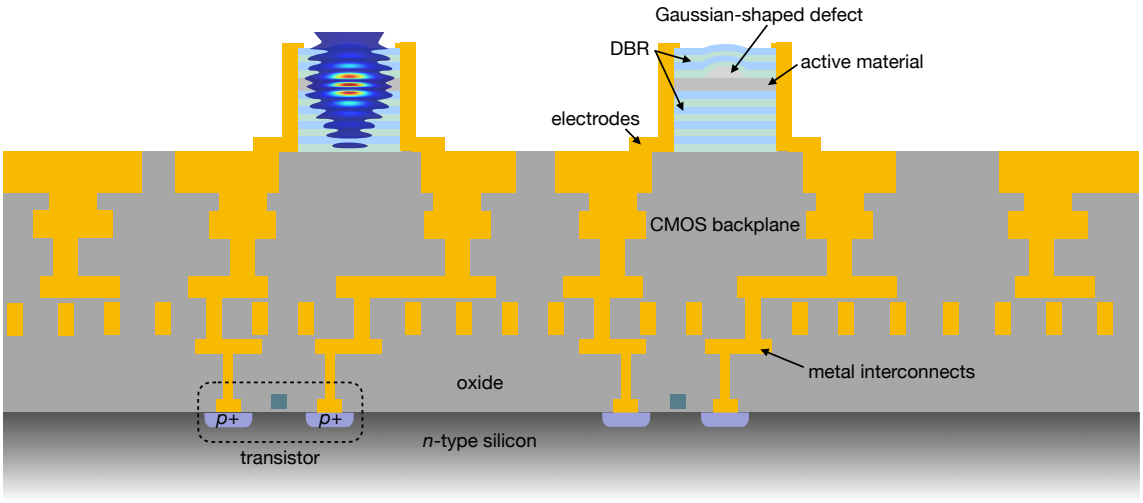

Figure 5-1: Schematic cross section of spatial light modulators with two-dimensional tunable microcavity arrays on a complementary metal-oxide-semiconductor (CMOS) backplane. Each phase shifter pixel consists of a one-sided vertical microcavity laterally confined by a Gaussian-shaped defect, with electrical contacts connected to the CMOS driving circuit.

Several key challenges in the fabrication of this structure include: (1) the Gaussian shape definition; (2) the deposition of the side metal contact; and (3) the implementation of the phase mask (not illustrated here).

When defining the Gaussian shape, it is important to maintain enough accuracy of the shape, because deviation from the shape can lead to degradation of the cavity's intrinsic quality factor (shown in Sec. 2.3.3). Three potential approaches can be used for this process, including direct resist reflow, grayscale resist lithography followed by reflow, and resist reflow followed by substrate etching. Direct resist reflow is the simplest process but allows limited control of the reflowed shape. Reflow followed by etching adds another control step enabled by selectivity engineering of the etching process. Grayscale lithography followed by reflow offers the most versatility through a pre-shaping of the resist before the reflow process.

The deposition of the side contact can be realized by angled evaporation or sputtering. Here, it is the best to use a photoresist with a thickness larger than the height of the microcavity which is a few micrometers tall. If angled evaporation is used, when opening windows for the metal deposition, it is necessary to make sure that the aspect ratio of the window is not too large. This ensures that the metal can reach the surface of the substrate without getting blocked. The phase mask concept allows each vertical pillar to be placed several micrometers from each other, which strongly reduces the precision requirement and difficulty for the fabrication.

The phase mask can be implemented with 3D grayscale lithography as in Sec. 2.5.2 or nanoimprint lithography. Because the phase curvature for the Gaussian-defect vertical at the location of the mask resembles that of a spherical wave, the phase mask can also be replaced by a microlens array to achieve similar performance. Here, precise alignment of the mask to existing microcavities underneath is necessary.

5.2 High-Speed Electro-Optic Material Graphene

On the material side, this thesis investigates the novel 2D material graphene and proposes and demonstrates a graphene surface dynamical electrical gating technique that has spatial resolution down to $< 30\,\mathrm{nm}$ [65].

While most photonic devices demonstrated in this thesis do not directly take advantage of this technique, this technique can enable future demonstration of high-quality graphene plasmonic metasurfaces when combined with a high-quality CVD encapsulated graphene platform [126]. In particular, by creating nanoscale periodic modulation of the graphene Fermi level, plasmonic nanoresonators can be created without degradation of the quality factor due to edge effects caused by harsh etching process. The CVD-grown graphene sandwiched by two uniform CVD-grown hBN films can also provide a flat substrate with minimal nanoscale strain variation and an encapsulation that protects graphene from the environment, both leading to higher carrier mobility.

The technique can also benefit from further experimentation of different electrolyte

and mask materials. For example, an ion with a larger atomic number is advantageous for two reasons. First, a larger ionic radius makes it harder for the ions to permeate through the mask's pin holes, implying better mask protection. Second, a larger ionic mass leads to a lower ionic polarization resonance frequency. This means that the optical absorption will be reduced in the electrolyte, especially in the mid-infrared or terahertz range.

5.3 Outlook

In conclusion, the research presented in this thesis represents a step towards the demonstration of a new high-speed spatial light modulator architecture for spatiotemporal control of light. With subsequently developed fabrication processes and integration with a CMOS backplane, a GHz spatial light modulator with near unity diffraction efficiency and standard-CMOS-compatible driving voltages is possible in both phase-only and amplitude modulation modes. This new technology would strongly advance applications such as optical interconnects, optical information processing, quantum computation, imaging, display, and programmable optical tweezers.

Bibliography

[1] `https://waymo.com`. Accessed on 2020-04-25.

[2] Donggyu Kim, Alexander Keesling, Ahmed Omran, Harry Levine, Hannes Bernien, Markus Greiner, Mikhail D Lukin, and Dirk R Englund. Large-scale uniform optical focus array generation with a phase spatial light modulator. *Optics Letters*, 44(12):3178–3181, 2019.

[3] Daniel Barredo, Vincent Lienhard, Sylvain De Leseleuc, Thierry Lahaye, and Antoine Browaeys. Synthetic three-dimensional atomic structures assembled atom by atom. *Nature*, 561(7721):79–82, 2018.

[4] `http://www.ti.com/dlp-chip/overview.html`. Accessed on 2020-04-25.

[5] Xing Lin, Yair Rivenson, Nezih T Yardimci, Muhammed Veli, Yi Luo, Mona Jarrahi, and Aydogan Ozcan. All-optical machine learning using diffractive deep neural networks. *Science*, 361(6406):1004–1008, 2018.

[6] Sebastian A Vasquez-Lopez, Raphaël Turcotte, Vadim Koren, Martin Plöschner, Zahid Padamsey, Martin J Booth, Tomáš Čižmár, and Nigel J Emptage. Subcellular spatial resolution achieved for deep-brain imaging in vivo using a minimally invasive multimode fiber. *Light: Science & Applications*, 7(1):1–6, 2018.

[7] Ke Wang, Ampalavanapillai Nirmalathas, Christina Lim, Efstratios Skafidas, and Kamal Alameh. High-speed reconfigurable card-to-card optical interconnects based on hybrid free-space and multi-mode fiber propagations. *Optics express*, 21(25):31166–31175, 2013.

[8] Ren-Jye Shiue, Yuanda Gao, Yifei Wang, Cheng Peng, Alexander D Robertson, Dmitri K Efetov, Solomon Assefa, Frank HL Koppens, James Hone, and Dirk Englund. High-responsivity graphene–boron nitride photodetector and autocorrelator in a silicon photonic integrated circuit. *Nano letters*, 15(11):7288–7293, 2015.

[9] Yuanda Gao, Ren-Jye Shiue, Xuetao Gan, Luozhou Li, Cheng Peng, Inanc Meric, Lei Wang, Attila Szep, Dennis Walker Jr, James Hone, et al. High-speed electro-optic modulator integrated with graphene-boron nitride heterostructure and photonic crystal nanocavity. *Nano letters*, 15(3):2001–2005, 2015.

[10] David Alcaraz Iranzo, Sébastien Nanot, Eduardo JC Dias, Itai Epstein, Cheng Peng, Dmitri K Efetov, Mark B Lundeberg, Romain Parret, Johann Osmond, Jin-Yong Hong, et al. Probing the ultimate plasmon confinement limits with a van der waals heterostructure. *Science*, 360(6386):291–295, 2018.

[11] Brent Schwarz. Lidar: Mapping the world in 3d. *Nature Photonics*, 4(7):429, 2010.

[12] Emil Haellstig, Johan Stigwall, Mikael Lindgren, and Lars Sjoqvist. Laser beam steering and tracking using a liquid crystal spatial light modulator. In *Laser Systems Technology*, pages 13–23. International Society for Optics and Photonics, 2003.

[13] David Vettese. Microdisplays: Liquid crystal on silicon. *Nature Photonics*, 4(11):752, 2010.

[14] Andrew Forbes, Angela Dudley, and Melanie McLaren. Creation and detection of optical modes with spatial light modulators. *Advances in Optics and Photonics*, 8(2):200–227, 2016.

[15] Claire M Watts, David Shrekenhamer, John Montoya, Guy Lipworth, John Hunt, Timothy Sleasman, Sanjay Krishna, David R Smith, and Willie J Padilla. Terahertz compressive imaging with metamaterial spatial light modulators. *Nature Photonics*, 8(8):605, 2014.

[16] Ryan Hamerly, Liane Bernstein, Alexander Sludds, Marin Soljačić, and Dirk Englund. Large-scale optical neural networks based on photoelectric multiplication. *Physical Review X*, 9(2):021032, 2019.

[17] Joseph M Kahn and David AB Miller. Communications expands its space. *Nature Photonics*, 11(1):5, 2017.

[18] Florence Nogrette, Henning Labuhn, Sylvain Ravets, Daniel Barredo, Lucas Béguin, Aline Vernier, Thierry Lahaye, and Antoine Browaeys. Single-atom trapping in holographic 2d arrays of microtraps with arbitrary geometries. *Physical Review X*, 4(2):021034, 2014.

[19] AG Holoeye Photonics. Holoeye corporation. `http://www.holoeye.com`.

[20] Charley J Henderson, Diego Gil Leyva, and Timothy D Wilkinson. Free space adaptive optical interconnect at 1.25 gb/s, with beam steering using a ferroelectric liquid-crystal slm. *Journal of Lightwave Technology*, 24(5):1989–1997, 2006.

[21] Dana Dudley, Walter M Duncan, and John Slaughter. Emerging digital micromirror device (dmd) applications. In *MOEMS display and imaging systems*, pages 14–26. International Society for Optics and Photonics, 2003.

[22] Vern Shrauger and Cardinal Warde. Development of a high-speed high-fill-factor phase-only spatial light modulator. In *Diffractive and Holographic Technologies for Integrated Photonic Systems*, pages 101–109. International Society for Optics and Photonics, 2001.

[23] Zichen Zhang, Zheng You, and Daping Chu. Fundamentals of phase-only liquid crystal on silicon (lcos) devices. *Light: Science & Applications*, 3(10):e213, 2014.

[24] W Merlijn Van Spengen. Mems reliability from a failure mechanisms perspective. *Microelectronics Reliability*, 43(7):1049–1060, 2003.

[25] Yu Horie, Amir Arbabi, Ehsan Arbabi, Seyedeh Mahsa Kamali, and Andrei Faraon. High-speed, phase-dominant spatial light modulation with silicon-based active resonant antennas. *ACS Photonics*, 5(5):1711–1717, 2017.

[26] Youmin Wang, Guangya Zhou, Xiaosheng Zhang, Kyungmok Kwon, Pierre-A Blanche, Nicholas Triesault, Kyoung-sik Yu, and Ming C Wu. 2d broadband beamsteering with large-scale mems optical phased array. *Optica*, 6(5):557–562, 2019.

[27] Pin Chieh Wu, Ragip A Pala, Ghazaleh Kafaie Shirmanesh, Wen-Hui Cheng, Ruzan Sokhoyan, Meir Grajower, Muhammad Z Alam, Duhyun Lee, and Harry A Atwater. Dynamic beam steering with all-dielectric electro-optic iii–v multiple-quantum-well metasurfaces. *Nature communications*, 10(1):1–9, 2019.

[28] Richard A Soref. Silicon spatial light modulator, October 20 1992. US Patent 5,157,538.

[29] Yao-Wei Huang, Ho Wai Howard Lee, Ruzan Sokhoyan, Ragip A Pala, Krishnan Thyagarajan, Seunghoon Han, Din Ping Tsai, and Harry A Atwater. Gate-tunable conducting oxide metasurfaces. *Nano Letters*, 16(9):5319–5325, 2016.

[30] Michelle C Sherrott, Philip WC Hon, Katherine T Fountaine, Juan C Garcia, Samuel M Ponti, Victor W Brar, Luke A Sweatlock, and Harry A Atwater. Experimental demonstration of$>$ 230 phase modulation in gate-tunable graphene–gold reconfigurable mid-infrared metasurfaces. *Nano letters*, 17(5):3027–3034, 2017.

[31] Cheng Wang, Mian Zhang, Xi Chen, Maxime Bertrand, Amirhassan Shams-Ansari, Sethumadhavan Chandrasekhar, Peter Winzer, and Marko Lončar. Integrated lithium niobate electro-optic modulators operating at cmos-compatible voltages. *Nature*, 562(7725):101–104, 2018.

[32] Stefan Abel, Felix Eltes, J. Elliott Ortmann, Andreas Messner, Pau Castera, Tino Wagner, Darius Urbonas, Alvaro Rosa, Ana M. Gutierrez, Domenico Tulli, Ping Ma, Benedikt Baeuerle, Arne Josten, Wolfgang Heni, Daniele Caimi, Lukas Czornomaz, Alexander A. Demkov, Juerg Leuthold, Pablo Sanchis, and Jean

Fompeyrine. Large pockels effect in micro-and nanostructured barium titanate integrated on silicon. *Nature Materials*, 18(1):42, 2019.

[33] James R Fienup. Phase retrieval algorithms: a comparison. *Applied Optics*, 21(15):2758–2769, 1982.

[34] Robert W Boyd. *Nonlinear optics*. Academic press, 2019.

[35] Stefan Abel, Thilo Stöferle, Chiara Marchiori, Christophe Rossel, Marta D. Rossell, Rolf Erni, Daniele Caimi, Marilyne Sousa, Alexei Chelnokov, Bert J. Offrein, and Jean Fompeyrine. A strong electro-optically active lead-free ferroelectric integrated on silicon. *Nature Communications*, 4:1671, 2013.

[36] N Daix, E Uccelli, L Czornomaz, D Caimi, C Rossel, M Sousa, H Siegwart, C Marchiori, JM Hartmann, K-T Shiu, et al. Towards large size substrates for iii-v co-integration made by direct wafer bonding on si. *APL materials*, 2(8):086104, 2014.

[37] Felix Eltes, Christian Mai, Daniele Caimi, Marcel Kroh, Youri Popoff, Georg Winzer, Despoina Petousi, Stefan Lischke, J Elliott Ortmann, Lukas Czornomaz, et al. A batio 3-based electro-optic pockels modulator monolithically integrated on an advanced silicon photonics platform. *Journal of Lightwave Technology*, 37(5):1456–1462, 2019.

[38] Kristy J Kormondy, Youri Popoff, Marilyne Sousa, Felix Eltes, Daniele Caimi, Marta D Rossell, Manfred Fiebig, Patrik Hoffmann, Chiara Marchiori, Michael Reinke, Morgan Trassin, Alexander A Demkov, Jean Fompeyrine, and Stefan Abel. Microstructure and ferroelectricity of batio3 thin films on si for integrated photonics. *Nanotechnology*, 28(7):075706, 2017.

[39] Mian Zhang, Cheng Wang, Rebecca Cheng, Amirhassan Shams-Ansari, and Marko Lončar. Monolithic ultra-high-q lithium niobate microring resonator. *Optica*, 4(12):1536–1537, 2017.

[40] Hanxiao Liang, Rui Luo, Yang He, Haowei Jiang, and Qiang Lin. High-quality lithium niobate photonic crystal nanocavities. *Optica*, 4(10):1251–1258, 2017.

[41] Victor Arrizón, Guadalupe Méndez, and David Sánchez-de La-Llave. Accurate encoding of arbitrary complex fields with amplitude-only liquid crystal spatial light modulators. *Optics express*, 13(20):7913–7927, 2005.

[42] Shaohua Tao, XiaoCong Yuan, and Wai Chye Cheong. Comparison of amplitude-and phase-holograms. In *Design, Fabrication, and Characterization of Photonic Devices II*, volume 4594, pages 459–463. International Society for Optics and Photonics, 2001.

[43] Cheng Peng, Ryan Hamerly, Mohammad Soltani, and Dirk R Englund. Design of high-speed phase-only spatial light modulators with two-dimensional tunable microcavity arrays. *Optics express*, 27(21):30669–30680, 2019.

[44] Hermann A Haus. *Waves and fields in optoelectronics*. Prentice-Hall,, 1984.

[45] A Petraru, M Siegert, M Schmid, J Schubert, and Ch Buchal. Ferroelectic batio 3 thin film optical waveguide modulators. *MRS Online Proceedings Library Archive*, 688, 2001.

[46] Lumerical. F.d.t.d. solutions, 2019.

[47] Mikhail N. Polyanskiy. Refractive index database. `https://refractiveindex.info`. Accessed on 2019-08-01.

[48] `www.semiaccurate.com/2012/12/10/intel-talks-about-22nm-soc-transistors/`. Accessed on 2020-04-28.

[49] Fei Ding, Thilo Stöferle, Lijian Mai, Armin Knoll, and Rainer F Mahrt. Vertical microcavities with high q and strong lateral mode confinement. *Physical Review B*, 87(16):161116, 2013.

[50] Stephen Y Chou, Peter R Krauss, and Preston J Renstrom. Nanoimprint lithography. *Journal of Vacuum Science & Technology B: Microelectronics and Nanometer Structures Processing, Measurement, and Phenomena*, 14(6):4129–4133, 1996.

[51] Amir Arbabi, Yu Horie, Mahmood Bagheri, and Andrei Faraon. Dielectric metasurfaces for complete control of phase and polarization with subwavelength spatial resolution and high transmission. *Nature nanotechnology*, 10(11):937, 2015.

[52] L Jay Guo. Nanoimprint lithography: methods and material requirements. *Advanced materials*, 19(4):495–513, 2007.

[53] Nadya Anscombe. Direct laser writing. *Nature Photonics*, 4(1):22–23, 2010.

[54] J McPherson, J-Y Kim, A Shanware, and H Mogul. Thermochemical description of dielectric breakdown in high dielectric constant materials. *Applied Physics Letters*, 82:2121, 2003.

[55] Cédric Sire, Serge Blonkowski, Michael J Gordon, and Thierry Baron. Statistics of electrical breakdown field in hfo2 and sio2 films from millimeter to nanometer length scales. *Applied Physics Letters*, 91(24):2905, 2007.

[56] Yoshiaki Hattori, Takashi Taniguchi, Kenji Watanabe, and Kosuke Nagashio. Layer-by-layer dielectric breakdown of hexagonal boron nitride. *ACS nano*, 9(1):916–921, 2014.

[57] K Ueno, S Nakamura, H Shimotani, A Ohtomo, N Kimura, T Nojima, H Aoki, Y Iwasa, and M Kawasaki. Electric-field-induced superconductivity in an insulator. *Nature materials*, 7(11):855–858, 2008.

[58] Dmitri K Efetov and Philip Kim. Controlling electron-phonon interactions in graphene at ultrahigh carrier densities. *Physical review letters*, 105(25):256805, 2010.

[59] Hongtao Yuan, Hidekazu Shimotani, Atsushi Tsukazaki, Akira Ohtomo, Masashi Kawasaki, and Yoshihiro Iwasa. High-density carrier accumulation in zno field-effect transistors gated by electric double layers of ionic liquids. *Advanced Functional Materials*, 19(7):1046–1053, 2009.

[60] Dmitri K Efetov. Towards inducing superconductivity into graphene. 2014.

[61] Qiaoliang Bao and Kian Ping Loh. Graphene photonics, plasmonics, and broadband optoelectronic devices. *ACS nano*, 6(5):3677–3694, 2012.

[62] LA Falkovsky. Optical properties of graphene. In *Journal of Physics: Conference Series*, volume 129, page 012004. IOP Publishing, 2008.

[63] ZQ Li, Eric A Henriksen, Z Jiang, Zhao Hao, Michael C Martin, P Kim, HL Stormer, and Dimitri N Basov. Dirac charge dynamics in graphene by infrared spectroscopy. *Nature Physics*, 4(7):532–535, 2008.

[64] Justin CW Song, Mark S Rudner, Charles M Marcus, and Leonid S Levitov. Hot carrier transport and photocurrent response in graphene. *Nano letters*, 11(11):4688–4692, 2011.

[65] Cheng Peng, Sebastien Nanot, Ren-Jye Shiue, Gabriele Grosso, Yafang Yang, Marek Hempel, Pablo Jarillo-Herrero, Jing Kong, Frank HL Koppens, Dmitri K Efetov, et al. Compact mid-infrared graphene thermopile enabled by a nanopatterning technique of electrolyte gates. *New Journal of Physics*, 20(8):083050, 2018.

[66] Donald A Neamen. *Semiconductor physics and devices*. McGraw-Hill Higher Education, 2003.

[67] Shun Lien Chuang. *Physics of photonic devices*, volume 80. John Wiley & Sons, 2012.

[68] Andrea C. Ferrari, Francesco Bonaccorso, Vladimir Falko, Konstantin S. Novoselov, Stephan Roche, Peter Bøggild, Stefano Borini, Frank Koppens, Vincenzo Palermo, Nicola Pugno, José a. Garrido, Roman Sordan, Alberto Bianco, Laura Ballerini, Maurizio Prato, Elefteris Lidorikis, Jani Kivioja, Claudio Marinelli, Tapani Ryhänen, Alberto Morpurgo, Jonathan N. Coleman, Valeria Nicolosi, Luigi Colombo, Albert Fert, Mar Garcia-Hernandez, Adrian Bachtold, Gregory F. Schneider, Francisco Guinea, Cees Dekker, Matteo Barbone, Costas Galiotis, Alexander Grigorenko, Gerasimos Konstantatos, Andras Kis, Mikhail Katsnelson, Carlo W. J. Beenakker, Lieven Vandersypen, Annick Loiseau, Vittorio Morandi, Daniel Neumaier, Emanuele Treossi, Vittorio Pellegrini, Marco Polini, Alessandro Tredicucci, Gareth M. Williams, Byung Hee

Hong, Jong Hyun Ahn, Jong Min Kim, Herbert Zirath, Bart J. van Wees, Herre van der Zant, Luigi Occhipinti, Andrea Di Matteo, Ian a. Kinloch, Thomas Seyller, Etienne Quesnel, Xinliang Feng, Ken Teo, Nalin Rupesinghe, Pertti Hakonen, Simon R. T. Neil, Quentin Tannock, Tomas Löfwander, and Jari Kinaret. Science and technology roadmap for graphene, related two-dimensional crystals, and hybrid systems. *Nanoscale*, 7(11):4598–4810, 2015.

[69] Phaedon Avouris and Marcus Freitag. Graphene photonics, plasmonics, and optoelectronics. *IEEE Journal of selected topics in quantum electronics*, 1(20):6000112, 2014.

[70] FHL Koppens, T Mueller, Ph Avouris, AC Ferrari, MS Vitiello, and M Polini. Photodetectors based on graphene, other two-dimensional materials and hybrid systems. *Nature nanotechnology*, 9(10):780–793, 2014.

[71] Qing Hua Wang, Kourosh Kalantar-Zadeh, Andras Kis, Jonathan N Coleman, and Michael S Strano. Electronics and optoelectronics of two-dimensional transition metal dichalcogenides. *Nature nanotechnology*, 7(11):699–712, 2012.

[72] L. Britnell, R. M. Ribeiro, A. Eckmann, R. Jalil, B. D. Belle, A. Mishchenko, Y.-J. Kim, R. V. Gorbachev, T. Georgiou, S. V. Morozov, A. N. Grigorenko, A. K. Geim, C. Casiraghi, A. H. Castro Neto, and K. S. Novoselov. Strong light-matter interactions in heterostructures of atomically thin films. *Science*, 340(6138):1311–1314, 2013.

[73] Chang-Hua Liu, You-Chia Chang, Theodore B Norris, and Zhaohui Zhong. Graphene photodetectors with ultra-broadband and high responsivity at room temperature. *Nature nanotechnology*, 9(4):273–278, 2014.

[74] U Sassi, R Parret, S Nanot, M Bruna, S Borini, S Milana, D De Fazio, Z Zhuang, E Lidorikis, FHL Koppens, et al. Graphene-based, mid-infrared, room-temperature pyroelectric bolometers with ultrahigh temperature coefficient of resistance. *arXiv preprint arXiv:1608.00569*, 2016.

[75] Tania Roy, Mahmut Tosun, Xi Cao, Hui Fang, Der-Hsien Lien, Peida Zhao, Yu-Ze Chen, Yu-Lun Chueh, Jing Guo, and Ali Javey. Dual-gated mos2/wse2 van der waals tunnel diodes and transistors. *Acs Nano*, 9(2):2071–2079, 2015.

[76] Vadim V Cheianov, Vladimir Fal'ko, and BL Altshuler. The focusing of electron flow and a veselago lens in graphene pn junctions. *Science*, 315(5816):1252–1255, 2007.

[77] XJ Shang, JF He, HL Wang, MF Li, Y Zhu, ZC Niu, and Ying Fu. Effect of built-in electric field in photovoltaic inas quantum dot embedded gaas solar cell. *Applied Physics A*, 103(2):335–341, 2011.

[78] Gerasimos Konstantatos and Edward H Sargent. Nanostructured materials for photon detection. *Nature nanotechnology*, 5(6):391–400, 2010.

[79] Sukosin Thongrattanasiri, Frank HL Koppens, and F Javier García de Abajo. Complete optical absorption in periodically patterned graphene. *Physical review letters*, 108(4):047401, 2012.

[80] Caiyan Ye, Zhihong Zhu, Wei Xu, Xiaodong Yuan, and Shiqiao Qin. Electrically tunable absorber based on nonstructured graphene. *Journal of Optics*, 17(12):125009, 2015.

[81] Ashkan Vakil and Nader Engheta. Transformation optics using graphene. *Science*, 332(6035):1291–1294, 2011.

[82] Matthew Yankowitz, Jiamin Xue, Daniel Cormode, Javier D Sanchez-Yamagishi, K Watanabe, T Taniguchi, Pablo Jarillo-Herrero, Philippe Jacquod, and Brian J LeRoy. Emergence of superlattice dirac points in graphene on hexagonal boron nitride. *Nature Physics*, 8(5):382–386, 2012.

[83] Jun Kang, Jingbo Li, Shu-Shen Li, Jian-Bai Xia, and Lin-Wang Wang. Electronic structural moire pattern effects on mos2/mose2 2d heterostructures. *Nano letters*, 13(11):5485–5490, 2013.

[84] Cheol-Hwan Park, Li Yang, Young-Woo Son, Marvin L Cohen, and Steven G Louie. Anisotropic behaviours of massless dirac fermions in graphene under periodic potentials. *Nature Physics*, 4(3):213–217, 2008.

[85] Cheol-Hwan Park, Young-Woo Son, Li Yang, Marvin L Cohen, and Steven G Louie. Electron beam supercollimation in graphene superlattices. *Nano letters*, 8(9):2920–2924, 2008.

[86] Britton WH Baugher, Hugh OH Churchill, Yafang Yang, and Pablo Jarillo-Herrero. Optoelectronic devices based on electrically tunable pn diodes in a monolayer dichalcogenide. *Nature nanotechnology*, 9(4):262–267, 2014.

[87] Andreas Pospischil, Marco M Furchi, and Thomas Mueller. Solar-energy conversion and light emission in an atomic monolayer pn diode. *Nature nanotechnology*, 9(4):257–261, 2014.

[88] Jason S. Ross, Philip Klement, Aaron M. Jones, Nirmal J. Ghimire, Jiaqiang Yan, D. G. Mandrus, Takashi Taniguchi, Kenji Watanabe, Kenji Kitamura, Wang Yao, David H. Cobden, and Xiaodong Xu. Electrically tunable excitonic light-emitting diodes based on monolayer WSe2 p–n junctions. *Nature Nanotechnology*, 9(4):268–272, 2014.

[89] Kostya S Novoselov, Andre K Geim, Sergei V Morozov, D Jiang, Y_ Zhang, Sergey V Dubonos, Irina V Grigorieva, and Alexandr A Firsov. Electric field effect in atomically thin carbon films. *science*, 306(5696):666–669, 2004.

[90] K Ueno, S Nakamura, H Shimotani, HT Yuan, N Kimura, T Nojima, H Aoki, Y Iwasa, and M Kawasaki. Discovery of superconductivity in ktao3 by electrostatic carrier doping. *Nature nanotechnology*, 6(7):408–412, 2011.

[91] Yasuhide Ohno, Kenzo Maehashi, Yusuke Yamashiro, and Kazuhiko Matsumoto. Electrolyte-gated graphene field-effect transistors for detecting ph and protein adsorption. *Nano Letters*, 9(9):3318–3322, 2009.

[92] EA Henriksen, D Nandi, and JP Eisenstein. Quantum hall effect and semimetallic behavior of dual-gated aba-stacked trilayer graphene. *Physical Review X*, 2(1):011004, 2012.

[93] Lucas H Hess, Moritz V Hauf, Max Seifert, Florian Speck, Thomas Seyller, Martin Stutzmann, Ian D Sharp, and Jose A Garrido. High-transconductance graphene solution-gated field effect transistors. *Applied Physics Letters*, 99(3):033503, 2011.

[94] Guillaume Froehlicher and Stéphane Berciaud. Raman spectroscopy of electrochemically gated graphene transistors: Geometrical capacitance, electron-phonon, electron-electron, and electron-defect scattering. *Physical Review B*, 91(20):205413, 2015.

[95] Sameer Grover, Anupama Joshi, Ashwin Tulapurkar, and Mandar M Deshmukh. Abrupt pn junction using ionic gating at zero-bias in bilayer graphene. *Scientific Reports*, 7, 2017.

[96] B Bilenberg, S Jacobsen, MS Schmidt, LHD Skjolding, P Shi, Peter Bøggild, JO Tegenfeldt, and Anders Kristensen. High resolution 100 kv electron beam lithography in su-8. *Microelectronic Engineering*, 83(4-9):1609–1612, 2006.

[97] Comsol. *COMSOL Multiphysics: Version 5.0*. Comsol, 2015.

[98] Allen J Bard, Larry R Faulkner, Johna Leddy, and Cynthia G Zoski. *Electrochemical methods: fundamentals and applications*, volume 2. Wiley New York, 1980.

[99] Anindya Das, S Pisana, B Chakraborty, S Piscanec, SK Saha, UV Waghmare, KS Novoselov, HR Krishnamurthy, AK Geim, and AC Ferrari. Monitoring dopants by raman scattering in an electrochemically top-gated graphene transistor. *Nature nanotechnology*, 3(4):210–215, 2008.

[100] Richard H Boyd. The dielectric constant of lamellar semicrystalline polymers. *Journal of Polymer Science Part B: Polymer Physics*, 21(4):505–514, 1983.

[101] Chenguang Lu, Qiang Fu, Shaoming Huang, and Jie Liu. Polymer electrolyte-gated carbon nanotube field-effect transistor. *Nano Letters*, 4(4):623–627, 2004.

[102] Wei Chen and Haroon Ahmed. Fabrication of 5–7 nm wide etched lines in silicon using 100 kev electron-beam lithography and polymethylmethacrylate resist. *Applied physics letters*, 62(13):1499–1501, 1993.

[103] R J Sengwa, Kulvinder Kaur, and Rakhee Chaudhary. Dielectric properties of low molecular weight poly (ethylene glycol) s. *Polymer international*, 49(6):599–608, 2000.

[104] Naokazu Koizuim and Tetsuya Hanai. Dielectric properties of lower-membered polyethylene glycols at low frequencies. *The Journal of Physical Chemistry*, 60(11):1496–1500, 1956.

[105] SP Beaumont, PG Bower, T Tamamura, and CDW Wilkinson. Sub-20-nm-wide metal lines by electron-beam exposure of thin poly (methyl methacrylate) films and liftoff. *Applied Physics Letters*, 38(6):436–439, 1981.

[106] Huigao Duan, Donald Winston, Joel KW Yang, Bryan M Cord, Vitor R Manfrinato, and Karl K Berggren. Sub-10-nm half-pitch electron-beam lithography by using poly (methyl methacrylate) as a negative resist. *Journal of Vacuum Science & Technology B*, 28(6):C6C58–C6C62, 2010.

[107] HG Duan, EQ Xie, and L Han. Turning electrospun poly (methyl methacrylate) nanofibers into graphitic nanostructures by in situ electron beam irradiation. *Journal of Applied Physics*, 103(4):046105, 2008.

[108] Huigao Duan, Jianguo Zhao, Yongzhe Zhang, Erqing Xie, and Li Han. Preparing patterned carbonaceous nanostructures directly by overexposure of pmma using electron-beam lithography. *Nanotechnology*, 20(13):135306, 2009.

[109] William H Beyer. *CRC Handbook of chemistry and physics*. CRC press, 1984.

[110] JR Williams, L DiCarlo, and CM Marcus. Quantum hall effect in a gate-controlled pn junction of graphene. *Science*, 317(5838):638–641, 2007.

[111] Allen L. Hsu, Patrick Herring, Nathaniel Gabor, Sungjae Ha, Yong Cheol Shin, Yi Song, Matthew Chin, Madan Dubey, Anantha Chandrakasan, Jing Kong, Pablo Jarillo-Herrero, and Tomas Palacios. Graphene-based thermopile for thermal imaging applications. *Nano letters*, 15(11):7211–7216, 2015.

[112] Patrick K Herring, Allen L Hsu, Nathaniel M Gabor, Yong Cheol Shin, Jing Kong, Tomás Palacios, and Pablo Jarillo-Herrero. Photoresponse of an electrically tunable ambipolar graphene infrared thermocouple. *Nano letters*, 14(2):901–907, 2014.

[113] Steven Johnson. *THe NLopt nonlinear-optimization package*. http://ab-initio.mit.edu/nlopt.

[114] Jian Wang and Sungjoo Lee. Ge-photodetectors for si-based optoelectronic integration. *Sensors*, 11(1):696–718, 2011.

[115] Di Liang, Gunther Roelkens, Roel Baets, and John E Bowers. Hybrid integrated platforms for silicon photonics. *Materials*, 3(3):1782–1802, 2010.

[116] Fengnian Xia, Han Wang, Di Xiao, Madan Dubey, and Ashwin Ramasubramaniam. Two-dimensional material nanophotonics. *Nature Photonics*, 8(12):899, 2014.

[117] Lei Wang, I Meric, PY Huang, Q Gao, Y Gao, H Tran, T Taniguchi, Kenji Watanabe, LM Campos, DA Muller, et al. One-dimensional electrical contact to a two-dimensional material. *Science*, 342(6158):614–617, 2013.

[118] Andreas Pospischil, Markus Humer, Marco M Furchi, Dominic Bachmann, Romain Guider, Thomas Fromherz, and Thomas Mueller. Cmos-compatible graphene photodetector covering all optical communication bands. *Nature Photonics*, 7(11):892–896, 2013.

[119] Xuetao Gan, Ren-Jye Shiue, Yuanda Gao, Inanc Meric, Tony F Heinz, Kenneth Shepard, James Hone, Solomon Assefa, and Dirk Englund. Chip-integrated ultrafast graphene photodetector with high responsivity. *Nature Photonics*, 7(11):883, 2013.

[120] Daniel Schall, Daniel Neumaier, Muhammad Mohsin, Bartos Chmielak, Jens Bolten, Caroline Porschatis, Andreas Prinzen, Christopher Matheisen, Wolfgang Kuebart, Bernhard Junginger, et al. 50 gbit/s photodetectors based on wafer-scale graphene for integrated silicon photonic communication systems. *Acs Photonics*, 1(9):781–784, 2014.

[121] Xuetao Gan, Ren-Jye Shiue, Yuanda Gao, Kin Fai Mak, Xinwen Yao, Luozhou Li, Attila Szep, Dennis Walker Jr, James Hone, Tony F Heinz, et al. High-contrast electrooptic modulation of a photonic crystal nanocavity by electrical gating of graphene. *Nano letters*, 13(2):691–696, 2013.

[122] Arka Majumdar, Jonghwan Kim, Jelena Vuckovic, and Feng Wang. Electrical control of silicon photonic crystal cavity by graphene. *Nano letters*, 13(2):515–518, 2013.

[123] Mark I Stockman. Nanofocusing of optical energy in tapered plasmonic waveguides. *Physical review letters*, 93(13):137404, 2004.

[124] Sergey I Bozhevolnyi, Valentyn S Volkov, Eloise Devaux, and Thomas W Ebbesen. Channel plasmon-polariton guiding by subwavelength metal grooves. *Physical review letters*, 95(4):046802, 2005.

[125] JA Dionne, LA Sweatlock, HA Atwater, and A Polman. Plasmon slot waveguides: Towards chip-scale propagation with subwavelength-scale localization. *Physical Review B*, 73(3):035407, 2006.

[126] Cheng Peng and Dirk Englund. Tunable graphene metamaterials for beam steering and tunable flat lenses, August 8 2019. US Patent App. 16/268,566.